

Construction of Large Area Micromegas Detectors
Konstruktion großflächiger Micromegas Detektoren



Masterarbeit der Fakultät für Physik
der
Ludwig-Maximilians-Universität München

eingereicht von

Elias Pree

München, 30. Oktober 2014

Gutachter: Prof.Dr. Otmar Biebel

Zusammenfassung

Die Designluminosität des Large Hadron Collider (LHC) wird im Jahr 2022 auf $5 \cdot 10 \times 10^{34} \text{ cm}^2 \text{ s}^{-1}$ erhöht. Dafür muss das ATLAS Myonenspektrometer aufgewertet werden. Die gegenwärtigen Detektoren des sogenannten Small Wheels, wovon es zwei Stück im ATLAS Detektor gibt und die eine scheibenartige Struktur besitzen, sind Cathode Strip Chambers (CSC) und Monitored Drift Tubes (MDT). Diese werden nicht in der Lage sein die mit der Luminositätssteigerung einhergehenden hohen Trefferraten von mehr als 15 kHz cm^{-2} zu verarbeiten. Die maximal erlaubte Trefferrate in einer MDT-Röhre ist 300 kHz . Da diese jeweils eine Fläche von 150 cm^2 haben, ist die maximale Trefferrate pro Fläche niedriger als 2 kHz cm^{-2} . Deshalb werden diese Detektor Systeme mit sogenannten small strip Thin Gap Chambers (sTGC) und Micromegas (MM) Detektoren ersetzt. Diese werden eine Fläche von einigen Quadratmetern haben.

Das neue Small Wheel (NSW) ist aufgeteilt in acht große und acht kleine Sektoren. Ein großer Sektor ist untergliedert in das LM1 und das LM2 Modul, ein kleiner in das SM1 und SM2 Modul. Jedes Modul besteht aus zwei Quadruplets von sTGC Detektoren, die zwei MM Detektorquadruplets umschließen, welche Rücken an Rücken miteinander verbunden sind. Die Micromegas Detektoren werden verwendet, um die Spur von Myonen, die vom Kollisionspunkt des ATLAS Detektors kommen, zu rekonstruieren. Die Konstruktion der 2 m^2 großen MM Quadruplets des SM2 Moduls ist das Hauptthema dieser Arbeit. Der Konstruktionsprozess wird erklärt anhand der Konstruktion des mechanischen Prototypen M1.

Ein notwendiges Werkzeug, um ebene Sandwich Platten zu bauen, welche im Micromegas Quadruplet verwendet werden, ist das sogenannte Stiffback. Dieses ist eine sehr steife und ebene Sandwich Struktur in Leichtbauweise. Die Entwicklung von einem anfänglichen Prototyp bis zum gegenwärtigen Design wird gezeigt. Das derzeit verwendete Design für das Stiffback hat eine Fläche von $2 \times 1.5 \text{ m}^2$ und besteht aus zwei 1 mm dicken Aluminium Platten, die einen 8 cm dicken Aluminium Kern aus hexagonaler Wabenstruktur umschließen.

Die Hauptschwierigkeit in der Konstruktion von 2 m^2 großen Sandwich Platten, die für das Micromegas Quadruplet benutzt werden, liegt darin, dass die Parallelität der Oberflächen des selben Sandwiches unter $80 \mu\text{m}$ liegt. Diese gute Planarität wird benötigt, damit man eine Ortsauflösung von unter $100 \mu\text{m}$ in jeder Detektor Ebene erreicht. Um die Ebenheit der Oberflächen zu untersuchen, werden verschiedene Messtechniken erklärt und verglichen. Von den drei untersuchten Methoden, welche unter anderem den Gebrauch eines Haarlineals und eines Interferometers beinhalten, hat sich der Gebrauch einer computergesteuerten Messmaschine mit Tastkopf als am praktikabelsten erwiesen.

Um Verformungen der äußersten Sandwich Platten in jedem Quadruplett zu reduzieren, werden zusätzliche Zwischenverbindungen gebraucht. Diese Verformungen

entstehen wegen des Überdrucks im Gasetektor. ANSYS Simulationen werden durchgeführt, um die Anzahl dieser Verbindungen zu reduzieren. Ursprünglich wurden neun Verbindungen für das SM2 Modul vorgeschlagen, doch konnte die Anzahl auf sechs verkleinert werden.

Eine Theorie, um die Steifheit und Durchbiegung von Sandwich Strukturen abzuschätzen ist die Sandwich Theorie. Die Durchbiegung von Sandwich Balken wird im Detail erklärt. Die Theorie führt die Biegesteifigkeit D des Sandwichbalkens ein, welche man benutzen kann, um die Steifheit von Sandwich Strukturen zu charakterisieren.

Jeder Micromegas Detektor braucht ein gespanntes Stahlgitter. Der Spann-Prozess wird erklärt und es werden zwei verschiedene Spann-Systeme miteinander verglichen. Mehrere $24 \times 24 \text{ cm}^2$ große Stahlgitter werden gespannt. Die Sefar 3A Spannkluppen haben sich den Kluppen der Yuancheng Printing Equipment Firma gegenüber als überlegen erwiesen.

Ein Vergleichspunkt ist die Homogenität der Gitterspannung, welche mit Spannungsmessgeräten gemessen wird. Zusätzlich werden zwei verschiedene Spannungsmessgeräte verglichen. Der Sefar Tensocheck 100 und der Newman ST1E Spannungsmesser. Das Gerät von Sefar hat sich in den Tests hier durchgesetzt, da es nicht so leicht Knicke im feinen Stahlgitter erzeugt.

Zuletzt werden noch Rechnungen und Simulationen mit ANSYS präsentiert, welche die Verformung des Gitters unter dem Einfluss des elektrischen Feldes im Detektor zeigen.

Abstract

The ultimate design luminosity of the Large Hadron Collider (LHC) will be increased to $5 \cdot 10 \times 10^{34} \text{ cm}^2 \text{ s}^{-1}$ in 2022. The ATLAS muon spectrometer therefore needs to be upgraded. The muon spectrometer has two Small Wheels, which are disk-like structures. The current detectors of the Small Wheel consisting of Cathode Strip Chambers (CSC) and Monitored Drift Tubes (MDT) will not be able to handle the new hit rates higher than 15 kHz cm^{-2} . The maximal allowed hit rate of a single MDT is 300 kHz. A single MDT has an area of 150 cm^2 , which leads to a maximal allowed hit rate per area below 2 kHz. These detector systems therefore get replaced with small strip Thin Gap Chambers (sTGC) and Micromegas detectors (MM), which will have an area of several square meter.

The New Small Wheel is segmented in eight large and eight small sectors. The large sector is divided in the LM1 and LM2 module and the small sector in the SM1 and SM2 module. Each module consists of two quadruplets of sTGC detectors sandwiching two back to back mounted MM detector quadruplets. The Micromegas detectors are used for the tracking of the muons coming from the interaction point of the ATLAS detector. The construction of the 2 m^2 sized Micromegas quadruplets of the SM2 module is the main topic of this thesis. The construction process is explained based on the construction of the mechanical prototype M1.

A necessary tool for the construction of planar sandwich panels, used in the Micromegas quadruplet, is the "stiffback" which is a very stiff, light weight and planar sandwich construction. The development from an initial prototype to the present design of the stiffback is shown. The present stiffback design, with an area of $2 \times 1.5 \text{ m}^2$, consists of two 1 mm thick aluminium plates sandwiching a 8 cm thick aluminium honeycomb core.

The main difficulty in the construction of the 2 m^2 sized sandwich panels, used for the Micromegas quadruplet, is to achieve a parallelism of the two surfaces of the same sandwiches of better than $80 \mu\text{m}$. The reason for the planarity is to assure a spatial resolution below $100 \mu\text{m}$ in each detector plane. To check the planarity of the surfaces different measurement techniques are explained and compared. Out of the three methods, which include amongst others the use of a straight edge or an interferometer, the use of a computerized measurement machine (CMM) with a probe head has proven to be the most practical.

To reduce the deformation, due to gas overpressure in the gas detector, of the outer sandwich panels in each quadruplet, interconnections are needed. ANSYS simulations are performed to reduce the number of interconnections. The amount of interconnections needed is now six in comparison to the initially proposed nine for the SM2 module.

A theory to estimate the stiffness and deformation of sandwich structures is the sandwich theory. The deformation of sandwich beams is explained in detail. The theory introduces the bending stiffness D of a sandwich beam, which can be used to characterize the stiffness of sandwich constructions.

Each Micromegas detector needs a stretched steel mesh. The stretching process is explained and two different stretching systems are compared. Several $24 \times 24 \text{ cm}^2$ stretched steel meshes are therefore produced. The Sefar 3A stretching clamps are superior in comparison to the stretching clamps from the Yuancheng Printing Equipment company.

One aspect in the comparison is the homogeneity of the mesh tension, which is tested with tension meters. Additionally, two different tension meters are compared. The Sefar Tensocheck 100 and the Newman ST1E tension meter. The Sefar device is more favourable, since it does not induce kinks in the mesh as easy as the other device.

At last calculations and simulations with ANSYS, which show the deformation of the mesh under the influence of the electric field, are presented.

Contents

1	Introduction	1
2	Introduction to ANSYS	5
3	The Micromegas Working Principle	7
3.1	Interaction of Charged Particles with Matter	7
3.2	Gas Amplification	8
3.3	The Micromegas Principle	9
4	Sandwich-Beam Theory	11
4.1	Derivation of Sandwich Beam Differential Equations	12
4.2	Derivation of Beam Bending Formula	18
4.3	Beam Bending Example	20
5	Construction of Sandwich Panels	23
5.1	Construction Method for First Prototype	23
5.2	Production Process of Readout Panels	27
6	Surface Measurements of Sandwich Panels	29
6.1	Determination of the E-Modulus of FR4	29
6.2	Planarity Measurement using a Straight Edge	30
6.3	Deflection Measurement using an Interferometer	32
6.4	Deflection Measurement with a CMM	38
7	Development of the Stiffback	45
7.1	First Stiffback Version	45
7.2	Double Honeycomb Concept	50
7.3	Final Design	54
7.4	Small Scale Prototype for New Design	55
8	Interconnections	63
9	Mesh	67
9.1	Mesh Stretching Process	68
9.2	Comparison of Sefar Tensocheck 100 and Newman Tension Meter . .	73
9.3	Mesh Deflection between Pillars due to the Electric Field	78
9.4	Sandwich Deformation because of Mesh Tension	81

10 Summary	85
A Material constants	87
Bibliography	89

1 Introduction

The Large Hadron Collider (LHC) at CERN in Switzerland is an almost 27 km long particle accelerator. In the first run between 2010 and 2012 it initially accelerated protons up to a center of mass energy of 7-8 TeV. The protons get accelerated not only in one direction, but in the direction opposite to the initial one of the ring-like accelerator as well and collide in four different places. At each collision point is a complex detector structure. One is the Atlas detector ([ATLAS Collaboration, 2008]), which is an acronym for "A Toroidal LHC ApparatuS". The proton-proton collisions produce many new particles, whose decay products can be detected. One of the main goals of the Atlas detector is the search for the Higgs-boson and its properties. Another application of the detector is the search for supersymmetric particles.

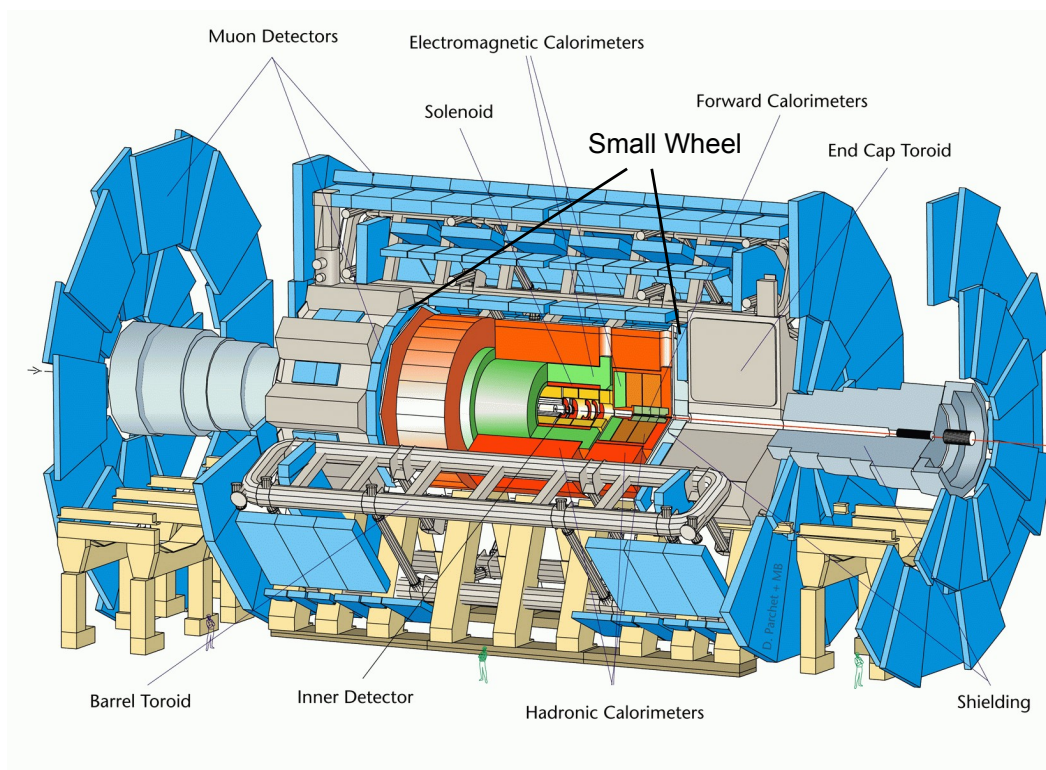


Figure 1.1: Cross section of the ATLAS detector taken from [ATLAS Collaboration, 2013]

To prove the existence of such new particles the amount of collision data has to be maximized. The next major increase of the integrated luminosity is planned in 2018, whereas the center of mass energy shall be increased from the current 8 TeV to the nominal energy of 13-14 TeV within 2015. In 2022 the luminosity will be increased to

the ultimate design luminosity of about $5 \times 10^{34} \text{ cm}^{-2} \text{ s}^{-1}$. Because of the increase of the luminosity the background hit rate will increase accordingly.

Some of the low background decay channels of the collisions include muons. They are detected and momentum analyzed in the muon spectrometer of the ATLAS detector. It consists of a barrel part and end cap regions, which are disk-like structures. The innermost disk-like end cap region is the small wheel. Since 90% of the level 1 trigger for muons is coming from the endcap regions with an η larger than one and the small wheel being the closest to the collision point, the background hit rate is the largest. After the upgrade in 2018 the hit rate will be higher than 15 kHz cm^{-2} . The current detector system in the small wheel are Monitored Drift Tubes (MDT) and Cathode Strip Chambers (CSC). They can not handle such rates. To ensure the high rate capability and muon tracking resolution below $100 \mu\text{m}$ new detectors have to be implemented in the New Small Wheel. So called small strip Thin Gap Chamber (sTGC) and Micromegas (MM) detectors will be used.

The section layout of the present Small Wheel can be seen in figure 1.2.

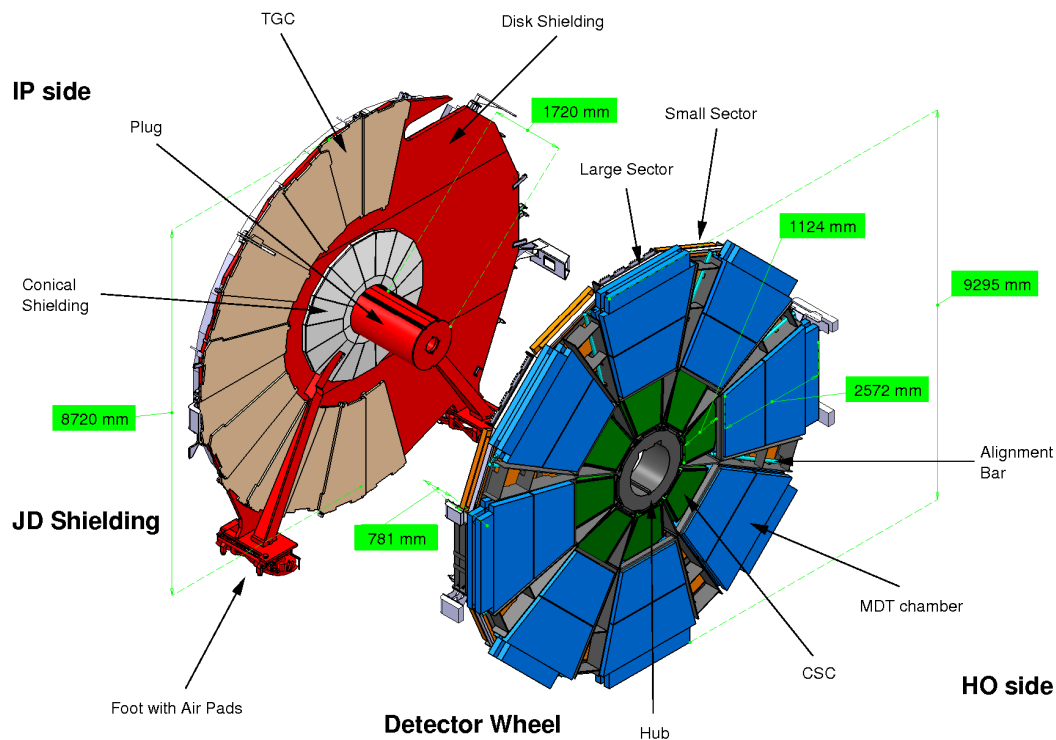


Figure 1.2: Layout of the present Small Wheel taken from [ATLAS Collaboration, 2013]

It consists of eight large and eight small sections. In the new upgraded Small Wheel the section layout is the same, but each sector consists of two quadruplets of sTGC detectors sandwiching two Micromegas detector quadruplets. Each quadruplet consists of four detectors. This layout is shown in figure 1.3.

The small and the large sector are additionally segmented in two pieces. The segmentation and the dimensions of each sector are shown in figure 1.4.

The sTGC detectors are used for triggering and the Micromegas detectors are used for precision coordinate determination. But both detector types could execute the

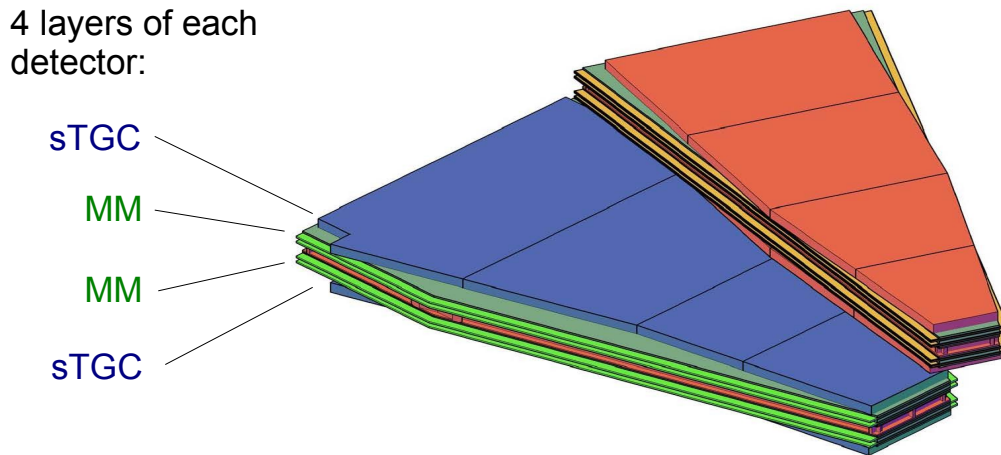


Figure 1.3: Four layers of sTGC detectors sandwiching two back to back mounted Micromegas (MM) quadruplets in the small and large sector. The Micromegas are indicated by the green and yellow colours and consist of 2×4 active layers. Figure is taken from [ATLAS Collaboration, 2013]

task of the other type as well. This means the greatest possible redundancy. The construction of these Micromegas quadruplets, especially the SM2 modul, which is built in a collaboration by the universities of Freiburg, Mainz, Würzburg and Munich (LMU), is the main topic of this thesis. The difficulty in the construction is given by the fact, that the several square meter large sandwich panels of the quadruplets may only have a parallelism of the surfaces of the same sandwiches of better than $80 \mu\text{m}$. Additionally to the general production process, various issues coming along with the construction will be addressed and solved. An important tool for the construction is a "stiffback", whose development and construction will be shown as well.

One issue for example is the blow up of the outer sandwich panels in each quadruplet induced by gas over pressure in the Micromegas detectors. This is solved by the use of interconnections. Another issue discussed is the stretching of the mesh, used for the detectors, and the deformation of it due to the electric field.

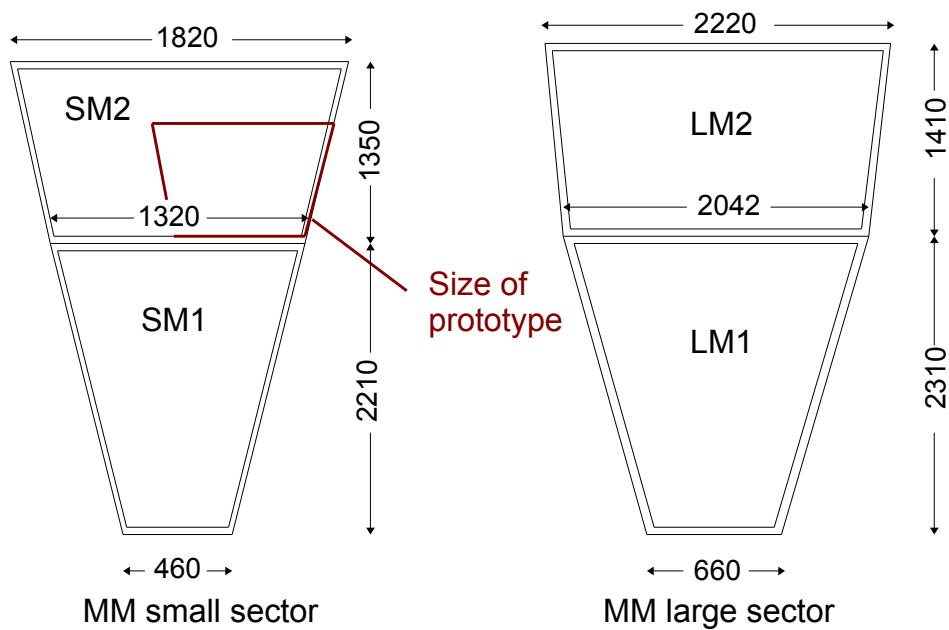


Figure 1.4: Dimensions of the segmented Micromegas sectors of the New Small Wheel in [mm]; additionally the size of the M1 mechanical prototype quadruplet is given for comparison

2 Introduction to ANSYS

The tool to simulate the deformations of the sandwich structures, used for the construction of the quadruplet, is the program package ANSYS from ANSYS, Inc. It is an engineering simulation software used to predict how product designs will behave. It makes use of the finite element method, which is a numerical method to find solutions for boundary value problems for partial differential equations. A sandwich structure is a planar plate consisting of multiple layers of different materials. This structural composition has some advantages, which will be mentioned later in this work.

Throughout the thesis several ANSYS simulations will be presented to check the deformations of different structures. To explain how such a simulation is performed, the term "element type" has to be explained at first. The explanations follow the ANSYS Element Reference [ANSYS, Inc., 2013].

First of all an element type is identified by a name, such as SHELL281, which consists of a group label (SHELL) and an identifying number (281). Depending on the model there are 2-D and 3-D elements. 2-D models are only defined in the x-y plane and are easier to set up and run faster than equivalent 3-D models. In general there are four element shapes possible: points, lines, areas and volumes. A point element is typically defined by one node. A line element is represented by a line connecting two or three nodes. An area element has a triangular or quadrilateral shape and may be a 2-D solid element or a shell. A volume element has a tetrahedral or brick shape and is usually a 3-D solid element. There are also degrees of freedom of the element determining the discipline for which the element is applicable. Typical applications are in structural, thermal, fluid, electric, magnetic, or coupled-field applications.

To simulate deformations of flat sandwich panels, usually the element SHELL281 is used in the thesis. It is an area element, which is not only working very well for this task but also requires little computation time. In an exemplary sandwich panel bending simulation, after the element type of the problem is chosen, different materials with its corresponding mechanical properties have to be introduced. Afterwards one can define several section-layers for this element type. Because of the multiple thin layers of a sandwich, it is more resource efficient to use such a SHELL element type with several layers, instead of a 3-D solid element type. The next part in the simulation would be the modelling of the geometry. Because of the use of a 2-D element to simulate a 3-D sandwich panel it is only necessary to build an area, which is made up from lines and keypoints. When meshing the area the nodes and elements are created. A node is a point that is connected to another node by an element. The elements and nodes are interconnected by a mesh. After the mesh is defined, the boundary conditions and the loading scenario have to be implemented. The boundary conditions are applied by the displacement constraining of nodes or

elements in different translational and rotational degrees of freedom. If the plate should be simply supported, only the translational degrees of freedom of the nodes of the support have to be fixated. Simply supported means, that the supports of the object, on which bending experiments are performed, are able to rotate. This is in comparison to a fixed support, which means the support can not rotate. This are two typical boundary conditions for bending experiments. To simulate the loading, a force or pressure can be applied to the nodes or area. After all of this is done, the programm can solve the problem and the numerous informations, like deformations or stresses, of the solution can be read out for example in the form of lists or plots. All ANSYS plots throughout the thesis will have a column in the top left corner, which gives information about what solution is displayed. The exact meaning of all numbers will not be explained, because they are of no importance for the thesis here.

3 The Micromegas Working Principle

The expression Micromegas is an abbreviation for "MICRO-MEsh GASEous structure". They are gas filled planar proportional chambers that have been proposed by [Giomataris et al., 1996]. Before the working principle of such a detector is described more in detail, the most important underlying physical phenomena are presented. They are taken from [Leo, 1994].

3.1 Interaction of Charged Particles with Matter

When charged particles traverse matter they lose energy and they can be deflected. This is mostly due to inelastic collisions with the atomic electrons of the material. There are other processes like the emission of Cherenkov radiation, nuclear reactions, bremsstrahlung or nuclear interactions, but they are compared to the atomic collision process much more rare or energetically hindered.

For charged particles like muons, pions, protons, α -particles and other light nuclei the main energy loss is coming from the inelastic collisions. These collisions with a cross section $\sigma = 10^{-17} - 10^{-16} \text{cm}^2$ transfer energy to the atom causing ionization or excitation. If the energy transfer of one of the many collisions is too small, the atom can only be excited and not ionized. The inelastic collisions occur with a certain quantum mechanical probability. Despite the energy loss in one collision being small, with many of it taking place in a macroscopic pathlength, the fluctuation in the total energy loss becomes small. It is therefore legitimate to work with the average energy loss per unit path length, which is called stopping power or simply dE/dx . The correct quantum-mechanical calculation was first performed by Bethe, Bloch and other authors. The obtained Bethe-Bloch formula is given in equation 3.1. The density effect correction δ and the shell correction C are added as well.

$$-\frac{dE}{dx} = 2\pi N_a r_e^2 m_e c^2 \rho \frac{Z}{A} \frac{z^2}{\beta^2} \left[\ln \left(\frac{2m_e \gamma^2 v^2 W_{max}}{I^2} \right) - 2\beta^2 - \delta - 2\frac{C}{Z} \right] \quad (3.1)$$

The term $2\pi N_a r_e^2 m_e c^2$ can be calculated to $0.1535 \text{ MeV cm}^2 \text{ g}^{-1}$. Including the density ρ the units of the Bethe-Bloch formula are MeV cm^{-1} .

The maximum energy transfer in a single collision is given for an incident particle of mass M by

$$W_{max} = \frac{2 m_e c^2 \beta^2 \gamma^2}{1 + 2 \frac{m_e}{M} \sqrt{1 + \beta^2 \gamma^2} + \frac{m_e^2}{M^2}} \quad (3.2)$$

r_e :	classical electron radius = $2.817 \cdot 10^{-15} m$	ρ :	density of absorbing material
m_e :	electron mass	z :	charge of incident particle [e]
N_a :	Avogadro's number = $6.022 \cdot 10^{23} mol^{-1}$	$\beta =$	$\frac{v}{c}$ of incident particle
I :	mean excitation potential	$\gamma =$	$\frac{1}{\sqrt{1-\beta^2}}$
Z :	atomic number of absorbing material	δ :	density correction
A :	atomic weight of absorbing material	C :	shell correction

Table 3.1: Parameters of Bethe-Bloch-formula

The stopping power of a positively charged muon in copper depending on his momentum is shown in figure 3.1. For very small and very large muon energies the Bethe-Bloch formula does not work anymore. In this regions other theories are used to describe the behaviour. Another interesting point to mention is the minimum at $\beta\gamma \approx 3.5$. Near this minimum is the energy region of the minimum ionizing cosmic muons. They have an energy of about 2 GeV and have a stopping power of about 2 MeV cm²/g. In comparison the muons, which want to be detected in the Micromegas detectors of the New Small Wheel have an energy above 20 GeV. This is the muon energy threshold for the level 1 trigger of the New Small Wheel. One cosmic muon for example deposits in a 5 mm large drift space, which is filled with argon with a density of 1.784 g cm⁻³, about 1784 eV. With a mean energy to produce an electron pair of 26 eV in argon [Pree, 2012], a muon produces about 68 electrons along its track in the drift region in the detector.

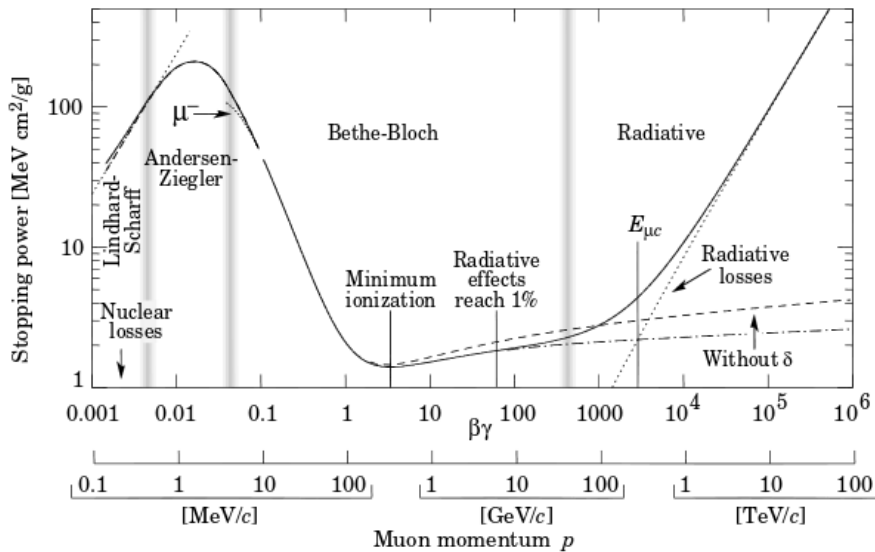


Figure 3.1: Energy loss depending on the muon momentum taken from [Groom et al., 2001]

3.2 Gas Amplification

Another important process, which takes place in the Micromegas detector is the gas amplification. Charged particles lose energy in the gas volume of the detector

according to Bethe-Bloch and create electron ion pairs. In an electric field such free electrons get accelerated. When the electric field is high enough these accelerated electrons gain enough energy to be able to create new electron-ion pairs. This means in a high electric field one electron produces another electron after an ionization pathlength λ . After several path lengths an avalanche like multiplication of the charges takes place. The probability for an electron to produce another one in a path length λ is 1. With the first townsend coefficient α

$$\alpha = \frac{1}{\lambda}$$

and the initial number of electrons n , the number of electrons created along a path length dx is given by:

$$dn = n\alpha dx$$

The integration of dn results in the total number of electrons in the path x , where gas amplification takes place and where n_0 is the number of initially present electrons:

$$n = n_0 \cdot \exp(\alpha x)$$

To obtain the gas amplification (or gas gain) factor G , n has to be divided by n_0 . The result is :

$$G = \exp(\alpha x)$$

This gas gain factor is typically in the orders of $\sim 10^3$ to 10^4 for Micromegas detectors.

3.3 The Micromegas Principle

Micromegas detectors consist basically of three parallel and planar structures. The drift cathode, a stretched steel mesh and the readout strips of the anode. These are shown in figure 3.2. The detector is filled with a gas mixture of Ar:CO₂ with volumetric ratio 93:7. The gas CO₂ is used as a quenching gas to capture photons and prevent uncontrolled gas multiplication.

On the cathode a typical voltage of -350 Volt is applied. With the mesh being on 0 Volt it results in an electric field, which accelerates electrons towards the mesh. This field is 0.7 kV/cm at a distance of 5 mm between both layers. Because of the drift of the electrons in this region the space between the cathode and the mesh is called the drift region.

The volage applied to the anode strips is in the order of + 530 Volt. Because of the small distance of 128 μ m between the mesh and the anode, the electric field in this

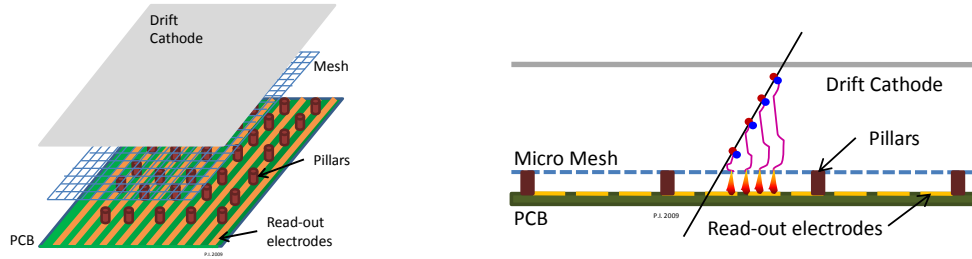


Figure 3.2: The planar layers of a Micromegas detector; drift cathode, micro-mesh and readout pcb with anode strips; taken from [ATLAS Collaboration, 2013]

region is about 40 kV/cm. Such high electric fields lead to gas amplification, which give the amplification region its name. The distance between the mesh and the anode is defined by many small cylindrical pillars with a diameter of 300 μm and height 128 μm . They are arranged with a distance of a few millimeters to each other, 7 mm in the New Small Wheel detector. The electrons created in the drift region arrive at the amplification region within 100 ns. At the given fields the gas amplification is $10^3 - 10^4$. This amount of charge goes to the anode strips and gets registered by the readout electronics. Due to the strip structure of the anode position information and tracking of the ionizing particle can be obtained. The readout strips of the anode are made out of copper. The Micromegas detectors for the New Small Wheel will have a pitch of about 450 μm , which is the distance from the middle of one strip to the middle of its neighbouring strip. The anode strips and readout electronics are placed on standard printed circuit boards (PCB). They use typically FR4 as isolating material, which is a composite material of woven fiberglass bound with an epoxy resin that is flame resistant. The FR4 sheets will be of importance later at the construction of the Micromegas detectors.

This chapter has shown the working principle of the Micromegas detector and the important physical fundamentals. Before the construction method of the Micromegas quadruplets is explained, the sandwich beam theory will be introduced. Because of the necessity of the planarity of the structures in the Micromegas detector, it is a useful tool to estimate the deformation and stiffness of sandwich panels, which are a main component in the detector.

4 Sandwich-Beam Theory

The bending of the sandwich structures, introduced in chapter 5, and the bending of auxiliary construction tools needs to be as small as possible. A way to describe the deformation is the sandwich-beam theory. With its help the bending stiffness D will be introduced, which is a measure for the bending stiffness of the sandwich. It can be used to compare the stiffness of sandwich structures. The parameter D is also used in the formula, which will be derived and which can describe the deformation of sandwich beams under loading with a force. The derivation follows in principle the work of [Huber, 2011/2012], but is influenced by [Hex, 2000] and [Hirschfeld, 2006]. Before the formula is derived, a few terms have to be introduced. The definitions here are taken from [Meschede, 2010].

A force F , which pulls on a wire with cross section A , is prolonging the wire by the length Δl . It is proportional to F , wire length l and $1/A$:

$$\Delta l = \frac{1}{E} \frac{lF}{A}$$

This can be rewritten and generalized to Hooke's Law:

$$\sigma = E \epsilon$$

E is the modulus of elasticity or Young's modulus. The relative expansion $\epsilon = \Delta l/l$ is proportional to the stress $\sigma = F/A$. Since ϵ is dimensionless, the material constant E has the units N/m^2 . The E -modulus is used as a measure of the stiffness of elastic materials.

If for example a force F is applied tangentially to an area A of a quader, the shear stress $\tau = F/A$ arises. It tilts all edges, which are perpendicular to the area A , by the angle α :

$$\tau = G\alpha$$

G is called the shear modulus.

4.1 Derivation of Sandwich Beam Differential Equations

The ultimate goal is the analytical calculation of the deformation of sandwich structures. This can be described by differential equations considering the requirements for the sandwich-beam theory.

Requirements

- The material of the facing sheets and the core is linear elastic. Additionally the core has to be homogenous.
- The facing sheets are plane, parallel and thin in comparison to the beam length. Normal stress is constantly distributed across the facing sheet.
- The E-modulus of the core is very small in comparison to the facing sheets. That has to be the case to be able to neglect the normal stress in the core in comparison to the normal stress in the facing sheets.
- Support and loading are arranged in such a way, that it can be calculated as an one dimensional beam
- The deformations are sufficiently small that a linear dependence between distortion and deformation values can be assumed.

The first task in the derivation of the differential equations for sandwich beams is to take a look at the angular relations of a deformed sandwich element. Figure 4.1 shows all angles and labels of an infinitesimal small deformed beam element. The thickness of the facing sheets of the sandwich is given by the parameters t_f and t_b . The thickness of the core is given by h and it does not change in the bending process. The deflection of the centroid axis of the sandwich beam element is called w .

The total shear angle of the core is:

$$\gamma_K = \gamma_1 + \gamma_{2K}$$

The partial shear angle of the core is:

$$\gamma_1 = \frac{dw}{dx} = w'$$

Throughout the whole chapter ' is representing the differentiation with respect to x . Instead of using γ_{2K} and the total shear angle γ_K of the core, the shear angles γ_2 and γ which refer to the neutral axis of the facing sheets, are used.

$$\gamma = \gamma_1 + \gamma_2 \tag{4.1}$$

The connection between the shear angle types, where $a=a_t+a_b$ is given for small angles by:

$$\Delta U = a\gamma = h\gamma_K \quad (4.2)$$

With equation 4.1 this leads to:

$$\gamma_2 = \frac{h}{a}\gamma_K - w'$$

This are all angular relations which are of importance. In the following the expansion of the facing sheets has to be described.

For small deformations the following statement, where ϵ_b and ϵ_t describe the relative elongation in x-direction of the whole bottom and top facing sheet, is true:

$$\epsilon_b = \frac{du_B}{dx}$$

$$\epsilon_t = \frac{du_T}{dx}$$

The bottom layer gets elongated and the top layer gets compressed. If we assume thin facing sheets, the displacements along the x-axis of u_b and u_t for the top and bottom layer differ only so little from each other in each layer, that they can be replaced by the displacement values of the facing sheet centroids.

$$u_b \approx u_B = \bar{u} + a_b\gamma_2$$

$$u_t \approx u_T = \bar{u} - a_t\gamma_2$$

If this is inserted in the definition of the expansion:

$$\epsilon_b \approx \epsilon_B = \bar{u}' + a_b\gamma_2' \quad (4.3)$$

$$\epsilon_t \approx \epsilon_T = \bar{u}' - a_t\gamma_2' \quad (4.4)$$

For the core of the sandwich the following statement is valid:

$$\tau = G\gamma_K$$

τ denotes the shear stress, G is the shear modulus and γ_K is the shear strain. With equation 4.2 γ_K can be replaced by γ :

$$\tau = \frac{a}{h}G\gamma \quad (4.5)$$

To characterize the expansion of the facing sheets, Hooke's law is viable. If different materials are used the relations are:

$$\sigma_b = E_b \epsilon_b \quad (4.6)$$

$$\sigma_t = E_t \epsilon_t \quad (4.7)$$

The concept of stress resultants will be introduced in the following. They consist of a bending moment M , shear force Q and a normal force N . The direction of these stress resultants can be defined in two different ways. On the one hand they can be independent of the deformation of the sandwich elements. Then they are parallel to the x and z axis and the stress resultants N_x and Q_z are used. But on the other hand the deformed sandwich element can be used for definition. Then the stress resultants are parallel to the borders of the deformed and displaced sandwich elements. Then they are called N and Q . The stress resultants for N and Q are indicated in figure 4.1.

To calculate these stress resultants, the stresses σ and τ have to be integrated over their corresponding cross section area.

$$N = \int_{(A)} \sigma dA = b(t_b \sigma_b + t_t \sigma_t) \quad (4.8)$$

$$M = \int_{(A)} \sigma z dA = b(t_b a_b \sigma_b + t_t a_t \sigma_t) \quad (4.9)$$

$$Q = \int_{(A)} \tau dA = ba\tau \quad (4.10)$$

When inserting 4.3 and 4.4 in 4.6 and 4.7 the following is obtained:

$$\sigma_b = E_b (\bar{u}' + a_b \gamma_2') \quad (4.11)$$

$$\sigma_t = E_t (\bar{u}' - a_t \gamma_2') \quad (4.12)$$

Before inserting the required parameters in the stress resultants the expansion stiffness A of the facing sheets has to be introduced:

$$A_b = E_b b t_b$$

$$A_t = E_t b t_t$$

$$A = A_b + A_t$$

Furthermore the shear stiffness of the core is needed:

$$S = G \frac{ba^2}{h} \quad (4.13)$$

The bending stiffness D [Nm^2] of the total sandwich, which is an important parameter for the characterization of a sandwich, is:

$$D = A_b a_b^2 + A_t a_t^2 \quad (4.14)$$

If both facing sheets have the same thickness and material, equation 4.14 can be rewritten to:

$$D = \frac{Ebt a^2}{2} \quad (4.15)$$

In this formula a equals $a_t + a_b$, which is the distance between the centres of the two facing sheets, and b is the width of the sandwich beam. In a further step equations 4.11 and 4.12 are inserted in the formulas for N and M . After using 4.13 and 4.14 and further simplification, the stress resultants can be written as:

$$N = A\bar{u}' \quad (4.16)$$

$$M = D\gamma_2' = D(\gamma' - w'') \quad (4.17)$$

$$Q = S\gamma \quad (4.18)$$

Equation 4.17 and 4.18 correspond to bending and shear deformation of the sandwich beam. Equation 4.16 corresponds to a pure compression or expansion of the beam. With the help of the equilibrium conditions

$$\sum M_x = 0$$

$$\sum F_z = 0$$

at the deformed beam element the following relations can be obtained:

$$\frac{dM}{dx} - Q = 0 \quad (4.19)$$

$$\frac{dQ}{dx} + q + Nw'' = 0 \quad (4.20)$$

It has to be mentioned that the term Nw'' comes from the deflection of the normal force N by an angle $d\gamma_1$. Because of that a normal force $Nd\gamma_1$ arises, which has to be added to the shear load qdx .

To finally get the differential equations describing the deformation of sandwich beams the method of partial deformations has to be introduced. In this method the total deformation w is split up in two parts:

$$w = w_M + w_Q \quad (4.21)$$

w_M describes the deformation of the sandwichbeam depending on the bending stiffness. w_Q accounts for the part of the deformation arising from the shear deformability.

If these new parameters are put in relation to already introduced angles it looks like the following:

$$w'_M = -\gamma_2 \quad (4.22)$$

$$w'_Q = \gamma \quad (4.23)$$

When inserting 4.22 and 4.23 in 4.17 and 4.18, the following relation is obtained:

$$M = -Dw''_M \quad (4.24)$$

$$Q = Sw''_Q \quad (4.25)$$

To get the wanted differential equations, equation 4.24 and 4.25 have to be inserted into 4.19 and 4.20. The result of this action is:

$$Dw'''_M + Sw'_Q = 0 \quad (4.26)$$

$$(S + N)w''_Q + Nw''_M = -q \quad (4.27)$$

If N is constant, decoupling of the two differential equations results in:

$$\left(1 + \frac{N}{S}\right)w'''_M - \frac{N}{D}w''_M = \frac{q}{D} \quad (4.28)$$

$$\left(1 + \frac{N}{S}\right)w''_Q - \frac{N}{D}w_Q = -\frac{q'}{D} \quad (4.29)$$

If $N = 0$, equation 4.28 and 4.29 result in:

$$w'''_M = \frac{q}{D} \Rightarrow w''_M = -\frac{M}{D} \quad (4.30)$$

$$w''_Q = -\frac{q'}{S} \Rightarrow w'_Q = \frac{Q}{S} \quad (4.31)$$

To solve these differential equations boundary conditions are necessary. The conditions at both ends of the beam for the three different support types are listed in table 4.1. Simple support means, that the end of the sandwich beam is not fixated and only rests on top of any support. This means, that the ends of the beam are able to rotate, when the beam is deformed under loading. When the end is fixed, this rotation is forbidden.

simply supported	$w_M + w_Q = 0$	$w''_M = 0$
fixed end	$w_M + w_Q = 0$	$w'_M = 0$
free end	$w''_M = 0$	$w'_Q = 0$

Table 4.1: Three different types of boundary conditions for both ends of the sandwich beams

4.2 Derivation of Beam Bending Formula

With these differential equations, it is possible to derive a deformation formula with coefficients corresponding to different support or loading cases. For one example case the procedure will be shown.

The case of interest contains a sandwich beam, which is supported on both ends freely. The load is manifested as an equally distributed force across the whole line. A general sketch of the setup can be seen in figure 4.2.

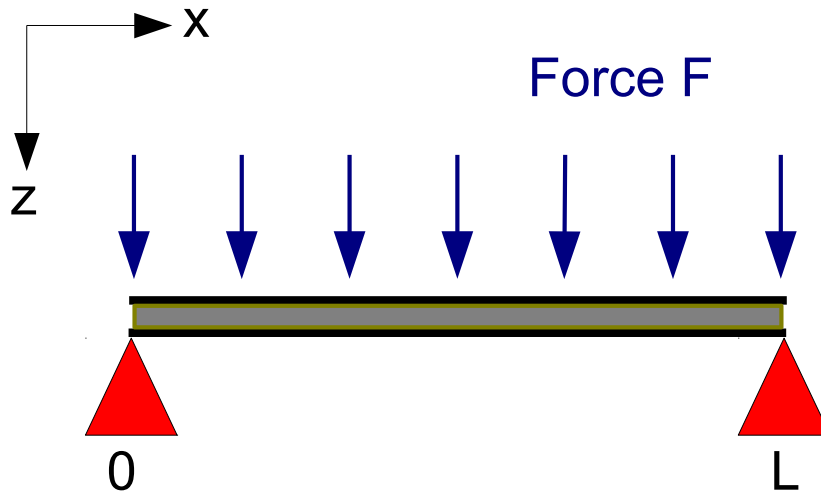


Figure 4.2: Setup for beam bending example

The first thing needed for equation 4.30 and 4.31 are the bending moment M and the shear force Q for this scenario.

$$M = \frac{F}{2L}x(L - x) \quad (4.32)$$

$$Q = \frac{F}{L}\left(\frac{L}{2} - x\right) \quad (4.33)$$

The bending moment M for simply supported ends has to be zero at the end of the beam. It has a maximum at $x = \frac{L}{2}$. The shear force Q is zero, where M has its maximum.

If the expressions 4.32 and 4.33 are inserted in 4.30 and 4.31 the following differential equations are obtained:

$$w''_M = -\frac{F}{2LD}x(L - x) \quad (4.34)$$

$$w'_Q = \frac{F}{LS}\left(\frac{L}{2} - x\right) \quad (4.35)$$

These equations are integrated to get w_M and w_Q .

$$w_M = -\frac{F}{2LD}x\left(\frac{1}{6}Lx^3 - \frac{1}{12}x^4\right) + ax + b \quad (4.36)$$

$$w_Q = \frac{F}{2S} \left(x - \frac{x^2}{L} \right) + c \quad (4.37)$$

Now the boundary conditions can be applied. The first one for this case here is

$$w_M + w_Q \stackrel{!}{=} 0,$$

which yields:

$$\begin{aligned} x = 0 : \quad & b + c = 0 \\ x = L : \quad & a = \frac{FL^2}{24D}. \end{aligned}$$

The integration constants a, b and c have to be inserted in 4.36 and 4.37. When the deformation in the middle of the beam is of interest, then $x = \frac{L}{2}$ has to be inserted in both equations at this point. This will lead to:

$$w_M = \frac{5}{384} \frac{FL^3}{D} \quad (4.38)$$

$$w_Q = \frac{1}{8} \frac{FL}{S} \quad (4.39)$$

Since the method of partial deformations split up the total deformation of the beam into two parts, it is at last possible to present a formula (4.40) which describes the total deformation of a sandwich beam in the middle under various conditions. Therefore w_M and w_Q just have to be added. If different loading or support cases want to be considered, the coefficients k_b and k_s have to be chosen from table 4.2 according to the conditions of the beam bending scenario.

$$\boxed{w = k_b \frac{FL^3}{D} + k_s \frac{FL}{S}} \quad (4.40)$$

The dominating part of the deformation of a sandwich beam is proportional to the length L^3 and proportional to $1/a^2$, which is the distance between the middle of each of the two facing sheets. The deformation is also proportional to $1/t$, where t is the thickness of the facing sheets.

The case in the example has both ends simply supported and the load is distributed uniformly across the beam. Therefore the coefficients $k_b = \frac{5}{384}$ and $k_s = \frac{1}{8}$ should have these values.

Bending conditions	k_b	k_s
both ends simple support + uniform load	$\frac{5}{384}$	$\frac{1}{8}$
both ends fixed + uniform load	$\frac{1}{384}$	$\frac{1}{8}$
both ends simple support + central load	$\frac{1}{48}$	$\frac{1}{4}$
both ends fixed + central load	$\frac{1}{192}$	$\frac{1}{4}$
one end fixed, one free + uniform load	$\frac{1}{8}$	$\frac{1}{2}$
one end fixed, one free + load one end	$\frac{1}{3}$	1

Table 4.2: Coefficients for Sandwich Beam Bending

4.3 Beam Bending Example

In this section equation 4.40 is used to give an example of a sandwich beam bending process. In the example the sandwich beam consists of seven layers. The core in the middle, getting sandwiched by a 200 μm glue layer, 500 μm FR4 layer and a 35 μm copper layer in the outermost position. The specifications and parameters for the sandwich beam are summarized in table 4.3. The parameters t_G, t_F and t_C are the thicknesses of the glue, FR4 and copper layer. E means E-modulus of the different materials.

F	=	55.6 N
b	=	1.07 m
l	=	1.10 m
h	=	0.06 m
t_G	=	200 μm
t_F	=	500 μm
t_C	=	35 μm
E_G	=	1.9×10^9 Pa
E_F	=	19×10^9 Pa
E_C	=	110×10^9 Pa
G	=	2.8×10^8 Pa

Table 4.3: Parameters for Sandwich Beam Bending Example

For the bending scenario here the beam is supported on two sides simply. It is loaded in the middle with a force F. To account for the three facing sheet layers with different thicknesses and materials, three bending stiffnesses D_G, D_F and D_C have to be calculated first. The bending stiffness D is defined in 4.15. Furthermore the total

bending stiffness of the beam consists of the sum of the bending stiffnesses of the facing sheets.

$$D_G = \frac{E_G b}{2} t_G (t_G + h)^2 = 737 \text{ N m}^2$$

$$D_F = \frac{E_F b}{2} t_F (t_F + h + 2t_G)^2 = 18\,850 \text{ N m}^2$$

$$D_C = \frac{E_C b}{2} t_C (t_C + h + 2t_G + 2t_F)^2 = 7774 \text{ N m}^2$$

This results in a total bending stiffness:

$$D = D_G + D_F + D_C = 27\,361 \text{ N m}^2$$

The next step is the calculation of the shear stiffness S:

$$S = \frac{G b}{h} (h + t_G + t_F + t_C)^2 = 18\,419\,110 \text{ N}$$

The deformation of the beam in the middle can now be calculated by inserting everything in equation 4.40:

$$w = \frac{\frac{1}{48} \cdot 55.6 \text{ N} \cdot (1.10 \text{ m})^3}{27\,361 \text{ N m}^2} + \frac{\frac{1}{4} \cdot 55.6 \text{ N} \cdot 1.10 \text{ m}}{18\,419\,110 \text{ N}} = 56.3 \mu\text{m} + 0.83 \mu\text{m} = \underline{\underline{57.1 \mu\text{m}}}$$

When comparing this result with figure 7.5 and figure 7.6, which show a bending experiment and the corresponding ANSYS simulation of the same problem, the sandwich beam theory is in accordance with not only the experiment but also the simulation. The force F used for the calculations here is corresponding with the weight of a 0.5 litre lead brick.

If the stiffness or deformation of a sandwich design is of interest here, the second part of the formula describing the deformation coming from the core shear can usually be neglected. It is generally much smaller than the first part coming from the bending of the facing sheets. If the honeycomb thickness is for example 1 cm instead of 6 cm the effect would be even stronger than it is in the calculations above. Since the thickness of the facing sheets is small compared to the thickness of the honeycomb core, the first part of equation 4.40 has a $\sim 1/h^2$ dependency and the second part a $\sim 1/h$. This simply means the thicker the honeycomb, the more contribution will the deformation induced by the core shear have.

The equation 4.40 is a good and simple way to describe the deformation of sandwich beams. The equation makes use of the bending stiffness D, which is on its own a good parameter to evaluate the stiffness of sandwich designs.

5 Construction of Sandwich Panels

This chapter discusses the construction of the Micromegas quadruplets of the New Small Wheel. As mentioned in the introduction, it is divided in eight small and eight large sectors. Each trapezoidal sector is divided into two parts. The large sector is divided into the 3m² large LM1 and LM2 module. The small one into the 2 m² SM1 and SM2. A collaboration of the German universities of Freiburg, Munich (LMU), Mainz and Würzburg is taking care of the construction of the SM2 module. Before the production of the SM2 module can start, a prototype has to be built to verify the production methodology.

5.1 Construction Method for First Prototype

The dimensions of the SM2 module and the mechanical prototype M1 are shown in figure 5.1. The outer dimensions including the green part represent the dimensions of the readout panel. The inner part, without the green area represents the drift panel. The readout panels are larger because they need additional space for the readout electronics.

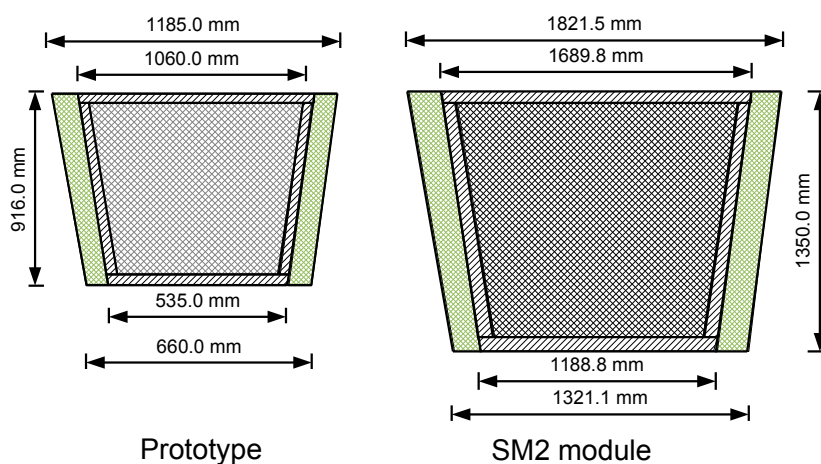


Figure 5.1: Dimensions of drift and readout panel of the prototype and the SM2 module

A sketch of the quadruplet layout is shown in figure 5.2. Each micromegas quadruplet consists of five sandwich panels which make up four micromegas detectors. A sandwich panel is a plate consisting of several layers leading to exceptional plate properties. The means such a panel can have a high stiffness with relatively low weight. Usually they consist of three layers. The two on the top and bottom are called facing sheets and they define the bending stiffness of the panel. For the case

here they are made of FR4. In the middle is the core, a light-weight material. It keeps the two facing sheets at constant distance. The material used here is aluminium honeycomb. The idea of this setup is to gain light weight plates with remarkable stiffness. These panels can be divided into two different panel types. Namely the drift and the readout panel. The first panel type has in comparison to the other type a 35 μm copper layer on top of the FR4. The inner copper layer is the cathode for a micromegas detector.

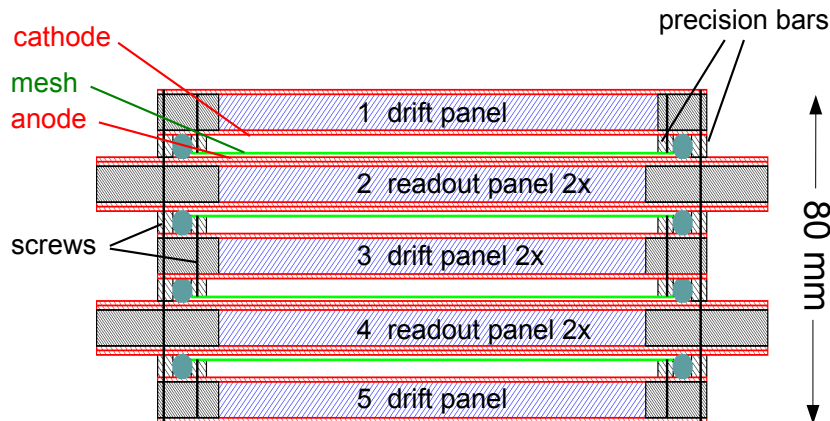


Figure 5.2: Schematic of a Micromegas quadruplet in side view, taken from [Hertenberger, 2014]

The space between a drift panel and a readout panel is defined by 5.17 mm thick precision bars defining the drift region for the micromegas detector. Both sides of the readout panels are covered with the readout strips of the anode. These copper strips have a width of 300 μm and a pitch of about 450 μm . 128 μm above the readout strips is a stretched steel mesh, which separates the drift and amplification region. This distance is ensured by many round pillars with a diameter of 0.3 mm and 7 mm of distance to each other.

It is known from chapter 3 that the micromegas detector consists of planar layers which are parallel to each other. For the case here it means, that the sandwich panels, defining the layers of the detector, only have to have a parallelism of the surfaces of the same sandwiches of better than 80 μm to ensure a spatial resolution of the micromegas detector below 100 μm in a single plane.

The production process of sandwich panels with these qualities is described in the following. The construction of drift panels can be divided up in two steps. A schematic figure of the process can be seen in figure 5.3. For both steps a granite table with a surface as flat as possible is required. Good granite tables have a acceptable deviation from the perfect plane in the orders of a few micro meters. The newly purchased granite table, which will be used for the production of the actual panels of the SM2 modul is specified to have a deviation from minimum to maximum below 6 μm . Actual measurements stated the distance to be smaller than 5 μm .

The table used for the first production step of the prototype is from the "Max-Planck-Institut für Physik". The second step has been performed partly on the table from the MPI and an old table at the facilities here, which unfortunately has a maximum deformation due to sagging of about 150 μm .

In the first production step a steel mesh is laid onto the granite table. On top of it the

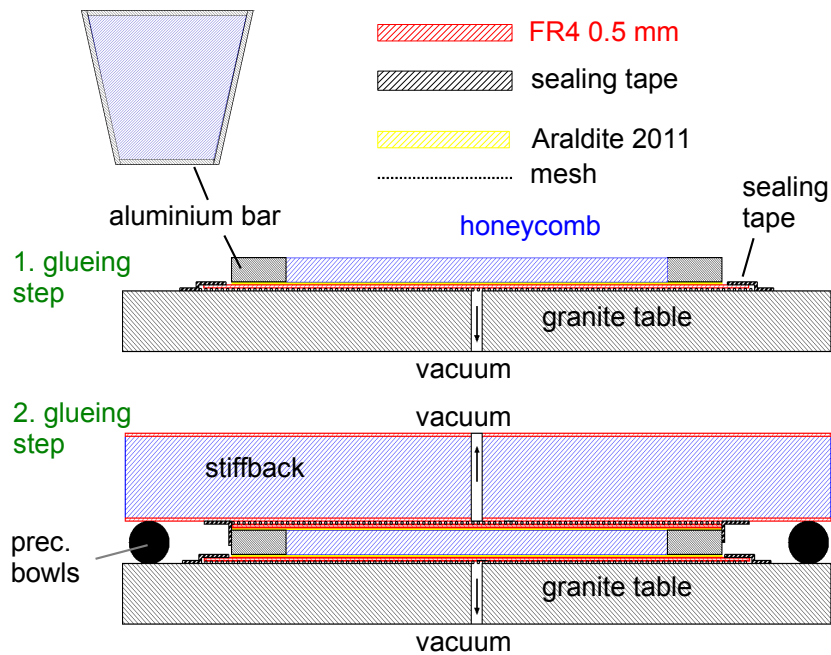


Figure 5.3: Schematic of the glueing process in two steps using a planar stiff holding structure, the so called "stiffback", taken from [Hertenberger, 2014]

first FR4 panel is placed and the space between the FR4 and the granite table is sealed with tape. It is needed because the FR4 panel needs to be pressed down to the granite table to transfer the planarity of the table to the first part of the panel. Eventual creases in the mesh would be transferred as well. Since the surface of the FR4 and especially the copper is so smooth the mesh is needed to distribute the vacuum across the whole plate. The vacuum pump can either be connected to holes in the table or directly to the mesh. With proper isolation both methods work. The FR4 plate, which should have been roughened up beforehand with fine abrasive paper, should be cleaned with alcohol for the first step of the glueing. As glue the two component epoxy resin Araldite 2011 is used. The goal is to apply a 150 to 200 μm thick glue layer. To accomplish this a serrated spatula with 300 μm deep notches is used. The reason is to form grooves and peaks which will support the bonding of the FR4 and the honeycomb. After glue application the honeycomb and supporting aluminium beams are put on top of the glue. To press it down a simple wood plate has been used. After a day of curing the first step of the glueing is finished. A photo of the glueing of the first step is shown in figure 5.4.

In the second step of the glueing additionally to the first setup a stiffback and precision bowls are needed. The stiffback is a light weight auxiliary structure, which is very stiff and has a planar surface similar to the granite table. Detailed information about the stiffback is presented in chapter 7. The second step starts the same way as the first step. The second FR4 layer is put on top of an auxiliary mesh, which is placed on the granite table. The roughening up and the cleaning is repeated for this side as well. The glue application is the same as well. The honeycomb glued to the first FR4 sheet is sucked to the stiffback by a mesh the same way it has been sucked to the granite table in the first step of the glueing before. This element of the first step



Figure 5.4: Photo of the glueing of the first side. The aluminium bars and the honeycomb are already on the FR4 sheet. Photograph taken from [Hertenberger, 2014].

of the glueing hanging on the stiffback is then placed on the precision bowls, which define the exact distance between the granite table and the stiffback, to assure the parallelicity of the two facing sheets of the sandwich. For the prototype produced this way only four precision bowls have been used. In retrospective it has become apparent that four pieces of support are not sufficient because of the deformation of the stiffback. This issue again is addressed in chapter 7. After curing of the glue the vacuum pumps are switched off and the sealing tape has to be removed. It has proven to be useful to attach strings at one end of the sealing tape to be able to peel it off easily. After these steps the production of a drift panel is complete. The first prototype quadruplet does only consist of the sandwich panels built with this method. After screwing them together the result can be seen in figure 5.5.

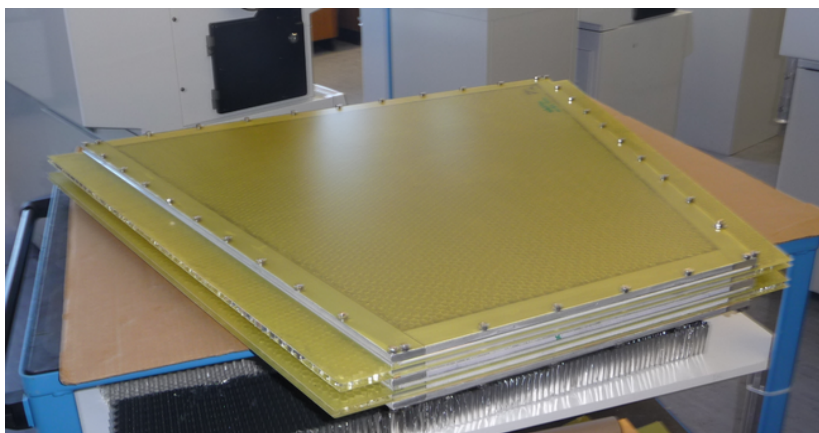


Figure 5.5: Photo of the mechanical prototype quadruplet, built for mechanical and thermal stress-tests in Freiburg. It is foreseen to be upgraded to a fully working module. Photograph taken from [Hertenberger, 2014]

5.2 Production Process of Readout Panels

In comparison to the readout panels in the prototype, the real ones are not plain FR4 sheets. For the production of the actual SM2 module they are already equipped with the readout strips, a kapton layer and the pillars on top of it. This means that one side of each FR4 panel used for the readout sandwich is equipped with these pillars. This side of the panel is getting sucked to the granite table and the stiffback respectively. The good thing is, that these pillars can replace the mesh to distribute the vacuum. With proper sealing of the border between the FR4 plate and the granite table the mesh can be omitted, which fastens the production process compared to the one introduced for the prototype. Requirement is, that the table and the stiffback do have holes for the vacuum connection. The new granite table in the facilities present here does have such holes.

To see if this method is viable an ANSYS simulation has been performed to investigate the behaviour of the FR4 when the vacuum is applied. A Shell281 element has been used therefore to simulate the 0.5 mm thick FR4 plate. The pillars have been chosen to be arranged in a hexagonal grid with 6 mm distance to each other. The area in the simulation where the FR4 and the pillars touch has been constrained in all moving directions. An equally distributed pressure of 0.5 bar on the simulated segment of the FR4 is simulated. The result of the simulation is shown in figure 5.6.

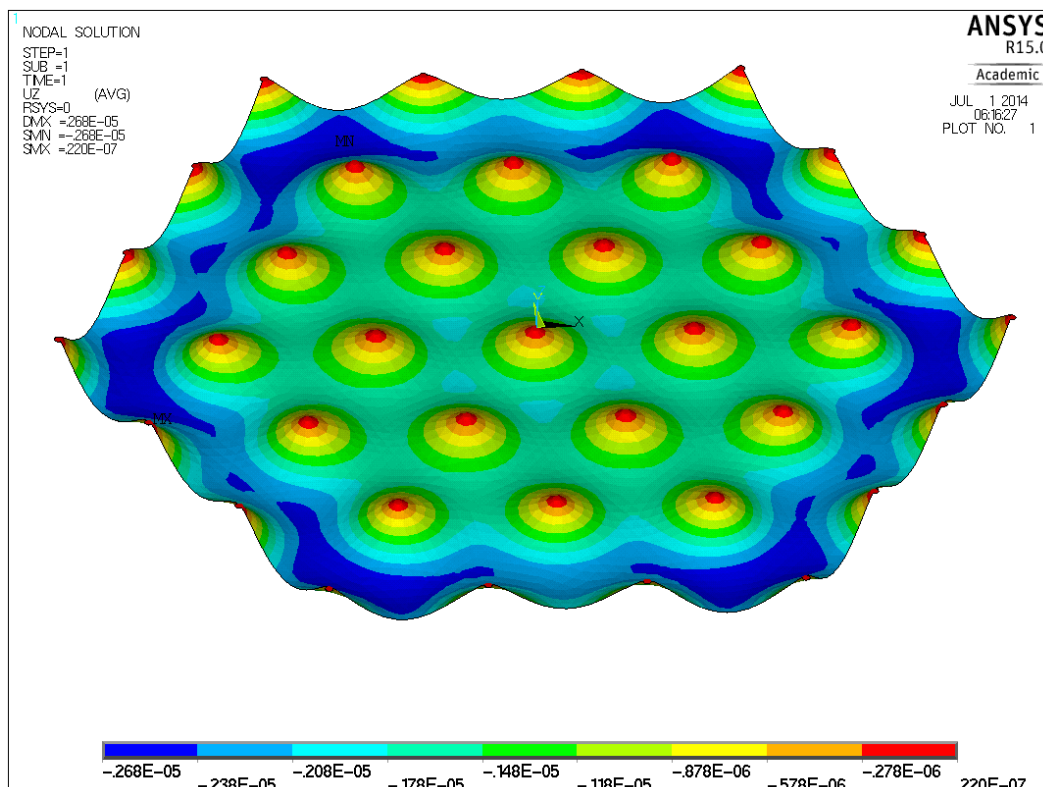


Figure 5.6: ANSYS simulation of a 0.5 mm thick FR4 layer placed on pillars with distance 6 mm to each other under 0.5 bar over pressure

It can be seen, that the maximum deformation is about 1.9 μm in relevant areas. This is in the valley of the inner hexagonal cell. The other pillars are used to minimize bound-

ary effects, which lead to deformations depicted as dark-blue in the figure. Since the deformation goes linear with the applied pressure load, it can be said, that even under full vacuum the deformation is only 3.8 μm . This means, that this method can be used without problems to fixate the FR4 panels of the readout panels to the granite table and the stiffback respectively. Besides the issue with the mesh, the general production process remains the same as for the prototype.

This chapter has explained the production process of the two different sandwich panel types. By means of the mechanical prototype the process for the drift panels has been explained. The process for the readout panels has been presented as well. This has not been tested in practice, but a simulation in ANSYS shows the feasibility of the concept.

6 Surface Measurements of Sandwich Panels

This chapter provides mainly insight in different measurement techniques to obtain information about the planarity of sandwich panels. Additionally one experiment was conducted to get the E-modulus of FR4 for simulation purposes.

6.1 Determination of the E-Modulus of FR4

In this section a small experiment is described to determine the E-modulus value of FR4, since literature values vary very much. The purpose is to increase accuracy for all simulations in which this material is used. To get the E-modulus a beam bending experiment with a strip of 0.5 mm thick FR4 is executed. The strip is a rectangle beam like structure with the dimensions 62.6 cm × 12.8 cm. The piece of FR4 is simply supported on each end. Additionally the distance between the two support blocks is 50 cm in the first case, which is depicted in 6.1(a). In the second case shown in 6.1(b) the distance is 62.3 cm. Different lengths of the beam lead to different deformations under the same load, which is always gravity only.



(a) 50 cm support distance

(b) 62.3 cm support distance

Figure 6.1: Bending experiment of a FR4 beam, which is simply supported on two sides and only deforms due to its own weight. Simple support means no restriction to rotational boundary conditions, but only translational. The plates are supported as indicated in the figure.

The distance between the minimum of the FR4 and the granite table is measured with a sliding gauge. This value has to be subtracted from the height of the red support blocks, which is 10.0 cm. This difference is the displacement of the FR4 beam under its own weight. For the first case 3.5 ± 0.1 cm deformation can be measured. For the second case 9.0 ± 0.1 cm.

To make use of this information an ANSYS simulation will be performed. Therefore a rectangle with dimensions 62.3 cm × 12.8 cm is built. As element type SHELL181 is used. To simulate one of the two beam bending scenarios both ends at 62.3 cm distance have their degrees of freedom in x,y and z direction restricted to zero. This represents simply supported beam ends. For the second case the FR4 area remains the same, but the distance between the two simply supports is only 50 cm. This means there is an overhang of 6.15 cm on each side. Since the density of the material is well known, gravity can easily be applied to simulate the deformation under its own weight. For both cases the E-modulus in x and y direction is varied until the deformation in the simulation matches the measured deformations from the experiment above.

For the first case a deformation of 3.5 cm leads to an E-modulus of 19.0 GPa in x and y direction. The corresponding simulation plot can be seen in 6.2(a). When the distance between the supports is 62.3 cm and with the same E-modulus as in the first case, it leads to a displacement of 9.1 cm. This can be seen in 6.2(b).

An E-modulus of 19.0 GPa in x and y direction of the FR4, which will be used for the sandwich panels allows to describe the measured gravitational deformations of FR4 very well in ANSYS.

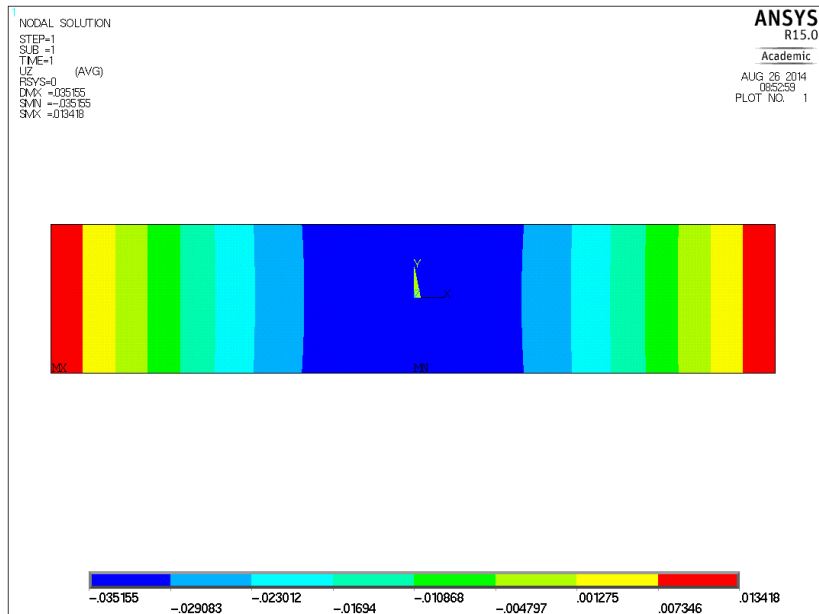
6.2 Planarity Measurement using a Straight Edge

Since the goal is to build very planar sandwich structures, it is mandatory to be able to check the planarity of the surfaces of the plates. Therefore three different measurement types will be presented.

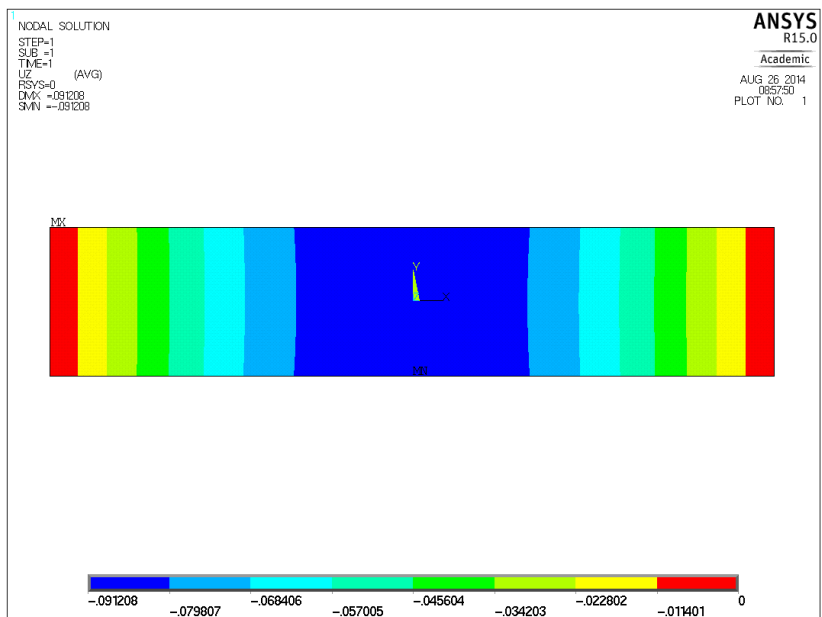
The first approach is making use of a straight edge. This is a tapered precision ruler, which can be seen in figure 6.3. The deviation from a perfect line is in the order of about 10 μm. The simplest and fastest method to get a rough overview of the deformation of the panel is to put the straight edge directly on the panel. If the panel is bent a light gap between the straight edge and the panel is visible. This will not amount to explicit deformation values but will give a quick estimation of the panel quality.

The next step to get real deformation values requires an additional granite table, precision blocks and a feeler gauge. The panel rests on the granite table between two precision blocks. On top of these the straight edge is placed. To measure the distance between the straight edge and the panel a feeler gauge is inserted in the gap. Usually a precision of 50 μm can be achieved depending on the feeler gauge.

To put this method to the test, the surface of a sandwich panel has been measured. The setup of the measurement can be seen in 6.3. In this measurement the straight edge is moved in 2.5 cm steps. For each step the distance and the corresponding location is obtained with the feeler gauge. Putting the information from all lines together one obtains the plot in figure 6.4(a). Compared to a measurement from a computerized measurement machine (CMM) as in figure 6.4(b), it does display similarities and



(a) ANSYS simulation with $E=19.0$ GPa and 50 cm support distance suggesting a deformation of about 3.5 cm



(b) ANSYS simulation with $E=19.0$ GPa and 62.3 cm support distance suggesting a deformation of about 9.1 cm

Figure 6.2: ANSYS simulation with different support distances

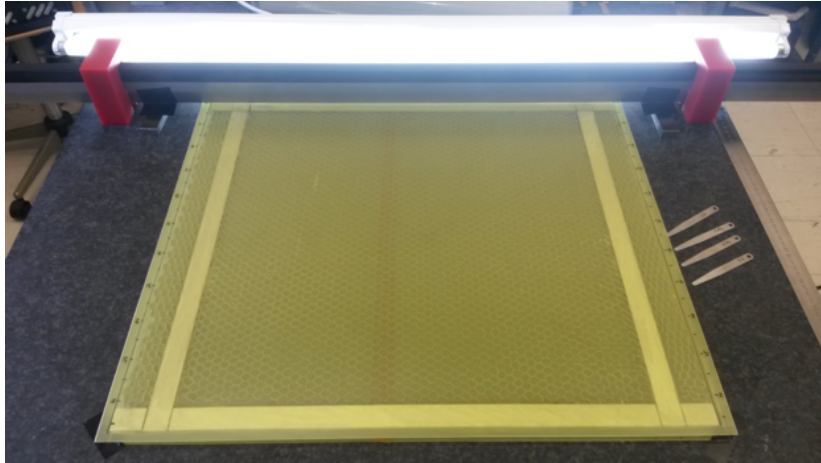


Figure 6.3: Surface measurement with straight edge and feeler gauge

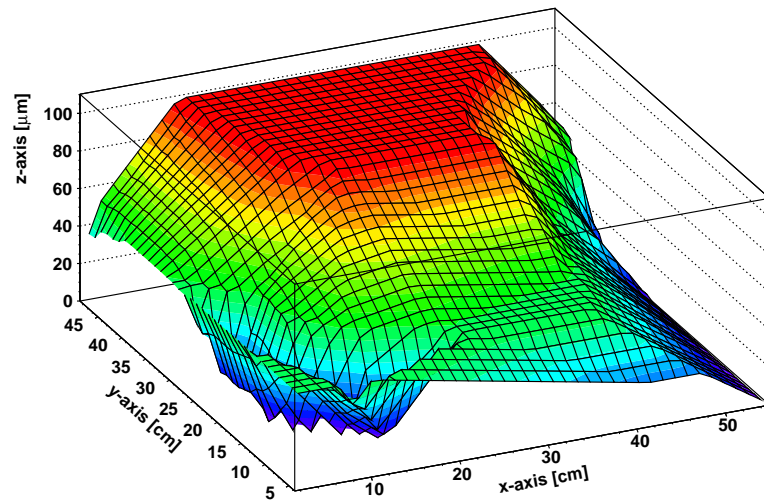
differences. The front left corner of both plots in figure 6.4(a) show a bulge. Another similarity is the steep decrease of the surface visible in the rear left corner. A big difference is the total maximum deformation, which is $100\ \mu\text{m}$ in the straight edge measurement and $160\ \mu\text{m}$ in the CMM measurement. This difference is coming from a combined effect of the sagging of the straight edge and the concomitant decrease of the difference between the straight edge and the sandwich and a possible kink in the feeler gauge, used to measure the differences in this region.

Conclusively this method with an accuracy defined by the step width of $50\ \mu\text{m}$ of the feeler gauge is not viable for the exact surface scan of the sandwich panels. It is a simple and cheap method, but it costs a lot of time and lacks the accuracy. But nevertheless the straight edge is a good choice when quickly checking the global curvature of a plate by laying it directly on a plate and checking for light gaps and deformations bigger than $50\ \mu\text{m}$ with an feeler gauge.

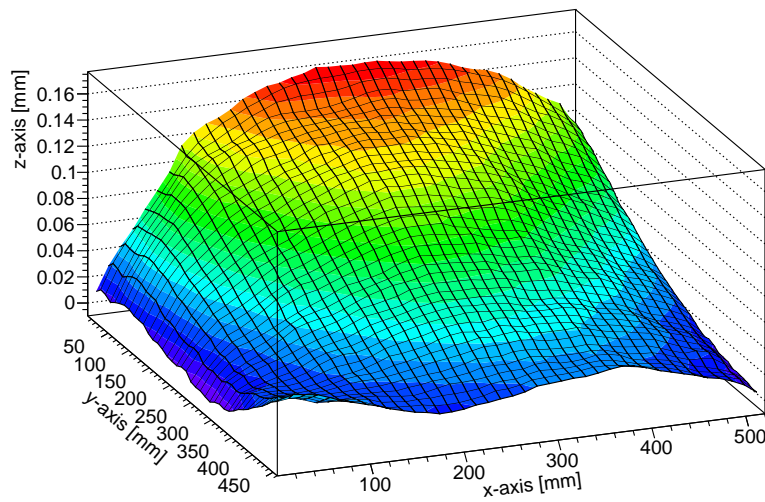
6.3 Deflection Measurement using an Interferometer

The next method results in measuring a height difference along a line with an interferometer. If this is performed several times along equally displaced lines it is possible to gain 3D surface information of a plate. For this task the ML10 measurement system from Renishaw is used. It consists of a stabilized Helium-Neon laser, interferometer and a reflector. The experimental setup can be seen in figure 6.5. The laser is on the bottom right and the interferometer is in the middle of the picture at the basis of the trapezoidal sandwich panel. The reflector can be seen at the end of the guiding bar.

The measurement principle is described in the following. The laser sends out a continuous light beam. Along its path stands the interferometer, which works like a Wollaston prism. It divides the laser beam into two divergent beams with a small angle between them. These beams run towards the reflector where they are sent back parallel to the incoming beams by mirrors. The interferometer is moved along the guiding bar. If the height of the interferometer changes from the initial



(a) Surface measurement with straight edge



(b) Surface measurement with CMM machine

Figure 6.4: Plots of the same surface using different measurement techniques



Figure 6.5: Experimental setup for an interferometer measurement. The ML10 laser is in the right bottom corner, the straightness interferometer in the middle at the beginning of the guiding bar and the reflector is in the left top corner at the end of the guiding bar. The guiding bar is the aluminium profile in the middle of the trapezoidal area.

calibration level, the optical path length for one beam increases whereas the other beams length decreases. This is due to the three wedge structure of the straightness interferometer, which can be seen in figure 6.6. The explanation of the straightness interferometer follows [Chapman et al., 2013]. The wedges consist of birefringent crystals, which have a refractive index, that varies according to the orientation of their crystal axes and the polarisation of the light travelling through them. When light is transmitted through such a material as two linear polarisations oriented parallel and perpendicular to the crystals optic axis, one polarisation will see a slightly higher refractive index and will travel more slowly, whilst the other will see a lower refractive index and will travel more quickly. The orientation of the optical axes of the two outer wedges are the same. The one in the middle is the corresponding other one. The differential refraction within the Wollaston prism, which causes the beams to diverge is the reason why the optic can be used to measure the height differences. S denotes the height change of the interferometer. H and L represent regions where the polarised laser beams see more material, which they see as having the lower (L) or the higher (H) refractive index, which changes their optical path length accordingly.

The reflected beams come back to the interferometer and interfere. From there the beam goes back to a sensor right next to the laser source where not only the intensity of the beam is measured, but also the number of constructive/destructive interferences is counted. This gives the height information. When measuring the height differences along a line of a panel it is therefore important that the laser beam may not be interrupted during the measurement. The interferometer may only be moved along the line since the interferometer can only measure relative changes in length. The laser beam paths are illustrated in 6.7.

To gain 3D surface information with the method described above, the height differences in each line have to be put in relation to each other. Therefore additional measurements along a line rectangular to these line measurements have to be per-

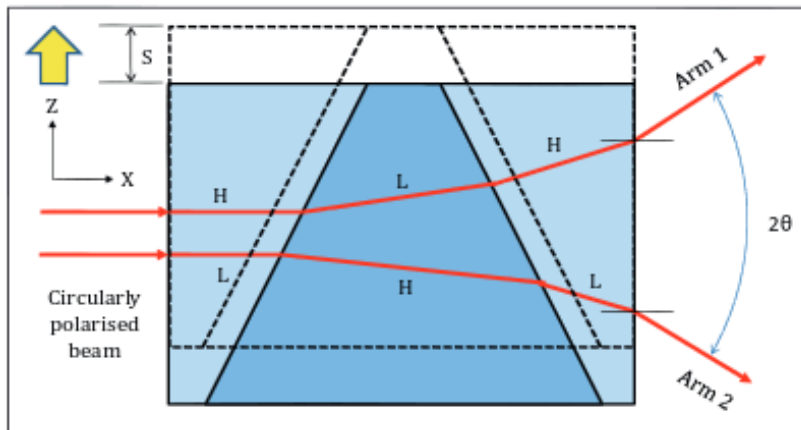


Figure 6.6: Sketch of a Renishaw straightness interferometer in side view, taken from [Chapman et al., 2013]

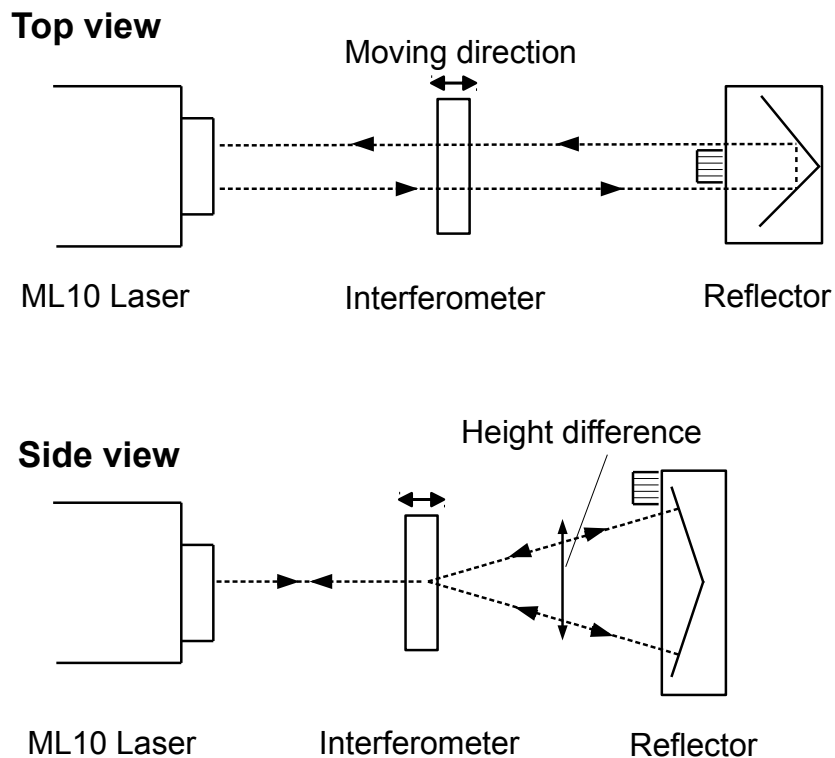


Figure 6.7: Course of laser beam in measurement; the mirror is a reflector like a cat's eye meaning the laser beam is sent back parallel to its incoming direction

formed. It is then possible to obtain a 3D plot of the surface. In the case here all measurements have been performed on a granite table and in a temperature stabilized room at about $(22 \pm 0.5)^\circ\text{C}$. Since the laser is standing on a tripod in the room, the laser beam and the granite table surface are not parallel to each other. An additional correction therefore has to be added. The result of one measurement of the surface of an sandwich trapezoid can be seen in 6.8. In this figure a 50 cm broad section of an trapezoidal readout sandwich panel can be seen. It contains 1067 measurement points. For each measurement point between 10 s and 15 s are needed. That is the reason for only this section having been measured. To rate the interferometer technique for surface measurement figure 6.8 can be compared with 6.9, which shows a measurement with a CMM. In both figures of the measurements the corner farthest in the back and the one in the right corner are showing the same corners of the sandwich panel. The corner in the left and the one in the front are not the same, since the measurement with the interferometer only shows a section of the total panel. In figure 6.8 is a flat plateau at $z=0$ visible. The measurement region is trapezoidal and the histogram is filled with the entry value zero, when there is no measurement data available at this point. The same happens on both sides for the histogram showing the CMM measurement, but the default entry value is the mean value in this case.

The right border of the trapezoid in both surface plots show a height difference between $250\ \mu\text{m}$ and $300\ \mu\text{m}$. The left border of figure 6.8 does have a difference of about $100\ \mu\text{m}$, whereas the line at $x=280\ \text{mm}$ in figure 6.9 has a height difference between $50\ \mu\text{m}$ and $100\ \mu\text{m}$. The largest discrepancy of both plots can be found along the line, which is parallel to the line where $y=0$, in figure 6.8. It is about $125\ \mu\text{m}$ compared to $200\ \mu\text{m}$ in the CMM measurement.

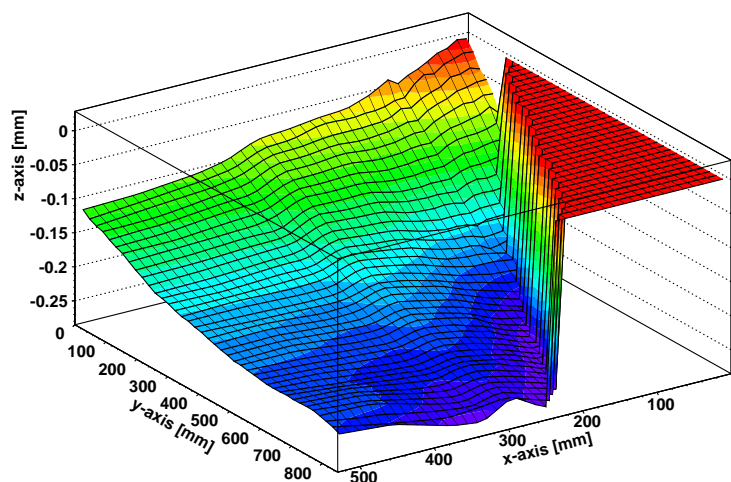


Figure 6.8: Surface measurement with the interferometer of a section of a trapezoidal sandwich panel. The red plateau in the right corner is the area where no measurement point is and the histogram is filled with default zero entries.

The general appearance is described correctly, but evidently there are some differences compared to the CMM measurement. One cause is that the interferometer is standing on a tripod and therefore a measurement of a single point on the surface is

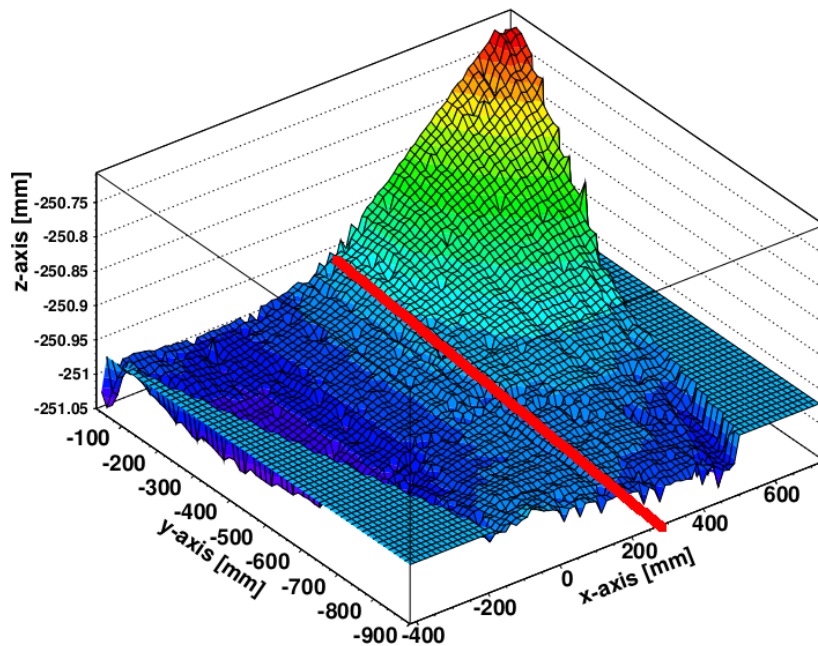


Figure 6.9: Surface measurement of the whole trapezoidal sandwich with a CMM machine; the right side of the red line can be compared with the interferometer measurement

not possible. The tripod can be seen in 6.10.



Figure 6.10: Tripod pedestal of the interferometer

This issue can be solved if a moveable sleigh, which is mounted onto the guiding bar, is built. The sleigh needs to have a hole, in which the pedestal with only a single point-like foot is inserted. The thickness of the sleigh and the diameter of the hole needs to be chosen in such a way, that the interferometer on its foot can only move in a direction perpendicular to the sleigh plate and has as little margin as possible left in all other directions. If the sleigh is moved along the guide bar to each measurement point, gravity is always taking care of the interferometer pedestal to be in contact with the surface. This allows a interferometer height measurement of points and not a plane defined by the three tripod footings.

Another influence for the difference may be the method of relating all lines to only one base-line, which is perpendicular to all other measurement lines. If there is an

erroneous data point in the base-line measurement, the whole line perpendicular to it will be shifted. Furthermore the correction for the not parallel laser beam and the granite table may be incomplete, since the slightly bent state of the granite table is completely neglected. For this correction one line on the granite table is measured with the interferometer. Then a line is fitted through all these points. With the help of these line parameters, all line measurements of the sandwich panel are to be corrected.

This method is not recommendable. In different plate measurements using the same methodology the problems were always the same. The initial calibration and the measurement itself take a lot of time. Furthermore errors can easily be made by putting all data together with the right corrections. But this method is nevertheless more accurate than the straight-edge method introduced in the section before. It also has to be mentioned that theoretically this method is by far the most accurate. But because of the tripod of the interferometer a scan of the surface deformation is not feasible.

6.4 Deflection Measurement with a CMM

This section describes the measurement of surfaces with a coordinate measuring machine (CMM). These can be operated manually or via computer. These machines have a probe head, which can be moved in all directions. Such a head presses on a point on the surface of the panel to be measured panel. If a certain force value is reached in the probe head, the coordinates of the head will be written to a file. The measurement of the surface of a sandwich drift panel is shown in figure 6.11. With a length of 1060 mm and a width of 916 mm, this drift panel is part of the M1 mechanical micromegas quadruplet prototype.

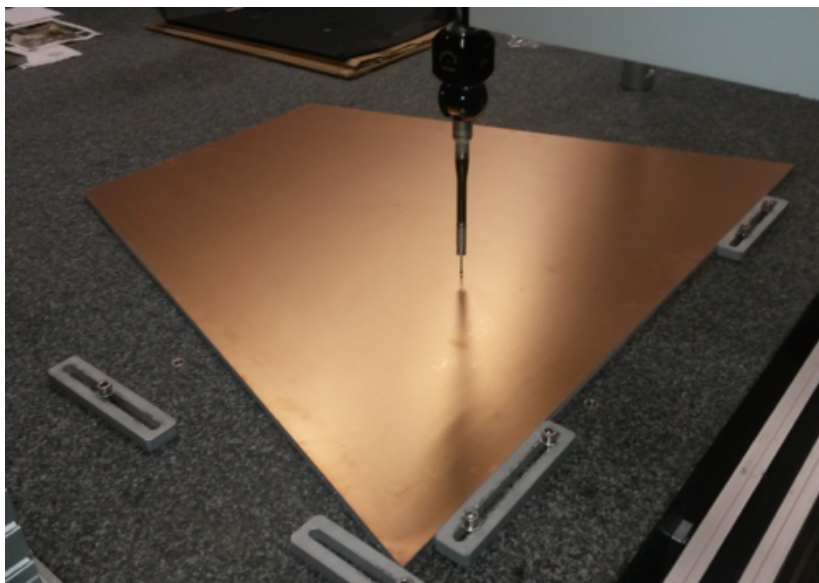


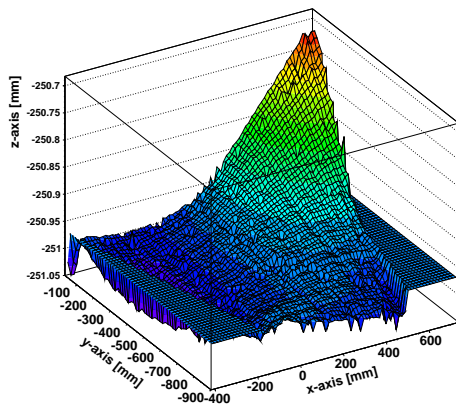
Figure 6.11: Photo of the Freiburg CMM measuring the surface of a drift sandwich panel of the prototype

The prototype consists of two drift panels, two readout panels and a double drift panel. Concerning the construction of flat sandwich panels for the prototype the only difference between these panel types is that a drift panel does have an additional 35 μm copper layer, which will later work as cathode for the micromegas detector. The readout panels are broader than drift panels to hold electronics. To check the quality of these panels and to see how good a CMM works, measurements of all five panels of the micromegas quadruplet have been taken. For the measurements here the grid in x- and y- direction is defined with a distance of 15 mm between two measurement points. Such a grid space means the measurement of the approximate 2500 points will take about two hours for this panel size.

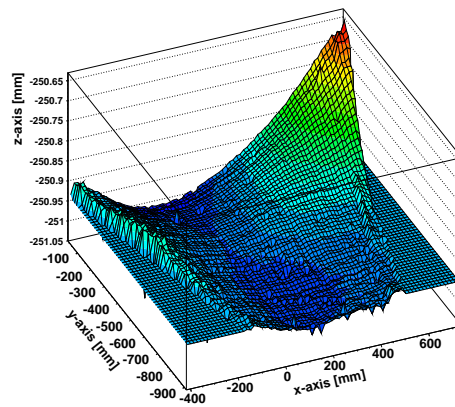
The results are displayed in figure 6.12 and 6.13.

The pictures of the panel side, that was glued in the first step in figure 6.12, show the side of the sandwich panel, which is stuck onto the stiffback during step two of the construction process. Therefore one expects the surface of the side glued first to be adapted to the surface of the stiffback. This means if the stiffback is deformed, this deformation is transferred to the surface of the sandwich panel. All figures of this side have in common, that the right top corner is bent upwards by roughly 0.3 mm. This can be traced back to a stiffback deformation, which is further discussed in chapter 7. Additionally there are other effects. Figure 6.12(a) and 6.12(b) are very similar, but compared to sandwich number two, three and four there is a clear difference. The influence of a different granite table and a different alignment of the steel precision balls can be seen. All steps of the glueing have been performed on the same table except for step two of the glueing of sandwich two, three and four. For the glueing of those three sides another granite table with poor quality has been used. Despite the use of the bad granite table only during the second step of the glueing, the first side is influenced negatively as well. One effect on the side glued during step one of sandwich panel two, three and four comes from the fact, that the stiffback with the FR4 panel attached is deforming in the middle unexpectedly much. This means that the area in the middle of the FR4, that is pressed against the honeycomb during curing, leads to the tubby deformations of sandwich two. The position of the precision steel balls, which are used as distance holders, do make a little effect. For both sides of sandwich panel zero and one the position is the same. For the other three panels the position has been differing.

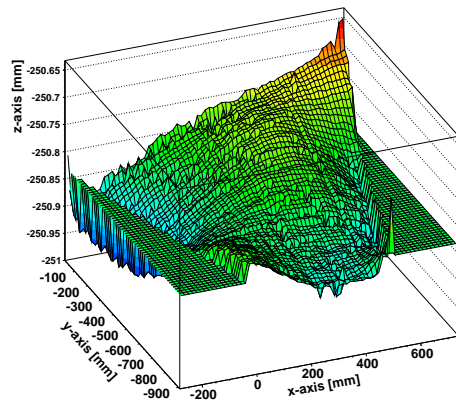
Figure 6.13 displays the side of the sandwiches, which are facing the granite table during the second step of the glueing process. The adaption of the granite table surface to the sandwich is visible. In figure 6.13(a) and figure 6.13(b) there can be seen 10 μm to 15 μm high bumps in straight lines, which cross each other perpendicularly. These are created from grooves in the granite table used to distribute the vacuum between the sandwich and the granite table. Comparing the bumpy disturbances with the planarity of the panel shows for sandwich one excellent planarity in the active area. Figure 6.13(d) and 6.13(e) show the deformed status of the granite table. The groove in the plots where the y-axis has a value of about -300 mm comes from a kink in the auxiliary mesh, which is used to distribute the vacuum on this granite table. Figure 6.13(c) does have the problem, that the distance holder between the sandwich and the granite table did not touch the surface of the granite table properly on one corner, leading to sandwich surfaces, which are not parallel anymore.



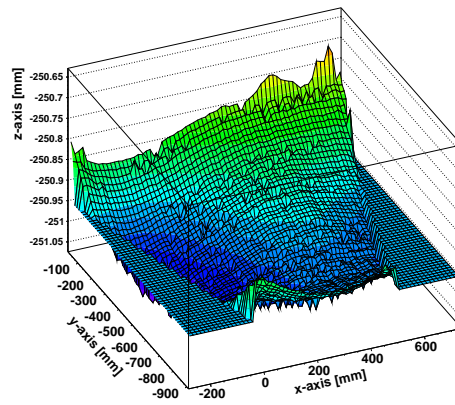
(a) CMM measurement of sandwich 0



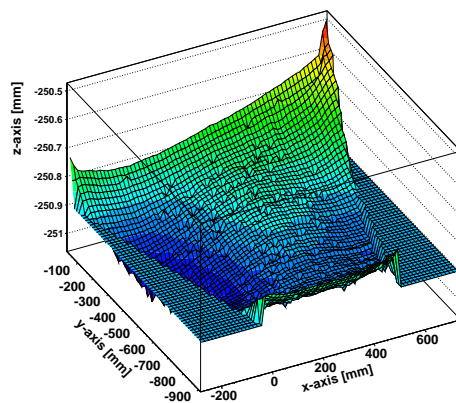
(b) CMM measurement of sandwich 1



(c) CMM measurement of sandwich 2

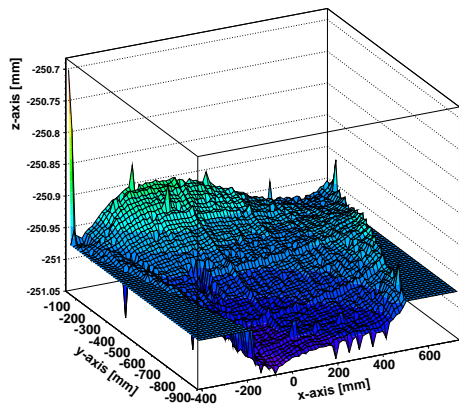


(d) CMM measurement of sandwich 3

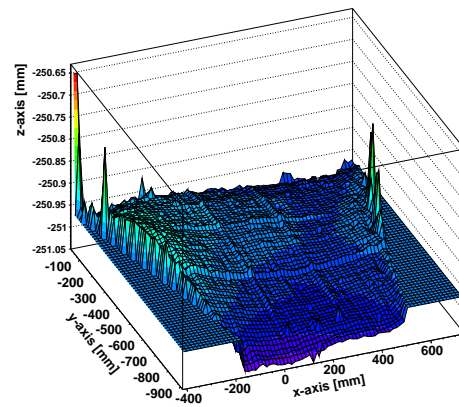


(e) CMM measurement of sandwich 4

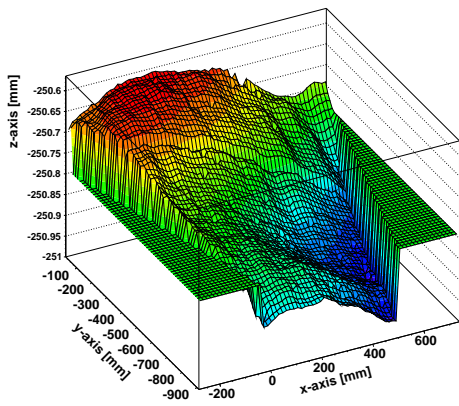
Figure 6.12: Surface measurement of the first glued side of the quadruplet sandwiches; all top right corners are bent by about 0.3 mm, indicating a systematic effect; a non-precise granite table had to be used for the second step of the glueing leading to tubby deformations in the middle area of the first step for sandwich two, three and four



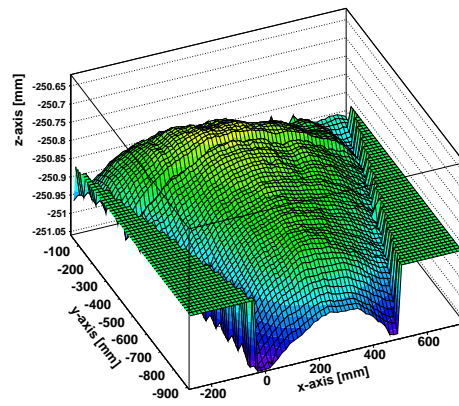
(a) CMM measurement of sandwich 0; vacuum grid in the granite table is visible



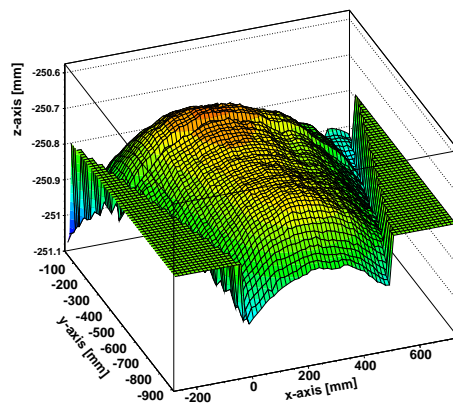
(b) CMM measurement of sandwich 1; vacuum grid in the granite table is visible



(c) CMM measurement of sandwich 2; tilt in the sandwich surfaces is visible



(d) CMM measurement of sandwich 3



(e) CMM measurement of sandwich 4

Figure 6.13: Surface measurement of the side of the quadruplet sandwiches glue in step two; for sandwich zero and one, the precise granite table with a grid of grooves for vacuum distribution is used; the figures for sandwich two, three and four show the influence of a non-precise (=tubby deformation $> 100 \mu\text{m}$) granite table; a kink in the mesh is visible in sandw. two, three and four

After understanding where the deformation in the surfaces come from, it is useful to classify the quality of the panel with a single value. A good possibility is the root mean square of all entries. Since the CMM measurement plots are all in the coordinate system of the machine, a plane is fitted in each plot. In the following the difference x_i between the plot and the fit is written to a histogram. The resulting figures are shown in 6.14 and 6.15. The root mean square is defined as:

$$\text{RMS} = \sqrt{\sum_{i=1}^n \frac{x_i^2}{n}}$$

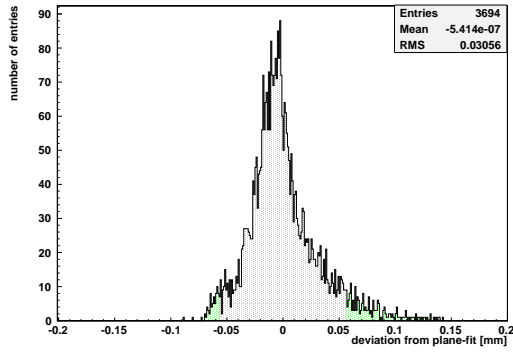
n is the number of the measurement points. The RMS in figures 6.14 and 6.15 covers the range from 0.0159 mm to 0.0653 mm. When comparing the histograms with their corresponding measurement plots, systematic deviations are observed for all panel sides but two, which are the sides of the readout panels, sandwich zero and one, prepared in step two, which can be seen in figure 6.13. Their RMS value is 0.0159 mm and 0.0196 mm. The entries only in these two histograms are equally distributed around the center. Considering only the RMS value allows statements only for purely statistic deviations, without systematic somponents.

Surface measurements by means of a CMM is the most practicable method in comparison to the other investigated methods. The advantages and disadvantages of all previous methods are summarized in table 6.1.

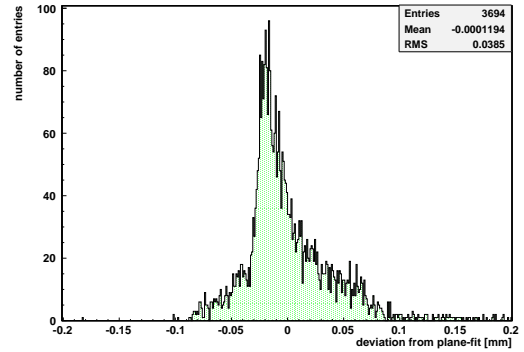
	Straightedge	Interferometer	CMM
Costs	low	medium	high
Time	low	high	medium
Accuracy	low	medium	high
Difficulty	low	high	medium

Table 6.1: Summarized comparison of all three presented methods

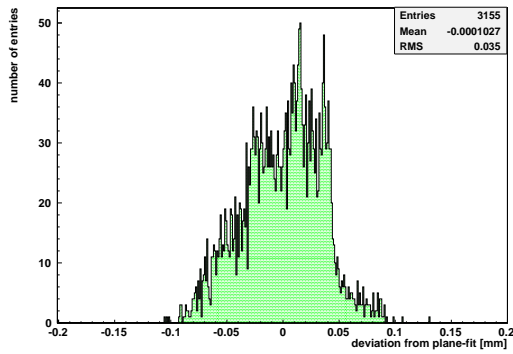
For a quick quality check, the straight edge method is the best. But since the sandwich panels need to have a planarity below 50 μm , the only technique with sufficient accuracy is the CMM. This measurement needs to be performed if real surface information is wanted after panel construction.



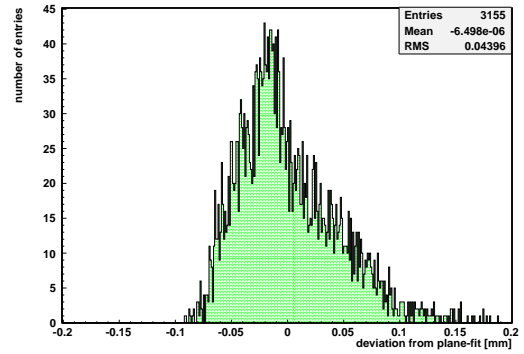
(a) Sandwich 0: Deviation from plane



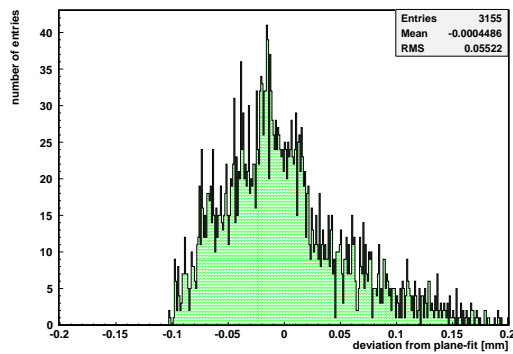
(b) Sandwich 1: Deviation from plane



(c) Sandwich 2: Deviation from plane

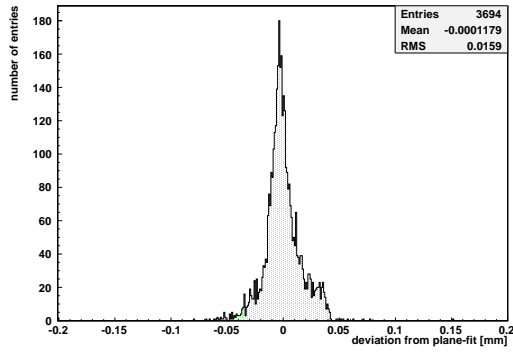


(d) Sandwich 3: Deviation from plane

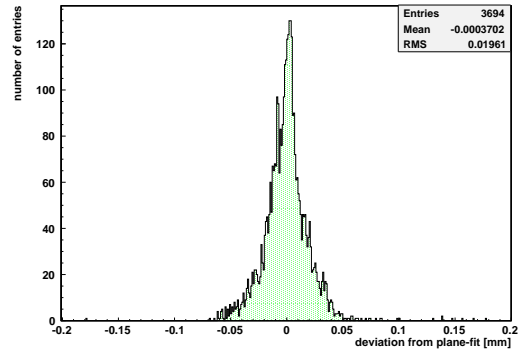


(e) Sandwich 4: Deviation from plane

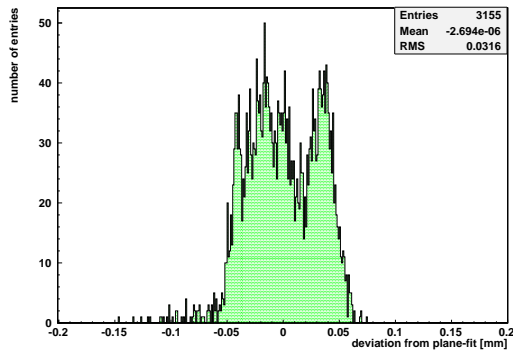
Figure 6.14: Histograms filled with the deviation of the side glued in step one from a fitted plane



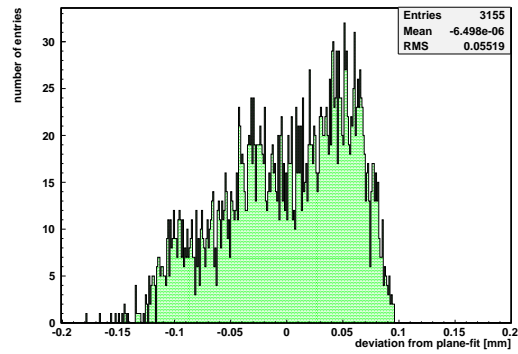
(a) Sandwich 0: Deviation from plane



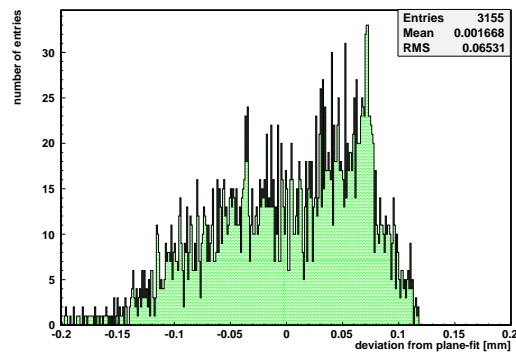
(b) Sandwich 1: Deviation from plane



(c) Sandwich 2: Deviation from plane



(d) Sandwich 3: Deviation from plane



(e) Sandwich 4: Deviation from plane

Figure 6.15: Histograms filled with the deviation of the side glued in step two from a fitted plane

7 Development of the Stiffback

To build large area micromegas detectors, very flat sandwich structures are needed. Since they have an area of a few square meters this is not a trivial task. The procedure is shown in chapter 5. An essential part in the technology to build these sandwiches is the so called "stiffback". This is a rigid and very flat plate, which has to be a bit bigger than the sandwich structures which are attached to it. It is used as an auxiliary structure in the glueing process to ensure the parallelism and flatness of the sandwich panel.

In this chapter the development of the stiffback from the first prototype to the present version will be presented.

7.1 First Stiffback Version

The first stiffback has been built as a sandwich structure. This design has been chosen because of the special features of this technology. The stiffback should be very rigid and as light as possible. This means that this structure should only undergo minimal sagging under its own weight and under the load of a sandwich panel. The weight has to be considered, since the stiffback should be easy to handle with one or two people without the use of a crane.

The sandwich layout of the stiffback is shown in figure 7.1.

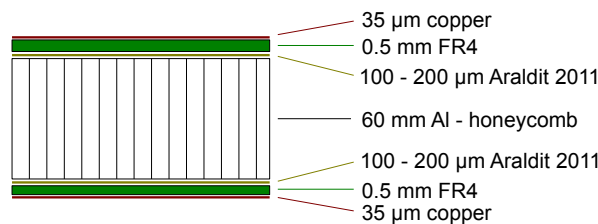


Figure 7.1: Cross section of the first stiffback sandwich

The actual stiffback does have additional thin aluminium plates on the side areas, which have only a small contribution to the stiffness of the overall panel.

In figure 7.2 the stiffback with the dimensions, 128.5 cm × 107.0 cm, can be seen from the side. It is simply supported by two sides. This means it does have a free rotational degree of freedom around the lines on which the stiffback rests. On top of the stiffback is a straight edge. It is placed in the middle of the panel. There is a light gap below the straight edge and the stiffback visible, which comes from a neon tube, resting behind. A measurement with a feeler gauge indicates this gap to be

between 50 and 100 μm . The stiffback, that was used to glue the sandwiches of the first prototype, was only supported on four steel balls. Simulations show, that the additional weight of the sandwich panel will increase the total deformation beyond the 100 μm limit.



Figure 7.2: Bending of the stiffback under its own weight. The airgap is visible by the shining through light.

A more exact surface scan of the stiffback has been performed in Freiburg at the CMM. The upper side of the stiffback with the vacuum connection is supported on four 4 cm broad beams, located on all four borders of the panel. The "good" side, onto which the sandwich panels were sucked during the glueing process, is scanned. The scan has only been performed on the trapezoidal area, where the FR4 sheets were mounted. The result of the measurement can be seen in figure 7.3. It shows the deformation of the surface of the stiffback under its own weight. From maximum to minimum it covers the range of almost 180 μm . This deformation is in agreement with the bending of the panels in figure 6.12.

Panel deformation experiments with additional weights have been performed. In figure 7.4 a beam bending experiment is visible. This means the panel is treated as a beam with a length of 110 cm and a width of 107 cm. It is supported on two sides simply. In the middle an additional aluminium profile is used to equally distribute the load along the whole width of the panel. Standard 0.5 litre lead bricks are used as weights. The mass of one brick is about 5.67 kg. With the help of the straight edge and the feeler gauge, the deformation for different numbers of lead bricks are measured. The results are summarized in a plot shown in figure 7.5 where not only an offset of $75 \pm 31 \mu\text{m}$ is shown, because of the own weight of the stiffback and the load of the additional aluminium beam, but also the linear increase of the deformation by weight, which is suggested by beam theory. One lead brick deforms the plate about $50 \pm 6 \mu\text{m}$. The $\pm 25 \mu\text{m}$ error in each deflection measurement point are chosen for the following reason. The smallest available thickness of the feeler gauge is 50 μm . The next larger thicknesses are usable in 50 μm steps. When a 50 μm feeler gauge can be inserted in the gap between the straight edge and the surface to be measured, and the 100 μm thick feeler gauge can not, the gap is between these two thickness values. In this case the measured value would be $75 \pm 25 \mu\text{m}$.

To check the viability for future stiffback simulations, this experiment is now simulated in ANSYS. As element type SHELL181 is used. This type can be used to

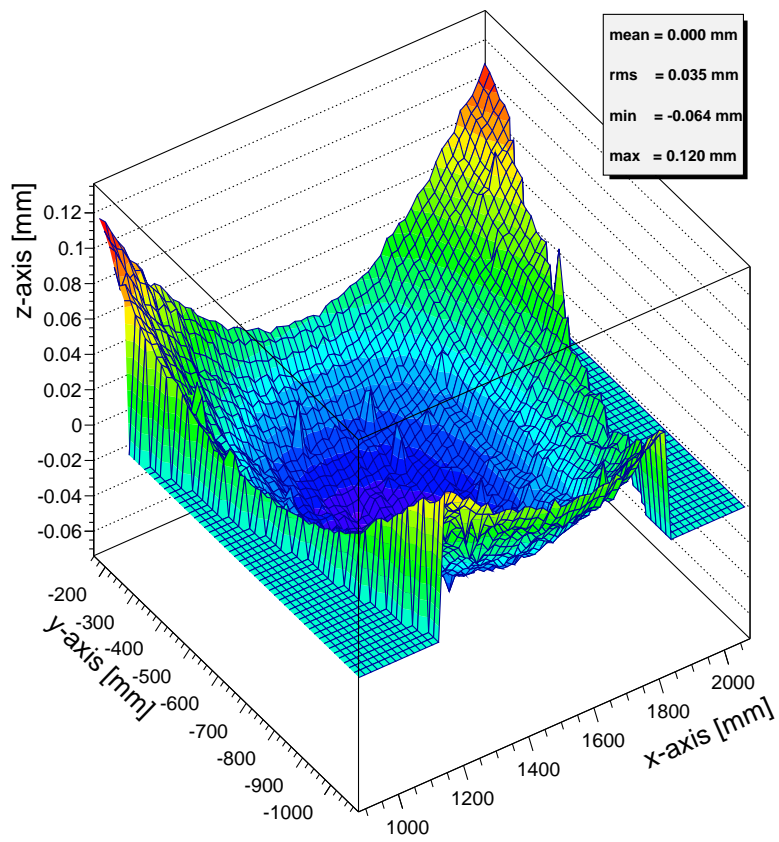


Figure 7.3: Stiffback deformation under its own weight



Figure 7.4: Setup for the beam bending experiments of the stiffback

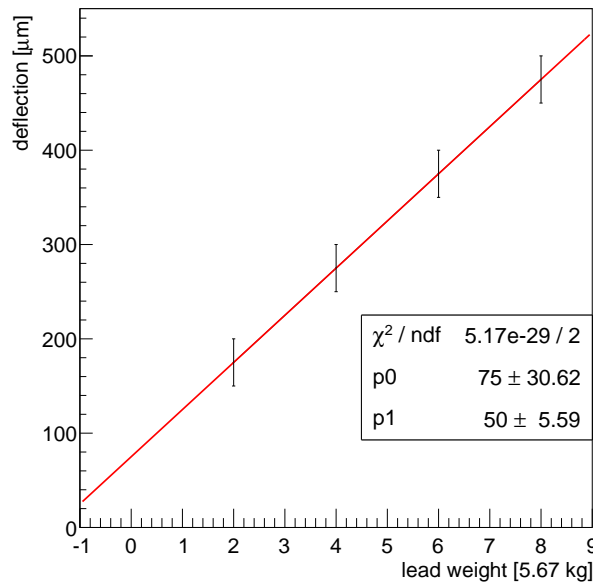


Figure 7.5: Beam bending like deformation experiment of the stiffback. The stiffback is two times simply supported. The 0.3 mm deformation of the sandwiches in figure 6.12 correspond to a load of the stiffback of about 30 kg.

simulate thin plates. Additionally different section layers of the plate can be defined. It is done according to figure 7.1. For the glue a layer thickness of 150 μm is used. In the simulation the plate area is enclosed by four lines. To establish a bending scenario simulation with a plate, the boundary conditions for the two opposing lines, which should function as simple support, have their translational degrees of freedom in x,y and z direction restricted to zero. The rotational degrees of freedom may not be restricted because the plate is not fixed along the lines. To simulate the equally distributed load coming from the 5 cm broad aluminium profile, all nodes in this area are loaded with a force in z direction. The sum of all these forces is the weight of two lead bricks (=111.25 N).

The simulation (figure 7.6) suggests a maximum deformation in z-direction of about 111 μm under a load of two lead bricks, in agreement with the actual measurement, which results in a deformation of $100 \pm 11 \mu\text{m}$ for the same weight. A deformation of 300 μm , as observed at the panels of the mechanical prototype, corresponds to a load of about 34 kg in the beam bending experiment here.

To test if the deformation of plates can be simulated as well as the deformation of beams, the same experiment has been repeated with all four sides simply supported. The setup is shown in figure 7.7. The dimensions of the investigated area are 110.0 cm x 89.5 cm. It is loaded in the middle with the same amount of bricks as before. With the help of the straight edge and feeler gauge the results in figure 7.8 can be obtained. For small deformations the load and the resulting deformation are linear proportional to each other, therefore a linear fit is used on the measurement values. The fit parameters indicate the offset and the inclination of the line. The offset with this kind of boundary conditions is about $51 \pm 19 \mu\text{m}$. The deformation for each block of lead is $37 \pm 4 \mu\text{m}$, which is considerably smaller than in the case of two simple supports.

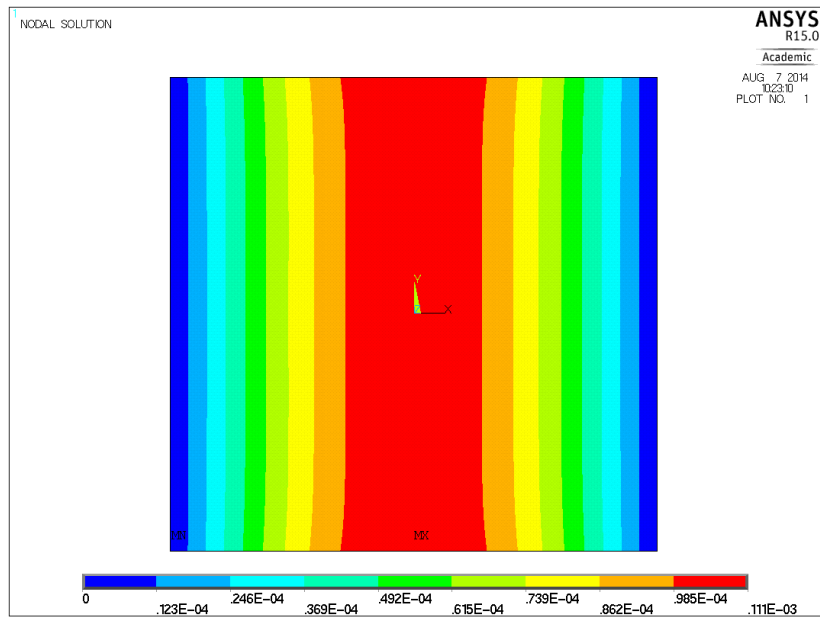


Figure 7.6: ANSYS simulation of the bending of the stiffback, which is supported on two sides and loaded in the line in the middle with a force equal to the weight of two lead bricks



Figure 7.7: Experimental setup for measuring the stiffback deformation

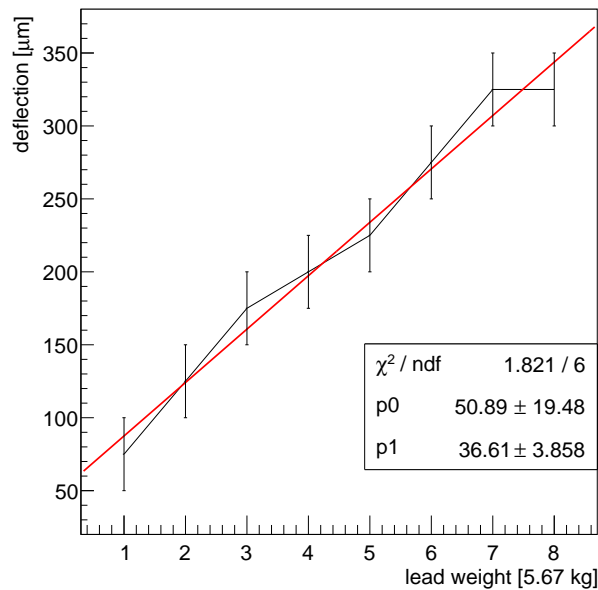


Figure 7.8: Deformation experiment with stiffback supported on four sides. The red line is a fit to the data. The deformation of $36.61 \mu\text{m}$ per lead brick agrees well with the ANSYS simulation.

This experiment is simulated in ANSYS as well. The element type and section layers remain the same as in the simulation before. To simulate the weight in the middle, a force is put on the lines of the area where the lead is supposed to rest. The total sum of the force on the lines equals the weight of the lead brick.

The result is visible in figure 7.9 and suggests a deformation of $35.5 \mu\text{m}$ in the middle and about $35.0 \mu\text{m}$ at the lines where the brick touches the panel. The good agreement with the measurement demonstrates the influence of the boundary conditions on the stability of the panel.

It must be considered furthermore that during glueing the stiffback is only supported on several steel balls, unlike the experiments here, where the panel is supported on whole sides. A plate supported on only the four corners for example will deform considerably more than a plate supported on all four sides, or a plate supported by 2 steel balls per side.

7.2 Double Honeycomb Concept

After the results of the last section, it is clear that the current layout of the stiffback has to be revised. The new concept makes again use of sandwich technology. It consists of nine layers instead of seven and does include additional aluminium profiles to reinforce the stiffness of the panel. Aluminium is furthermore used as facing sheet material instead of FR4. The structural design can be seen in figure 7.10. The in total four layers of glue, which are between each of the layers, are missing in this figure.

To test the design it is simulated in ANSYS. For the thin layers of aluminium, glue and honeycomb SHELL181 is used as element type. Different section layers are

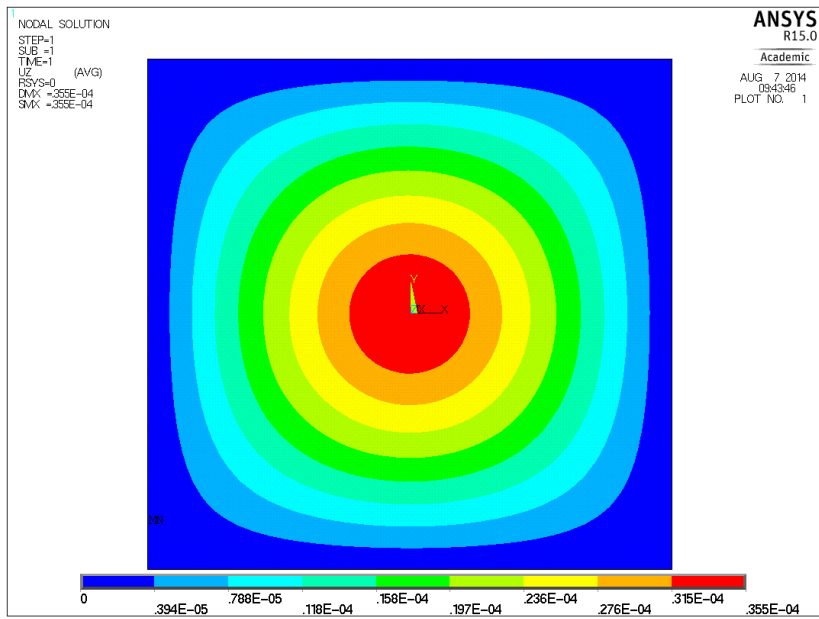


Figure 7.9: ANSYS simulation of the bending of a stiffback supported on all four sides

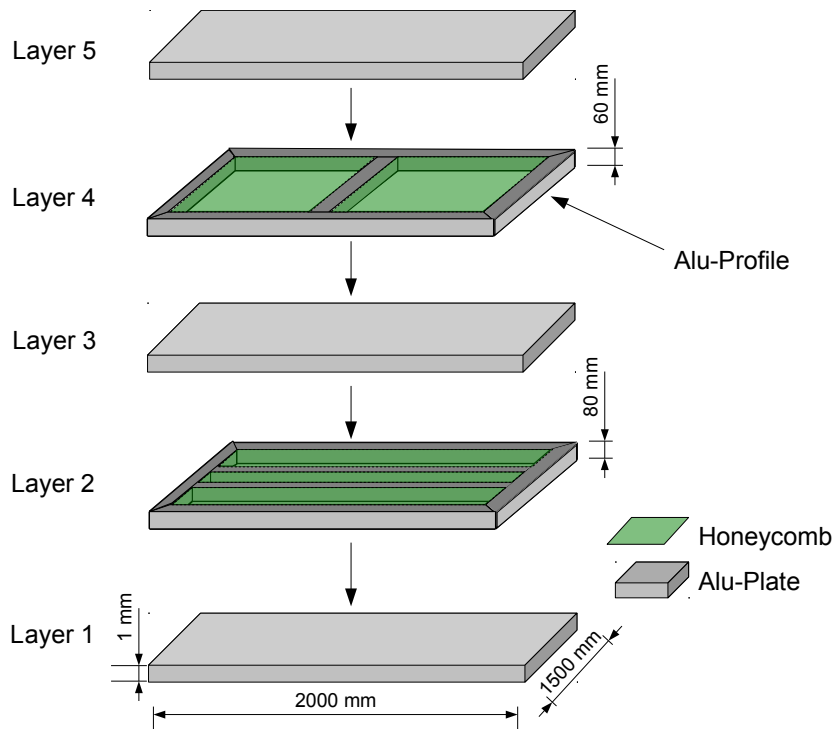


Figure 7.10: Structural design of a double honeycomb stiffback

defined for the materials to simulate the sandwich structure. BEAM189 is used as element type for the rectangle hollow aluminium profiles. For each of them a corresponding cross section is defined to take into account different wall thicknesses and geometries. In the simulation gravity is included and the trapezoidal pressure on the stiffback, coming from a sandwich panel with the dimensions and weight of the actual SM2 modul. An 11 mm thick sandwich panel does have a specific weight of 2.88 kg m^{-2} without aluminium beams at the borders. Honeycomb with 9 mm cellsize and $200 \text{ }\mu\text{m}$ thick glue layers are taken for the calculations here. To take into account the weight of the beams of the panel, a 30 mm x 10 mm hollow rectangle aluminium profile with 1.5 mm wall thickness is used for the calculation. The sum of all exterior and interior beams is about 9 m. When all this is included the total weight is about 5.6 kg m^{-2} . This means the pressure on the trapezoidal region is about 55 N m^{-2} . The stiffback is supported on four points which are 4 cm away from the corners. Figure 7.11 shows a result of the simulations. In this example 2 mm wall thickness is used for the reinforcing aluminium beams of the stiffback. When supported at the four corners the maximum deformation is $64 \text{ }\mu\text{m}$ in this case. This value is below $100 \text{ }\mu\text{m}$, the rigidity therefore is sufficient.

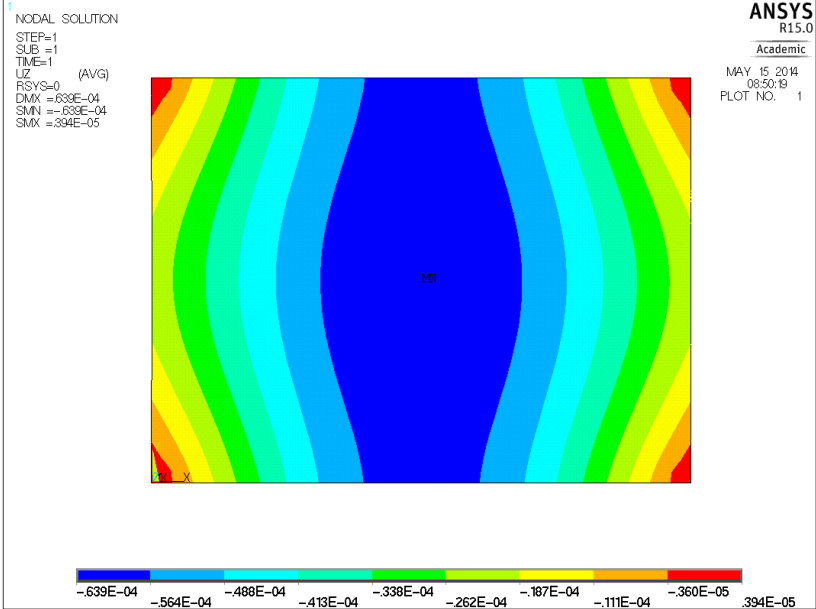


Figure 7.11: ANSYS simulation of a double honeycomb stiffback showing a maximum deformation of $64 \text{ }\mu\text{m}$ when supported at the corners only and loaded with a trapezoidal pressure representing the load of a sandwich panel attached to it during the construction process

The goal of the simulation is to minimize the deformation of the stiffback under load. Different beam setups in the stiffback sandwich and loadings are therefore simulated. Table 7.1 gives the results of various simulations. In the first case of the simulation the double honeycomb sandwich without reinforcing beams is loaded in different ways. Despite all deformation results of the different beam setups being very close, this setup is the least rigid one. The next setup of the beams is as introduced in figure 7.10. All beams are included with 2 mm wall thickness in this case, and with 4 mm in the next one. The results of these two cases are almost identical. But they both are better than the first case with no beams at all. For the last two simulations the inner

beams are removed. Only the outer beams remain. Because of the reduced weight the sagging due to gravity is reduced.

Deformation [μm]	gravity	gravity + pressure	pressure
No beams in Sandwich	57	71	14
Beams with 2 mm wall thickness	54	64	10
Beams with 4 mm wall thickness	55	63	8
2 mm beams on borders only	51	61	10
4 mm beams on borders only	49	58	9

Table 7.1: Results of deformation simulations in ANSYS

The beams in the middle do not contribute much to the stiffness according to these simulations.

In addition to the rigidity, the total mass of the construction can be used as decisive factor, see table 7.2.

	mass [kg]
No beams in Sandwich	57.36
Beams with 2 mm wall thickness	75.20
Beams with 4 mm wall thickness	95.21
2 mm beams on borders only	70.02
4 mm beams on borders only	84.09

Table 7.2: Mass of stiffback with different beam setups

From table 7.1 it is shown that there is not much difference between 2 mm or 4 mm wall thickness for the problem at hand. Furthermore the beams located only on the borders are a more suitable solution. Table 7.2 shows a mass difference of about 14 kg for the last case when comparing 2 mm and 4 mm wall thicknesses. A lighter stiffback is more favourable because it is easier to handle.

The double honeycomb design works best with 2 mm wall thickness beams which are only at the border of the stiffback. At a weight of about 70 kg it has a maximum deformation of 61 μm under load with only four point like supports.

A problem besides the weight would be the increased difficulty in the production process. While the glueing process would almost stay the same, the precision of the whole panel will decrease. That is because the errors in parallelism or deformation of each glueing layer will add up. More layers mean more possible errors. The additionally used beams in this design can make problems for a plane surface at the transitions where the honeycomb meets the beams. That is because it is difficult to achieve the identical thickness of the glue layer between the aluminium plate and the beams and between the aluminium plate and the honeycomb. A change in the thickness of the total glue layer by 50 μm will only influence the stiffness of the overall panel marginally. According to ANSYS simulations for this design it results in a change of deformation of about 2 %.

7.3 Final Design

The weight of the double honeycomb design is about 70 kg. Since it is desirable to be able to handle the stiffback without crane, the weight is relatively high. Figure 7.12 depicts the layered structure of the final stiffback design.

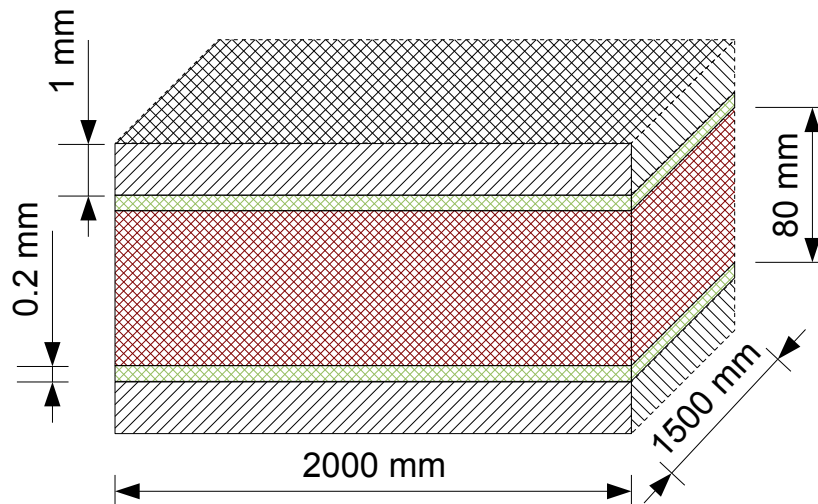


Figure 7.12: Final stiffback design

This design is a mixture of the first and second attempt. It only has one honeycomb layer instead of two. It furthermore uses aluminium plates with 1 mm thickness instead of 0.5 mm thick FR4 layers with an additional 35 μm copper layer. Between the aluminium plate and the honeycomb the glue layer is shown. Estimations of the bending stiffness result in a 9.1 times higher bending stiffness for the new design in comparison to the first stiffback design. This calculation for the bending stiffness D follows chapter 4.3.

The mass of this setup is 41.64 kg, which is a viable value.

To check if the construction still has the necessary stiffness, ANSYS simulations have been performed. In the first test the sandwich is supported by four point-like supports which are 2 cm in x and y direction from the corners away. The loading of the panel includes its own weight with gravity and a trapezoidal pressure of 55 N m^{-2} representing a complete sandwich panel of the SM2 modul pressing down on the stiffback because of gravity. The result can be seen in figure 7.13.

With this setup a maximum deformation of 171 μm , beyond the limit is existent in the middle of the plate. The only way to reduce deformation without an increase in the weight of the stiffback is to change the way the plate is supported. Therefore the number of point-like supports is increased from four to eight. In the middle between each of the old supports there is an additional new one. The result according to this design is shown in figure 7.14. With a maximum deformation of only 32 μm it is a very promising setup. It is compared to the double honeycomb design lighter, stiffer and less susceptible to errors since it does not contain any reinforcing beams and has only five overall layers instead of nine. If a stiffback of this size is made out of full aluminium it would have to be at least 7 cm thick to have the same

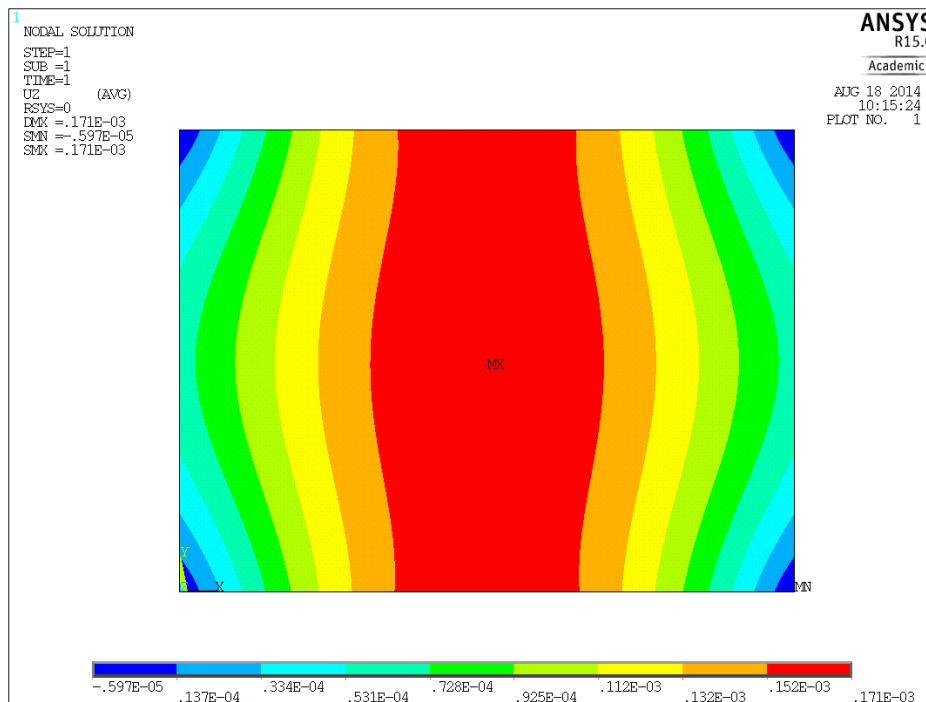


Figure 7.13: ANSYS simulation of the final stiffback design supported on four corners

deformation under the same parameters as the sandwich stiffback design here. It has been simulated in ANSYS. The weight of the plate would be 567 kg. This shows the superior nature of the stiffback sandwich in comparison to a full aluminum plate.

7.4 Small Scale Prototype for New Design

The simulations have shown the viability of the new design. But before building the actual stiffback a small prototype has been built to prove the concept. It is a 50 cm × 83 cm large sandwich with the same layers as described in section 7.3.

The building of this panel has not been performed as described in chapter 5. The sandwich panels of the New Small Wheel modules need a planar surface on both sides. A stiffback is therefore needed as second planar reference surface next to the granite table. Since the building of the stiffback is the task of this chapter, no other stiffback could be used as auxiliary structure. But the fact, that only one side of the stiffback needs to be as planar a possible, opens up an alternative way of construction, using a vacuum hood.

One aluminium plate is laid down on the granite table. Then the plate is roughened up with abrasive paper and subsequently cleaned with isopropyl alcohol. Afterwards the two component epoxy glue Araldite 2011 is applied on the aluminium plate. Such an amount of glue is chosen that after distribution the thickness of it is about 300 µm. A dented spatula is then used to make 300 µm large grooves in the Araldite layer, to help the honeycomb form a better connection with the adhesive. Afterwards the aluminium honeycomb can be laid down. The borders of the honeycomb area

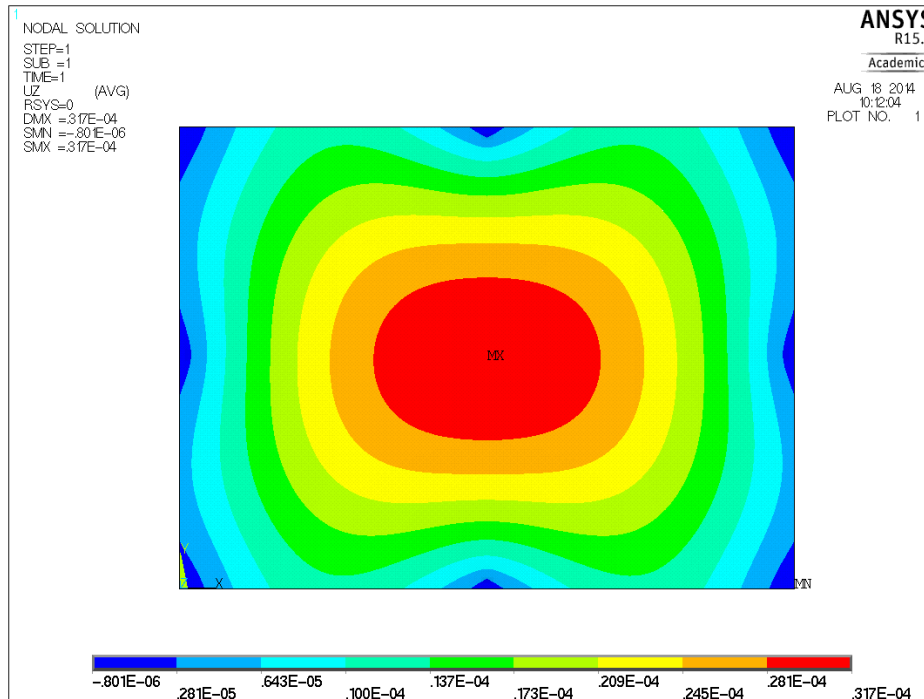


Figure 7.14: ANSYS simulation of the final stiffback design (2×1.5 m) supported on eight points. The maximum deviation under gravitational load and a trapezoidal pressure of 55 N m^{-2} , representing the weight of a sandwich panel of the SM2 module, is $32 \mu\text{m}$. The weight of a sandwich panel of the SM2 module is about 11 kg.

is about 1 cm inside of the border of the aluminium facing sheets. To press the aluminium plate to the granite table during curing of the glue, a simple wood plate, which could be replaced by a metal plate, has been put on top of the honeycomb. To ensure an equal and large pressure on the wood plate an auxiliary frame with a plastic foil has been put across the plate, and sealed on top of the aluminium frame. The setup can be seen in figure 7.15.

The air is sucked out of the volume, which is enclosed by an air tight frame, leading to a pressuring down of the plastic foil on the stiffback components. After a night of curing, the second aluminium plate can be prepared for glueing. The procedure is the same as for the first aluminium plate. After the preparation steps the honeycomb with the first aluminium plate glued onto it is laid down onto the second one. To put enough pressure on the stiffback for curing and for transferring the planarity of the granite table to the stiffback surface of the side glued in the second step, the frame with the plastic foil is used again. The frame is evacuated until a pressure below 100 mbar is reached. After a day of curing the four side areas of the stiffback are sealed with a 1 mm thin aluminium plate, which is glued to both facing sheets of the sandwich. Vacuum ports are added on two opposing sides as well. The space enclosed by the plate of the side area and the two aluminium facing sheets is filled with transparent two component epoxy resin. The resulting stiffback can be seen in figure 7.16. It shows the stiffback prototype during a surface scan using a CMM in Freiburg.

The sealing of the stiffback is needed to create a vacuum inside of the stiffback. The



Figure 7.15: Evacuated frame with plastic foil to equalise the pressure on the stiffback during curing



Figure 7.16: A 50 cm × 83 cm stiffback in final design layout during a surface scan using a CMM

honeycomb is microperforated with lots of small holes, making the vacuum be able to distribute throughout the whole stiffback. With many small holes in the aluminium plate of the stiffback the FR4 panel can be sucked onto it without the help of the extra mesh as it is described in chapter 5. If the pressure is 0 bar inside of the stiffback only 98 holes with 1.5 mm diameter would be needed to overcome the weight of a 1 m² area of a 0.5 mm thick FR4 plate with 1 cm of honeycomb attached to it. This comes from equalising the weight of 1 m² of the sandwich component and the force induced on a area of 1 m² by 1 bar air pressure. It is possible to calculate the area needed for 1 bar air pressure to equalise the weight of the 1 m² sandwich component. This area can be divided up in holes with arbitrary diameter.

Different measurements of the stiffback with the CMM in Freiburg have been performed. The first one is a simple scan of the side glued in the second step. It is visible in figure 7.17. Only the borders of the surface beyond the active area show deformations larger than 50 µm.

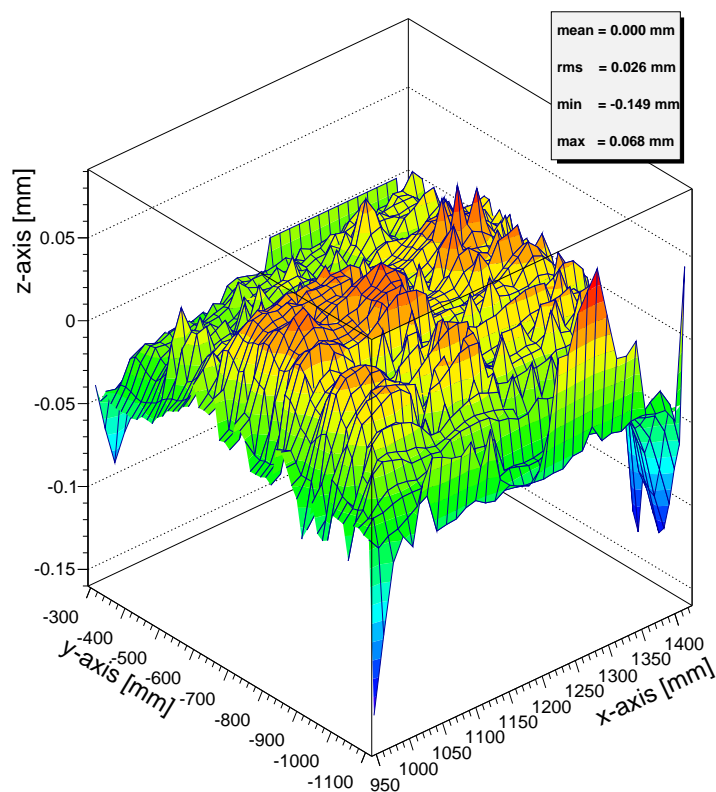


Figure 7.17: CMM measurement result of the surface glued in the second step; total deformation < 50 µm with exception of the border region

These deformations have a few origins. The first one comes from the very first time the air of the stiffback has been evacuated. It is the reason for a few permanent dents at the borders of the stiffback. Refilling of the air and repeated evacuation does not deform the stiffback anymore. This issue has been measured by scanning the surface of the stiffback with the CMM while it is evacuated and while not. Afterwards the difference of these two histograms has been calculated and plotted. The result can be seen in figure 7.18. There are two main aspects visible in the figure. One is a 10 µm deformation in the quadrant nearest to the spectator. The other distinctive feature are

the numerous 10 μm large spikes. They partly come from a stuttering of the engine of the CMM and partly from a suboptimal algorithm in the root macro used to create the histograms. It is therefore legitimate to assume an error of 10 μm . This leads to the conclusion that the evacuation of the stiffback does only deform it the first time.

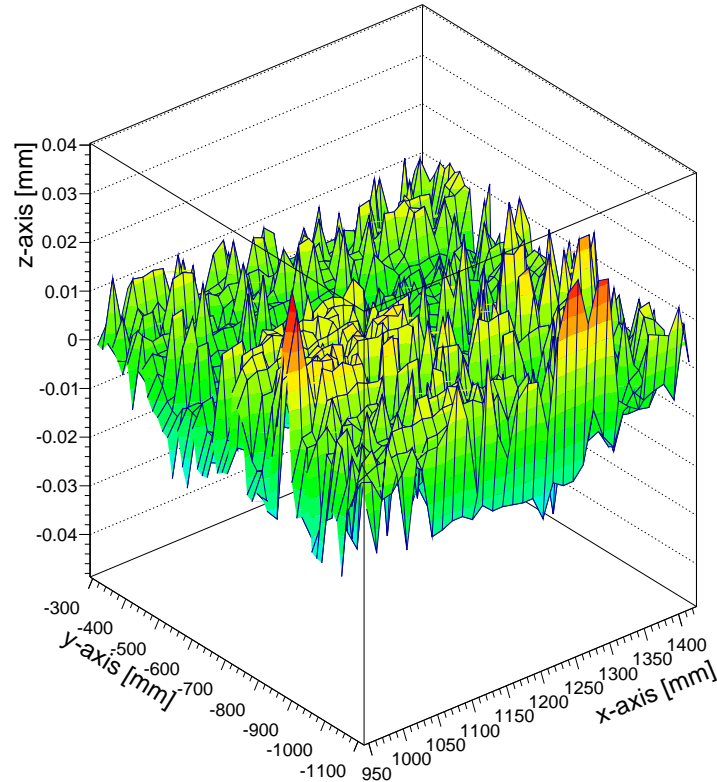
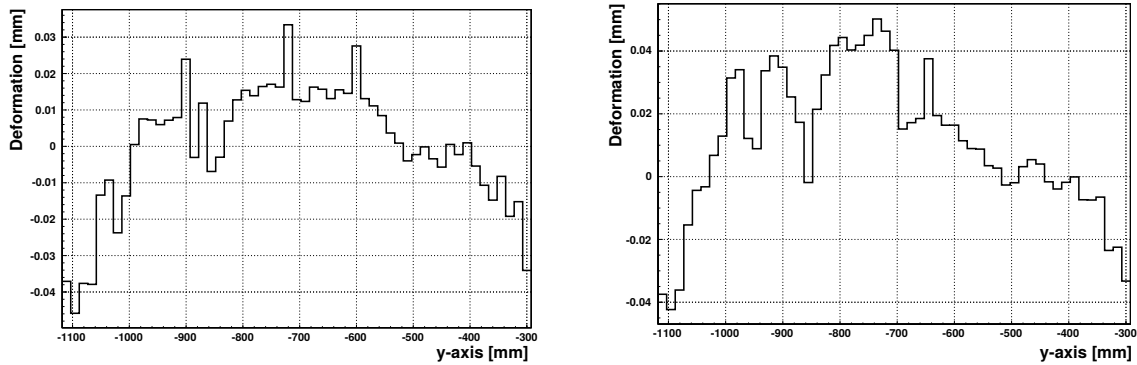


Figure 7.18: Difference of two CMM scans of the stiffback surface; one with the stiffback evacuated and the other not evacuated; there is no observable difference

Another reason for the deformation of the border of the stiffback, visible in figure 7.17 is the simple fact, that hardened epoxy resin residues are on some parts of the borders. They come from carelessness during application on the side areas. Most of them have been removed by a scraper. The resin residues and the successive removal of it has to be avoided for the actual stiffback to achieve a planarity below 50 μm . Another reason for the deformation of the border can come from the production process. When carrying the 1 mm thick aluminium plates by hand, it is possible to deform the borders more than 50 μm . For the plates of the actual stiffback the use of suction cup lifters should be considered.

Coming back to take a closer look at the overall deformation in figure 7.17, two bins in x-direction are chosen and their content is projected in y-direction. They represent the profile of the minimum (7.19(a)) and maximum (7.19(b)) deformation of the stiffback along y-direction. For the maximum deformation plot the bins at the two ends of the x-axis have been omitted.

The plots in 7.19 show two things. The first one is that because of the strong deformation at the borders, the first 5 cm of each border can not be used. The overall



(a) Projection of minimal deformation profile

(b) Projection of maximal deformation profile

Figure 7.19: Projection of deformation profile in y-direction

deformation in the minimal deformation example comprises 25 μm in the newly defined active area of the stiffback. The overall deformation in the maximal deformation example reaches 50 μm .

The second thing shown in the plots is the curvature of the total panel along y-direction. The 73 cm long active area forms an arch with maximum deformation of 25 μm in the middle, which can be seen in 7.19(a). This curvature can have several reasons. One is a possible deformation of the granite table used for glueing and another one is coming from possible deformations during the transportation of the stiffback. Additionally unequally applied glue may have an effect. But the most decisive influence probably comes from the honeycomb. It does have a little curvature. Because of a thickness of 80 mm with 6 mm cell size and 76 μm thick aluminium walls, the used honeycomb is compared to other honeycombs very rigid. A lot of force had to be used therefore to press the plates during glueing. After the glueing the honeycomb may have gone back a bit to its initial state, deforming the stiffback. The solution for this could be a honeycomb with thinner walls or 9 mm cell size.

Another test performed with the stiffback is a three point bending test. It is therefore placed on two 4 cm broad aluminium beams at each end of the long side of the panel. In the middle of the panel another aluminium profile with the same dimensions is placed in the middle on top of the setup so far. The setup can be seen in figure 7.21. For the bending experiment the weights 6.285 kg, 12.595 kg and 22.684 kg are used. To get convincing deformation values, ten positions of the middle beam have been measured with the CMM machine. The first measurement is without weight for reference. The next are with the different weights. The difference between the reference measurement and the data sets after weight application is plotted and fitted with a straight line. The height of the lines is the deformation induced by the different weights. This is shown in figure 7.20. The results are summarized in table 7.3.

Additionally to the measurement results, ANSYS simulations have been performed. These describe the same bending experiment. The results of the simulations are about 30 % smaller than the measurement and summarized in 7.3. For these ANSYS simulations it is safe to assume an error of at least 10 %. The CMM does have a measurement error of about 10 μm . These spikes in previous surface scans or in

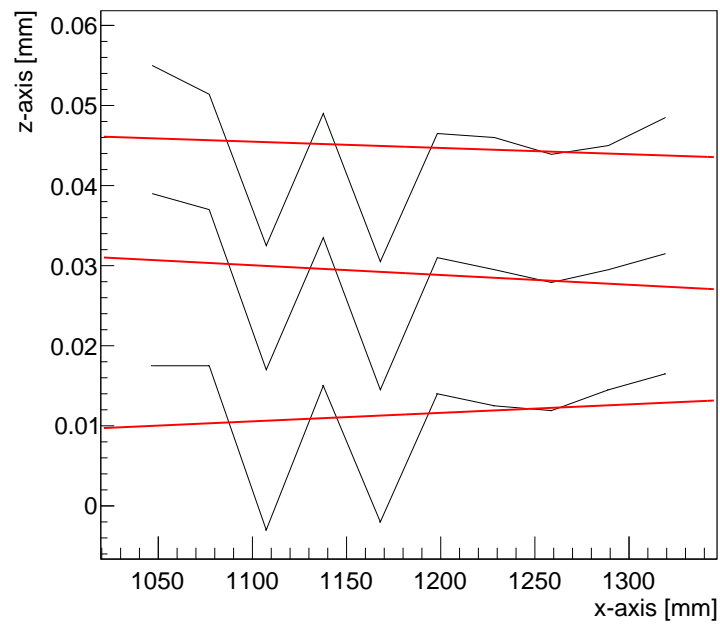


Figure 7.20: Difference of CMM data from a reference line of the unloaded three point bending scenario measurement of the prototype and the cases with the beam in the middle loaded with 6.3 kg, 12.6 kg and 22.7 kg; the red line is a linear fit for each case

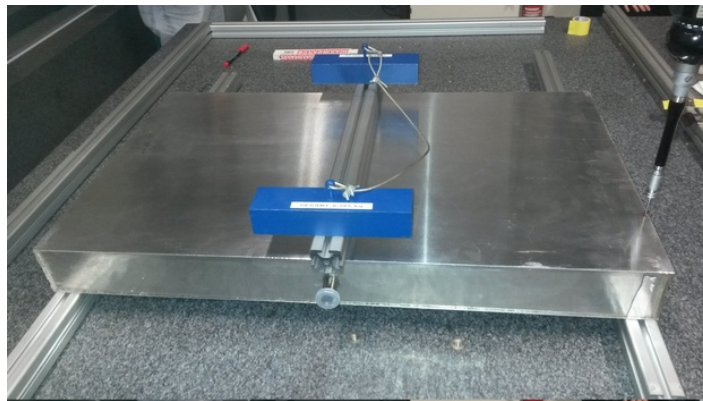


Figure 7.21: Photo of setup of three point bending test of small stiffback prototype

weight [kg]	deformation [μm]	ANSYS simulation [μm]
6.285	12	9
12.595	28	18
22.684	44	32

Table 7.3: Deformation results of three point bending test

figure 7.20 in the order of 10 to 20 μm can mostly be traced back to the CMM. An alternative reason for the spike could be dust particles. Because of this measurement error and the fact, that the effect of the aluminium profil, which is only loaded at the outer ends and additionally deforms under load, is completely neglected, the simulations and the measurement are in agreement. In the worst case scenario, when this difference is not based only on errors, and the faktor 1.4, which translates the simulation to the measurement values, is multiplied with the maximum deformation of 32 μm of the eight times supported stiffback of the final design, which is shown in figure 7.14, the resulting value is still below 50 μm .

The deformation under its own weight has been tested as well. The plate was put on four balls in each corner and the surface has been scanned. To get the deformation under its own weight, the difference between the result of this measurement and the result from the scan of the plate laid directly on the granite table is so small, that it is below the resolution of the CMM. The deformation of this stiffback under its own weight, when it is supported by its four corners, is therefore below 10 μm .

It is shown, that in principle this proposed design does already fulfill all requirements when defining an active area. The only improvements that could be made to possibly reduce the deformations in the border region, is to implement aluminium profiles at the borders. But this would increase the weight again.

8 Interconnections

This chapter addresses the deformation of the SM2 sandwich panels in the quadruplet through gas overpressure. The micromegas detector is usually operated with a few mbar overpressure and with a continuous flow of the Ar/CO₂ gas mixture through the detector. This inevitably leads to a force equivalent to $200 \text{ N/m}^2 \cdot 2 \text{ m}^2 = 400 \text{ N}$ and an inflation of the sandwich panels of the Micromegas detector of the NSW of about 2.2 mm for 2 mbar overpressure. Since the goal is to keep the maximum deviation of the outer sandwich panels below 100 μm , to get locally flat positions for the optical alignment platforms, it is mandatory to introduce a method to reduce the maximum deformation. So called interconnections are therefore introduced. These are cylindrical objects, which connect all 5 sandwich panels of a quadruplet and keep each panel in its position. They are positioned in the active area of the sandwich trapezoid. To find the position and number of interconnections needed is the main goal of this chapter. Whether and where additional beams are needed to support the structure is addressed as well.

A readout panel with nine interconnections and with the dimensions shown in 8.1 was suggested by colleagues. The letters A,B,C and D represent additional aluminium bars, which reinforce the sandwich panel. Beam A and C are in the middle of the trapezoid. The lines B and D are placed in the middle between line C and the two vertical borders of the trapezoid. The sandwich panel is simulated in ANSYS with a SHELL281 element type, whereas for the beams element type BEAM189 is used. The sandwich consists of five layers. Two 0.5 mm thick FR4 facing sheets and a 10 mm thick aluminium honeycomb core with 9 mm cell size. The facing sheets and the core are connected with a 100 μm thick layer of glue. The beams have a rectangular cross section with a width of 3 cm and height of 1 cm.

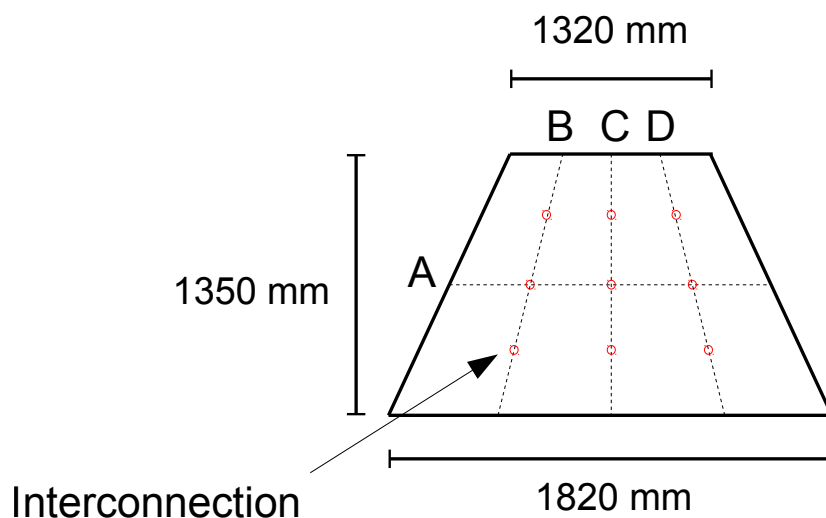


Figure 8.1: Sketch of the setup for interconnection simulation

The simulations treat five different cases. The first one addresses the sandwichpanel with no additional beams, but with interconnections. The second case includes hollow beams at position A and C, with 1.5 mm wall thickness. In case three the position of the beams is the same, but the beams are made out of full aluminium and are not hollow anymore. In case four and five beams are implemented at position A,B,C and D, whereas in the first mentioned one the hollow beams are used and in the second one the full beams. The maximum deformation for a different number of interconnections under an equally distributed pressure load of 2 mbar across the whole panel is shown in table 8.1. It can be seen, that the maximum deformation with no beams and interconnections is about 2.2 mm. Since the limit is 100 μm , all cases with nine interconnections would suffice.

Number of interconnections	Max. deviation under 2 mbar				
	Case 1	Case 2	Case 3	Case 4	Case 5
0	2185 μm	1654 μm	1490 μm	1458 μm	1260 μm
1	464 μm	325 μm	295 μm	297 μm	257 μm
3	256 μm	198 μm	190 μm	156 μm	136 μm
5	186 μm	171 μm	169 μm	120 μm	103 μm
9	62 μm	46 μm	44 μm	39 μm	37 μm

Table 8.1: ANSYS simulation results for the maximum deformation of read-out panels under a pressure load of 2 mbar and with different numbers of interconnections

Each simulation results in a plot showing the deformations of the sandwich panel. One example is given in figure 8.2, which displays the simulation for case one with nine interconnections.

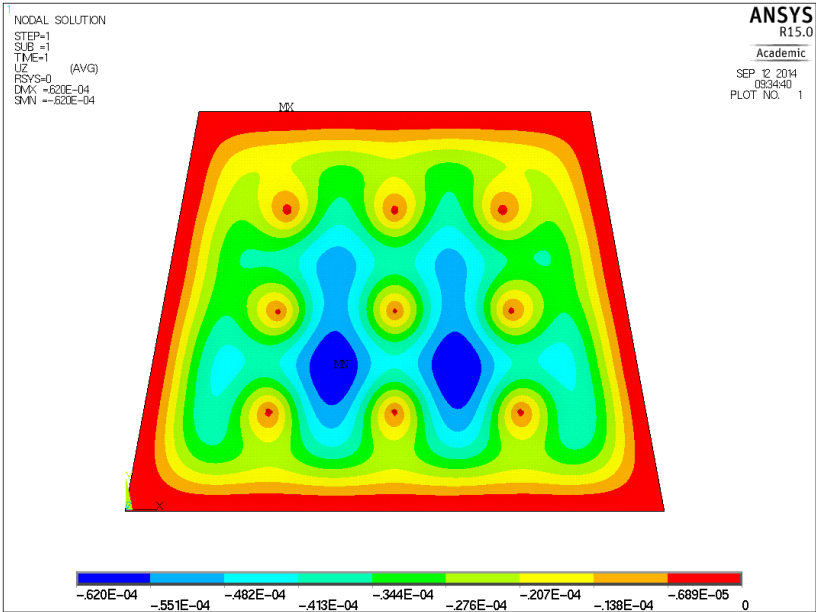


Figure 8.2: ANSYS simulation for case zero with nine interconnections leading to a maximum deformation of 62 μm

The goal regarding the maximum deformation would be reached, but another attempt is made to reduce the total number of interconnections and to keep the weight

as low as possible. Minimizing the number is making the panel production faster and reduces possible error sources. The full aluminium beam is weighting 0.81 kg m^{-1} . The hollow beam with a wall thickness of 1.5 mm has a weight of about 0.3 kg m^{-1} . If all four beams at position A,B,C and D are used, about 2.8 kg are saved per sandwich panel by the use of hollow beams. To reduce the number of interconnections, a different beam setup is investigated. It makes use of only two beams with three interconnections each. A sketch of it is displayed in figure 8.3. The two parallel beams are 457 mm away from the longest and shortest side of the trapezoidal panel.

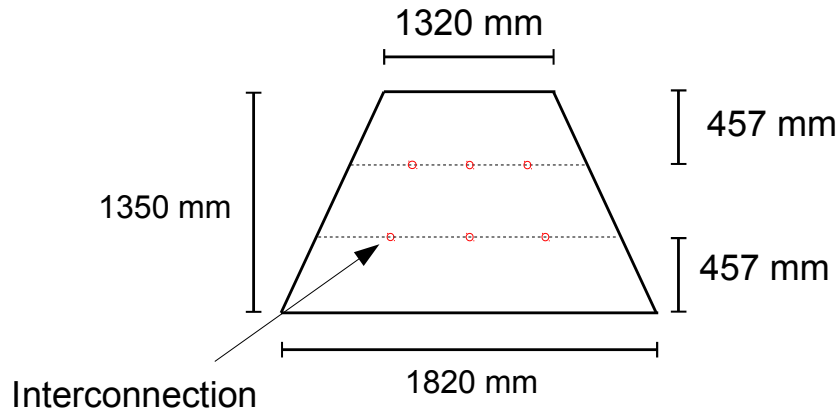


Figure 8.3: New setup with only six interconnections. The horizontal lines in the middle indicate the position of the aluminium beams.

ANSYS simulations have been performed to examine the new interconnection setup. All element types, material properties and sandwich layers remain the same. Solely the beam position and the interconnection position changes. The beams have a length of 1489.2 mm and 1650.8 mm. In the middle of each beam is one interconnection. The other two have a distance of 372.3 mm from the middle of the shorter beam and 412.7 mm from the middle of the longer one. The simulation examines different beam influences on the maximum deformation under a uniform pressure of 2 mbar and with zero or six interconnections. All beams have a width of 3 cm and a height of 1 cm. In the first case, no beams at all are used. The second case makes use of hollow rectangle aluminium beams with 1.5 mm wall thickness. Whereas in the last case full aluminium beams are used. The results of this simulation are summarized in table 8.2. The results for the two cases, where beams are used are very similar. Both cases achieve significantly less deformation than the case without reinforcing beam. Since weight saving is still an issue it is obvious to choose the hollow beam for this interconnection setup instead of the solid version.

Interconnections	no Alu beams	1.5 mm Alu beams	Full Alu beams
0	2182 μm	1813 μm	1675 μm
6	85 μm	57 μm	54 μm

Table 8.2: ANSYS six interconnection simulation for readout panels

To give an example of such a simulation result, the deformation of the sandwich panel is plotted. Figure 8.4 shows the case of six interconnections for the hollow aluminium beams.

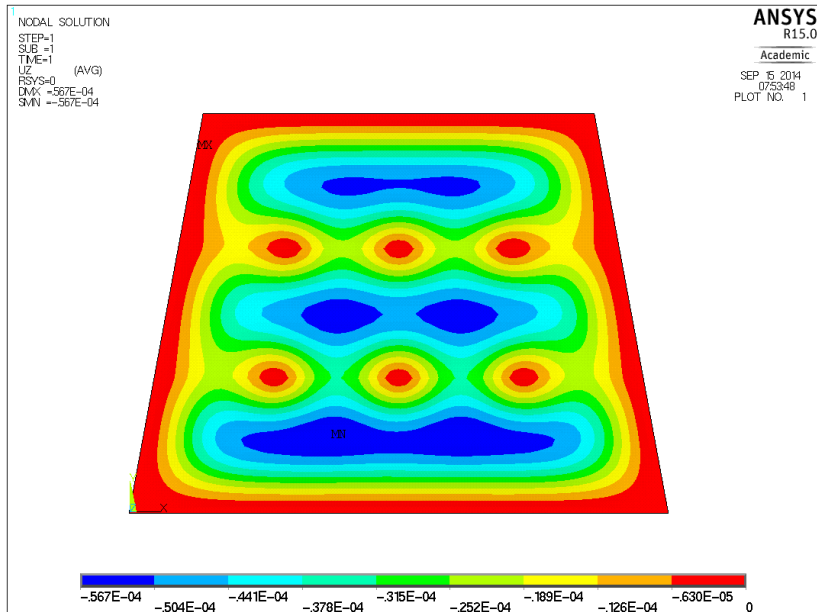


Figure 8.4: ANSYS result for 6 interconnection simulation with 1.5 mm wall thickness beams

Comparing the first setup with the crossed interconnection beams with the last setup with the parallel beams, the nine interconnection solution is having less maximum deformation. The deformation for the 1.5 mm wall thickness beams are $46\ \mu\text{m}$ and $39\ \mu\text{m}$ compared to $57\ \mu\text{m}$. Nevertheless the six interconnection solution is more favourable, since the deformation is well below the $100\ \mu\text{m}$ limit and six interconnections mean less work and time spent to build the panels. Furthermore possible error sources are reduced.

The simulations above have been performed for the readout panels. The drift panel is smaller, because it does not need the 6.5 cm broad strips holding the readout electronics. This means the drift panel does only have a basis length of 1689 mm instead of 1820 mm. The length at the opposite side of the panel is 1189 mm instead of 1320 mm. Repeating the simulations above for the drift panel, results in a maximum deformation of $53\ \mu\text{m}$. The distance between the middle and the outer interconnections are 300 mm and 350 mm on the shorter and the longer beam respectively

In the ATLAS collaboration there have been initially about ten interconnections in consideration for the SM2 module. Due to various simulations it has become possible to reduce the number of interconnections needed to six. This is the amount, which will be used in the final SM2 design by the collaboration.

9 Mesh

This chapter treats the steel mesh, which is an important part of every micromegas detector. It is used as an electrode between the cathode and the anode. It defines the end of the drift region and the beginning of the amplification region. As the name implies gas amplification takes place between mesh and anode because of the high E-field. Electrons will be sufficiently accelerated to produce new electron-ion pairs. The electrons move towards the anode, whereas the ions drift towards the mesh. The mesh is placed $128\ \mu\text{m}$ above the anode on pillars.

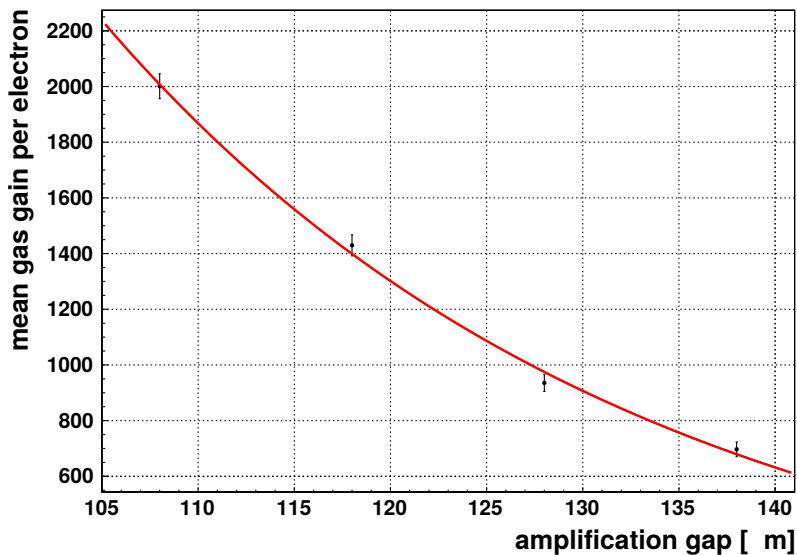


Figure 9.1: Garfield simulation describing the change in the gas gain with a change in the gap of the amplification region, taken from [Lösel, 2014], for an amplification voltage of 500 V

Deviations from this distance in the order of some micro meters quickly lead to different gas amplifications. The results of Garfield simulations, which show the mean gas gain per electron, which is produced in the drift region, depending on the amplification gap are plotted in figure 9.1. The amplification voltage is 500 V and the gas mixture used is Ar:CO₂ with a volumetric ratio of 93:7. The simulated values are fitted with an exponential function. The gas gain is about 950 at an amplification gap of $128\ \mu\text{m}$. If the gap is reduced by only $3\ \mu\text{m}$ the mean gas gain would increase by about 16%. To get a variation in the gas gain below 10% the variation in the amplification gap may not exceed $\pm (2 - 2.5)\ \mu\text{m}$.

To stop the sagging of the mesh it is stretched with a tension of about $10\ \text{N cm}^{-1}$ and glued onto the mesh frame. The first point of the discussion discusses how to stretch such a steel mesh homogeneously.

9.1 Mesh Stretching Process

The mesh stretching process is requiring a large table, pressurized air, a mesh frame and pneumatic clamps. Two different systems have been tested. The differences between the Sefar 3A system and the pneumatic clamp system from the Yuancheng Printing Equipment company are investigated in the following.

The handling of the steel mesh needs to be executed very carefully. It should only be transported when the mesh is already stretched or when it is rolled up. A kink or buckling will never disappear, even with stretching of the mesh, and makes it useless for the further use in the detector.

In the upcoming tests small meshes with a wire diameter of $23\ \mu\text{m}$ are stretched and glued on a $28 \times 28\ \text{cm}$ mesh frame, with a width of 2 cm. The first meshes have been stretched with the Sefar 3A system. A sketch of the setup is given in figure 9.2. The length of the clamps, which hold the mesh, is 25 cm. At the corners usually the distance between the end of the clamp and the end of the frame is 0.5 to 1 times the thickness of the frame the mesh will be glued to. The reason is to avoid extensive tension in the corners, where two perpendicular clamps are meeting.

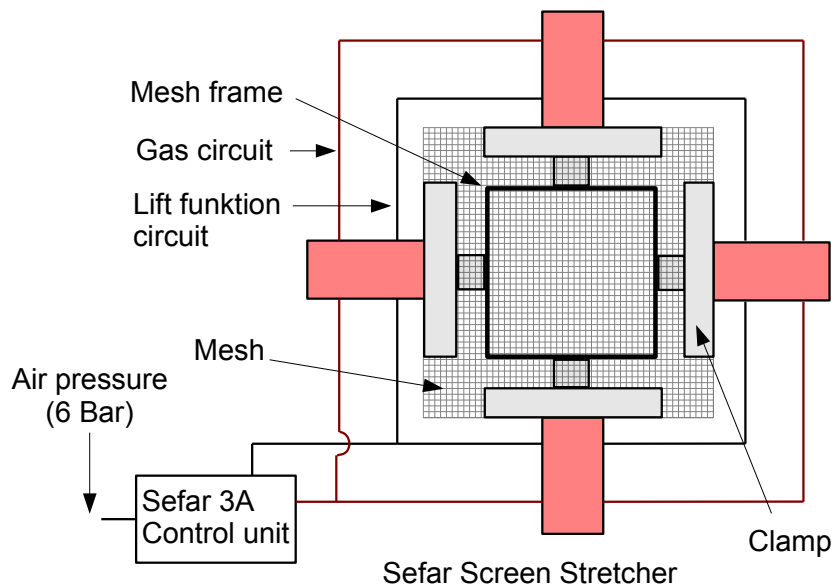


Figure 9.2: Mesh stretching setup for Sefar screen stretcher clamps. The clamps hold the mesh and stretch it with the use of air pressure.

After the system is set up on a table and all compressed air hoses are connected, the steel mesh is inserted carefully into the clamps. After fixation the air pressure is raised to about 2 bar, which leads to a mesh tension of about $10\ \text{N cm}^{-1}$. A picture of the real setup can be seen in figure 9.3. An advantage of the Sefar system is the so called lift function. This allows the mesh to be stretched while it is lifted up, meaning it does not touch the frame. When the desired tension is reached it can be lowered to the frame. Because of this there is no grinding of the mesh on the frame while stretching. If the frame should have any rough edges the mesh would otherwise rip apart. It

should be mentioned, that because of the lowering of the stretched mesh, the initial tension will increase by about 1 N cm^{-1} to 1.5 N cm^{-1} .



Figure 9.3: Photo of the Sefar mesh stretching setup

When the stretched mesh is attaching the frame, glue has to be applied. For this task the two component epoxy resin UHU Schnellfest with a processing time of 5 minutes has been used for the test meshes. It is important to distribute the glue equally on top of all areas where the mesh is touching the frame. This has been done with a small spatula, but it is possible to use a hard bristle brush as well. During curing of the glue it is recommended to put decent weights in the middle of the mesh. The reason is to increase the pressure of the mesh against the frame. A picture of the curing can be seen in figure 9.4. After half an hour of curing the pressure from the stretching devices can be released. Before opening the clamps to release the stretched mesh, the protruding mesh should be cut off.

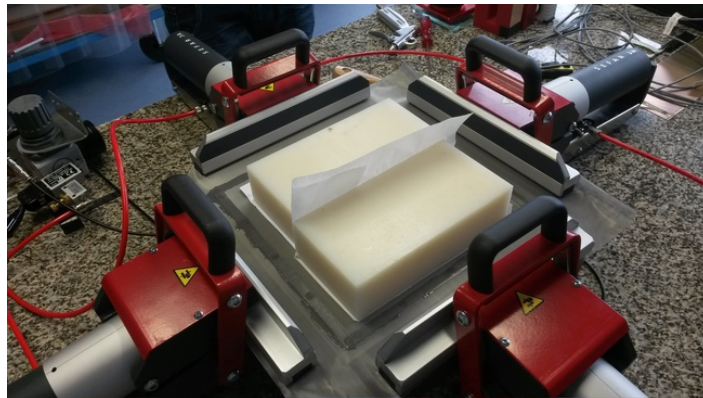


Figure 9.4: Photo of Sefar setup while curing of the glue, with additional weights on top of the mesh

The result is a stretched mesh on a frame as it can be seen in figure 9.5.

The second system tested here is from the chinese company Yuancheng Printing Equipment. In general the stretching process is the same, but there are a few differences. The first one is the different air pressure circuit, which is shown in figure 9.6. Additionally the size of the air cylinders is different. The clamps therefore need a pressure of about 4 bar to produce a mesh tension of about 10 N cm^{-1} . This means



Figure 9.5: Photo of a stretched mesh glued onto a $28 \times 28 \text{ cm}^2$ aluminium frame

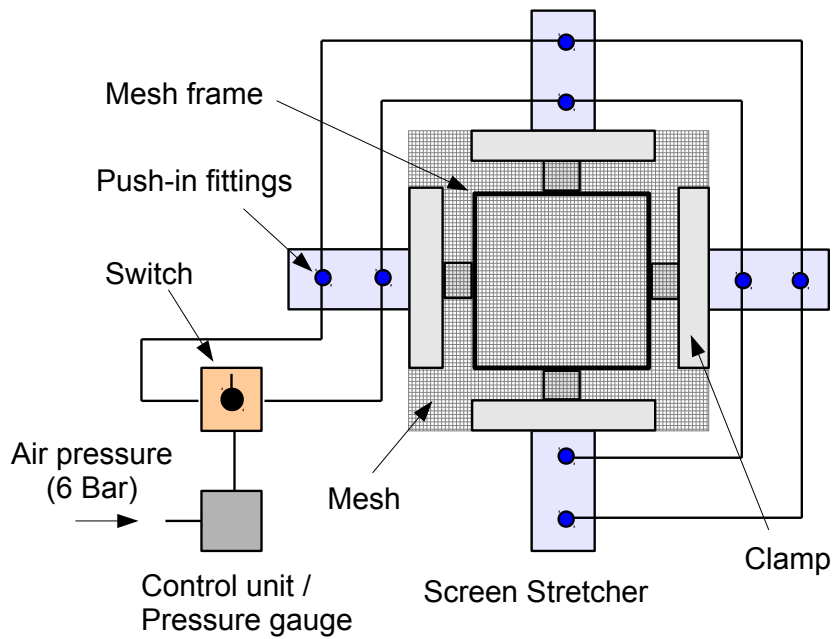


Figure 9.6: Mesh stretching setup for clamps from Yuancheng Printing Equipment

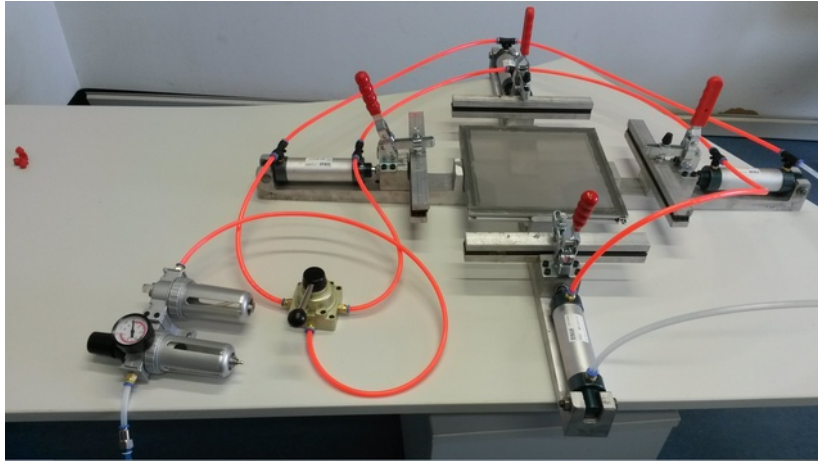


Figure 9.7: Photo of the mesh stretching setup using the clamps from Yuancheng Printing Equipment

that the clamps from the two different vendors can not be used in the same gas circuit. A photo of the real setup can be seen in figure 9.7.

The next difference is the lack of the lift function, meaning that the frame may not have any rough edges or protruding screws. The most striking difference is the manufactured quality, which becomes apparent in the simplicity of the design and the price. In figure 9.8 a photo of a stretching device is shown.

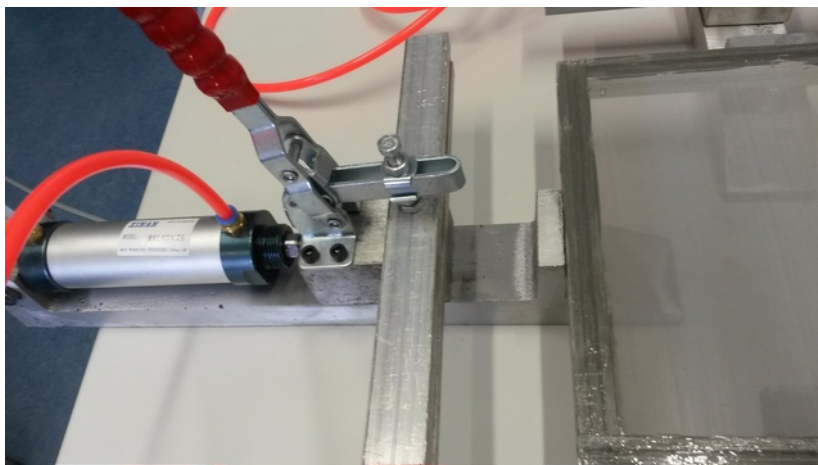


Figure 9.8: Photo of a clamp from Yuancheng Printing Equipment

With both the Sefar system and the one from the chinese vendor several small meshes (24 cm \times 24 cm) have been produced. The interesting question is now to investigate the quality of the stretched meshes, particularly the distribution of the tension of the meshes glued onto the frame. The Sefar tensocheck 100, a commercial tension meter, is used to get directional information about the tension of the meshes, see figure 9.12. Because of the size of the tension meter and the mesh, only nine measurement points in each direction are taken. The only problematic is when measuring the tension in regions very close to the frame. If the measurement is too close to the frame the tension will deviate from the tensions in the middle of the mesh. This effect happens

when not using the correct distance between the end of the clamps and the end of the frame at the corners.

Two measurement examples are chosen for comparison. They are displayed in figure 9.9 and figure 9.10. The different colors in these histograms are representing the different mesh tensions in units N cm^{-1} . The same mesh with a wire diameter of $23 \mu\text{m}$ has been used. The tension measurements have been performed with the Sefar Tensocheck 100, which is directional sensitive, meaning the tension in x- and y-direction can be read out separately.

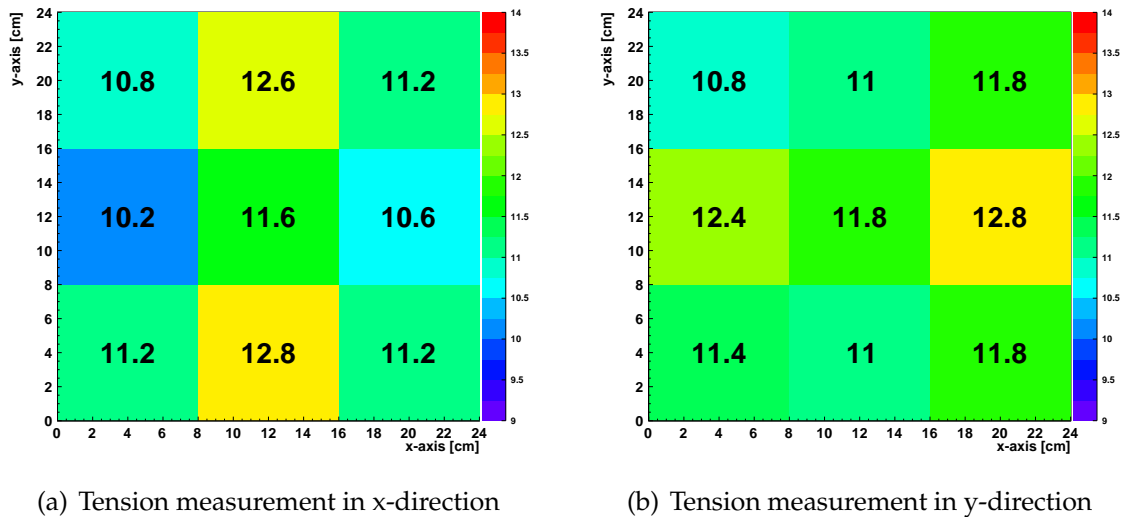
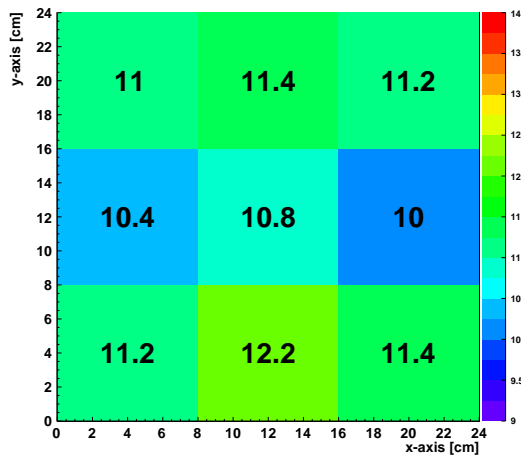


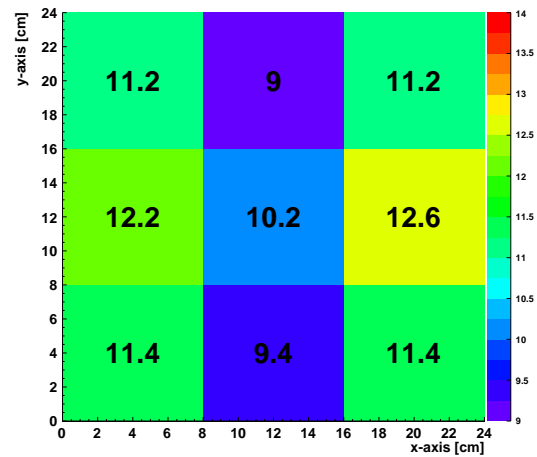
Figure 9.9: Tension measurement with Sefar Tensocheck 100 of a mesh stretched on an aluminium profile frame with Sefar system

The measurements of the mesh stretched by the sefar system show a tension in the middle of the mesh of 11.6 N cm^{-1} in x- and 11.8 N cm^{-1} in y-direction. The closer these values to each other the more homogenous the tension in the mesh. In comparison the difference of the values in the middle of the mesh stretched by the cheaper clamps is three times as large. This effect does occur on two different meshes with the same size as well. They are not shown here, but the difference in the Sefar-stretched mesh is again only 0.2 N cm^{-1} . For the other system it is 0.8 N cm^{-1} . This means that even in the smallest possible setup with only four clamps there are already inhomogeneities. They probably result from the fact, that the clamp, connected to the air cylinder, does experience different amounts of friction while moving along the guide rail. It is only consisting of a slit, in which a screw is inserted. The clamp is mounted on top of the screw, which is furnished with a nut. Despite the fact, that the surfaces of all stretching devices are very rough, all screws and nuts are tightened completely arbitrarily and differently from clamp to clamp. In comparison the movable parts of the Sefar clamps are on smooth surfaces and do not wiggle when slightly touched.

The maximum and minimum values of both measurements indicate a confirmation of the worse homogeneity of the clamps from the Yuangcheng Printing Equipment company. The differences of the maximum and minimum in the Sefar system are in x- and y-direction 2.6 N cm^{-1} and 2.0 N cm^{-1} . For the other system they are 2.2 N cm^{-1} and 3.6 N cm^{-1} .



(a) Tension measurement in x-direction



(b) Tension measurement in y-direction

Figure 9.10: Tension measurement with Sefar Tensocheck 100 of a mesh stretched on an aluminium profil frame with pneumatic clamps from Yuancheng Printing Equipment

In a long-term test it has been confirmed that both systems are able to keep the mesh tension for long periods of time. To test this a mesh has been inserted in the clamps and it has been stretched with about 15 N cm^{-1} for a week without interruption.

Conclusively it can be said, that the quality of the clamps from the chinese vendor is worse than the one from the european vendor. After extra adjusting, cleaning and sealing of the gas connections the clamps from the chinese vendor can do the job for the small meshes with only one clamp on each side. But the biggest problem for the stretching is, that the backing of the clamp for the mesh frame from the Yuancheng Printing Equipment company is flat, as it can be seen in 9.8. For bigger meshes, requiring more than one clamp per side, this flat backing will lead to periodic inhomogeneities in the mesh tension, because of the turn of the clamp when the meshframe is bent during the application of pressure. The backing of the Sefar clamps is tapered, solving the problem for bigger frames. But it should be mentioned also that the clamps from the chinese vendor are cheaper by a factor of about ten. The Sefar system requires no further time consuming adjustment and delivers great stretching quality.

9.2 Comparison of Sefar Tensocheck 100 and Newman Tension Meter

This section compares two different tension meters. One is the Sefar Tensocheck 100 and the other one is the Newman tension meter. They can be seen in figure 9.11 and 9.12.



Figure 9.11: Photo of the Newman and Sefar tension meter



Figure 9.12: Bottom view of the Newman tension meter and the Sefar Tensocheck 100; both tension meters have two parallel stationary bars at the borders, and a smaller movable one in the middle; because of this setup it is possible to obtain tension measurement data in the direction perpendicular to the footings

A tension meter is a small device used to measure the tension of meshes. The original use comes from the screen printing industry, where steel or fabric meshes are stretched and glued onto frames. These meshes need a high and homogenous tension. To ensure the quality of the meshes tension meters are used.

The next question is how a tension meter does work. The Sefar tension meter consists of a base (rectangle red platform in figure 9.11) and a vertical movable cylinder. The base includes two parallel stationary bars, which are displayed in figure 9.12. These footings have a width of 55 mm and a distance of 85 mm between each other. When taking a measurement, these footings are placed on the mesh. The movable part in the middle is pressing down on the mesh because of its own weight. Depending on the mesh tension the depth of immersion is smaller or larger. The measured distance of the movable part is then translated into a tension value. This translation is based on an internally and previously saved table, which is coming from calibration measurements by the producers of the device.

The Newman tension meter works almost the same. The width of the footings are 44 mm and the distance is 63 mm. The other difference comes from the fact, that the tension meter is analog and not digital. Additionally it is possible to read out the data of the Sefar device by a computer, whereas each measurement point of the analog device has to be documented by hand. Because of both tension meters' rectangular base shape with the two parallel footings, they can measure the tension directional-sensitive.

For further comparison the same industrial stretched mesh (110 cm × 130 cm) has been examined with both tension meters. Figure 9.13 shows how such a measurement has been performed.

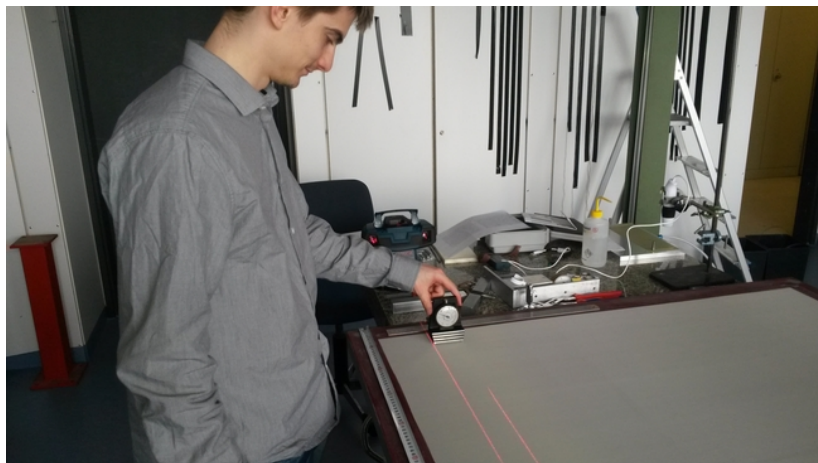
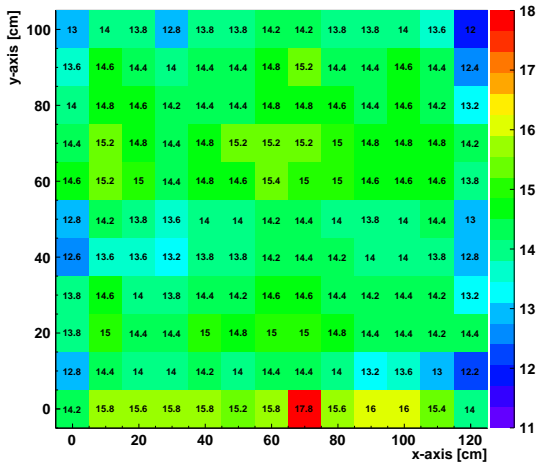


Figure 9.13: Photo of tension measurement with Newman tension meter; the red lines on the mesh are coming from a laser guiding system to ease the positioning of the tension meter

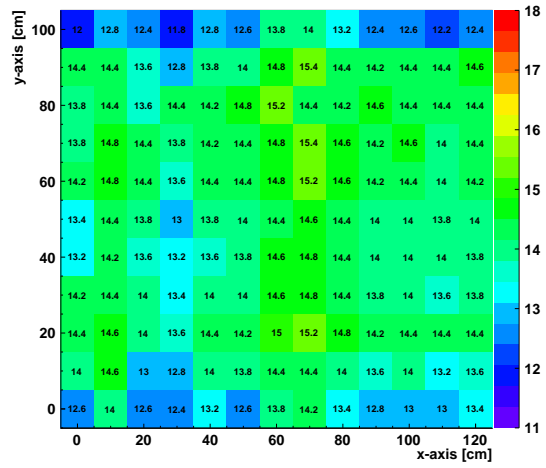
The tension measurement points are arranged in a chessboard-like grid with 10 cm distance between each other in x- and y-axis. Since both tension meters are directional sensitive, the mesh tension has been measured in both directions.

The results for the measurement with the Sefar device are shown in figure 9.14.

The results for the measurement with the Newman device are shown in figure 9.15.

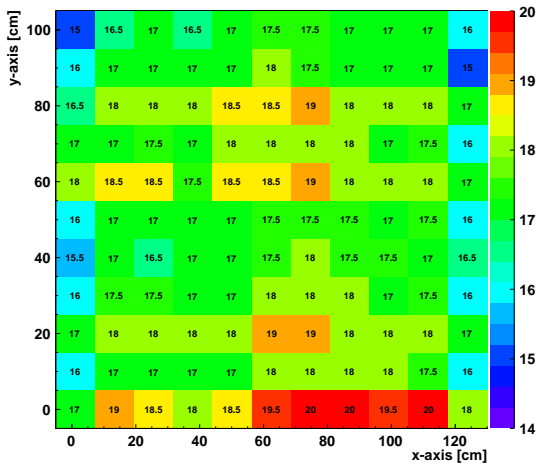


(a) Tension measurement in x-direction

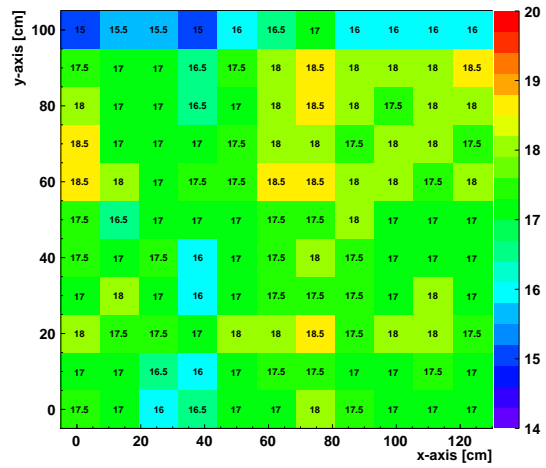


(b) Tension measurement in y-direction

Figure 9.14: Mesh tension measurement with Sefar Tensocheck 100



(a) Tension measurement in x-direction



(b) Tension measurement in y-direction

Figure 9.15: Mesh tension measurement with Newman tension meter

When comparing these two measurements, it can be seen that the maximum and minimum mesh tension distribution is similar. The Sefar device furthermore has a better resolution (0.2 N cm^{-1}) compared to the Newman product, which can hardly be read out more accurately than 0.5 N cm^{-1} . The difference between the minimal tension and maximal tension in x-direction is 5.8 N cm^{-1} for the Sefar device and 5.0 N cm^{-1} for the Newman tension meter. The differences in y-direction are 3.4 N cm^{-1} and respectively 3.5 N cm^{-1} . When taking into account the possibility of erroneous measurement points too close to the frame, the relative values are very similar. The most striking difference is that the Newman device has higher absolute values, see table 9.1. The mean value has an offset of 3.1 N cm^{-1} in x-direction and 3.3 N cm^{-1}

Tension meter	mean value	RMS
Sefar-in x-direction	14.4 N cm^{-1}	0.8 N cm^{-1}
Sefar-in y-direction	14.0 N cm^{-1}	0.7 N cm^{-1}
Newman-in x-direction	17.5 N cm^{-1}	0.9 N cm^{-1}
Newman-in y-direction	17.3 N cm^{-1}	0.7 N cm^{-1}

Table 9.1: Results of tension measurements

in y-direction. This simply relies on the fact, that the Newman tension meter is not calibrated anymore, but the Sefar Tensocheck is. For recalibration it needs to be sent back to the manufacturer. Next to the comparison of the two measurement devices, these measurements show, that industrially stretched meshes can have a deviation below 10 % of the mean value.

One of the most important tasks when handling meshes is to be careful to avoid kinks in the mesh, since they stay permanently and ruin the mesh for the use in the detector. Usually they are induced when creasing the mesh during transportation or insertion in the stretching clamps. Another source of kinks in the mesh can be the tension meter. Figure 9.16 shows several of these kinks in the mesh, occurring during the tension measurement.

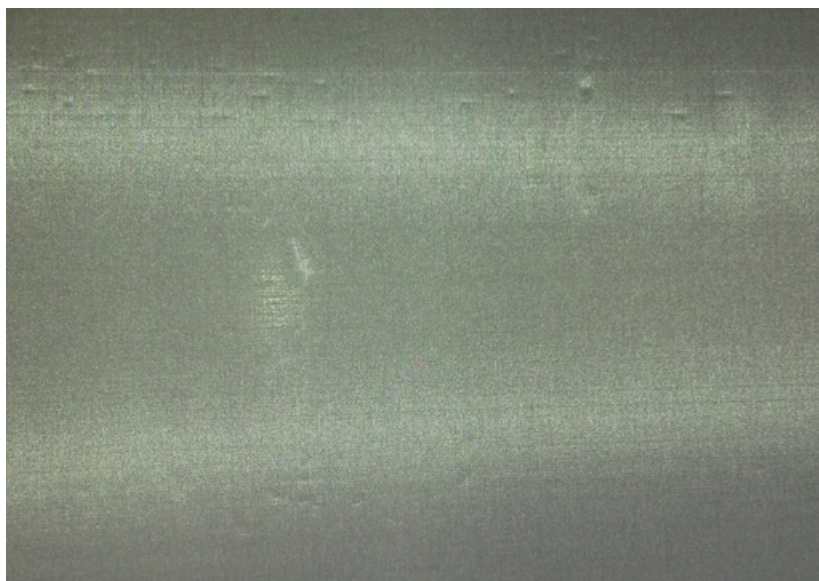


Figure 9.16: Mesh kinks induced by a tension meter

These kinks are created by lowering the tension meters by hand. One of the four edges of the footings will touch the mesh first. This focused pressure leads to the deformation (kink). If the footing of the tension meter has sharp edges, like the Newman tension meter has, it will almost always result in kinks. The Sefar tension meter in comparison has rounded edges. Careful use is therefore no problem for the mesh. Furthermore the mesh tension influences the likelihood of kink-induction. Mesh tensions of about 8 N cm^{-1} will result in kinks for both tension meters during the measurement. With 10 N cm^{-1} mesh tension the normal use of the Sefar tension meter does not produce kinks. Only very tilted and one sided loading induces deformations. If the mesh tension becomes higher, it is less likely to induce kinks while measuring the tension with a tension meter.

When taking into account all the points mentioned above, the Sefar Tensocheck 100 is superior.

9.3 Mesh Deflection between Pillars due to the Electric Field

After finding out how to stretch a mesh and how to measure its tension, the next point of interest is the deformation of the mesh, when it is implemented in the micromegas detector and voltage is applied. The mesh is supported on small pillars with a width of 0.3 mm and a height of $128 \mu\text{m}$ to ensure the correct distance between the mesh and the readout strips of the anode. The distance needs to be as homogenous as possible to ensure the same gas amplification across the active detector area. The effects can be seen in figure 9.1, where a 10% variation in gas gain is correlated to a $(2 - 2.5) \mu\text{m}$ variation in the amplification gap. Two different arrangements of the pillars are tested. The first one consists of quadratic unit cells with 7 mm side length. At each corner of the square is one pillar. The second arrangement type uses equilateral triangles with 7 mm side length as unit cells.

ANSYS simulations are used to test this issue. The difficulty of this task lies within the fact, that the stiffness of the mesh almost solely arises from the tension of the mesh. Because of a wire diameter of $18 \mu\text{m}$ the stiffness of the steel mesh, defined by its material properties, is extremely low. Only with correct application of the tension in the mesh the simulation can describe the behaviour of the mesh under loading.

The mesh is assumed to be an elastic material. If for example a 1 cm wide strip of the mesh is viewed as a rod with length L and cross-sectional area A , the following two relations of the tensile stress σ can be given:

$$\sigma = E \cdot \epsilon \quad (9.1)$$

$$\sigma = \frac{F}{A} \quad (9.2)$$

E denotes the modulus of elasticity and ϵ is the fraction of the change of length to

the total length of the beam in consideration.

$$\epsilon = \frac{\Delta L}{L} \quad (9.3)$$

To simulate the pretension in the mesh, it is stretched by a distance ΔL , which corresponds to a force F , which acts on a cross-sectional area of the mesh. When the equations 9.1, 9.2 and 9.3 are combined this value ΔL can be calculated.

$$\Delta L = L \cdot \frac{F}{A \cdot E} \quad (9.4)$$

With this formula all elongations, which correspond to different mesh tensions, can be calculated. These values are used in the simulations to introduce a displacement upon the borders of a mesh unit cell to simulate the force which pulls at the mesh from all directions in the mesh plane.

After establishing the pretension of the mesh the load of the electric field needs to be specified. The electric field between mesh and anode is usually in the order of 40 kV cm^{-1} . Since both layers can be assumed to be planar and parallel the picture of the parallel-plate capacitor is used for description. What is needed is the pressure, meaning the force on the area, which is induced because of the potential of the mesh. The energy of the homogenous field between the two condenser plates is described by:

$$W = \frac{1}{2} \cdot CU^2 = \frac{1}{2} \cdot \epsilon_0 \epsilon_r \frac{A}{d} U^2 \quad (9.5)$$

In this equation C denotes the capacitance, U the voltage, ϵ_0 is the vacuum permittivity, ϵ_r is the relative permittivity, A the area of the capacitor and d is the distance between the capacitor plates. To get the force between the plates, equation 9.5 needs to be differentiated with respect to the distance d . After rearranging and setting $\epsilon_r = 1$, because of the gas in the volume of the capacitor, the pressure resulting from the voltage in the mesh is:

$$\frac{F}{A} = \frac{1}{2} \cdot \epsilon_0 \frac{U^2}{d^2} \quad (9.6)$$

With all this information it is possible to simulate the deflection depending on the mesh tension. It has been performed for the two different pillar arrangements, each with three voltages -450 V , -540 V and -700 V . The results are summarized in figure 9.17 and figure 9.18.

The simulation of the triangular pillar arrangement shows smaller maximum deflections. It is obvious because the distance between the middle and the border in the square is larger than the distance in the equilateral triangle between the geometric centroid and the nearest border. A $1/x$ characteristic dependency of the deflection from the tension is visible in the plots in figure 9.17 and figure 9.18.

The pre-stretched mesh has been simulated based on the ideas described in [Groth and Müller, 2009]. It states, that the pre-stretched mesh, which can be viewed as a

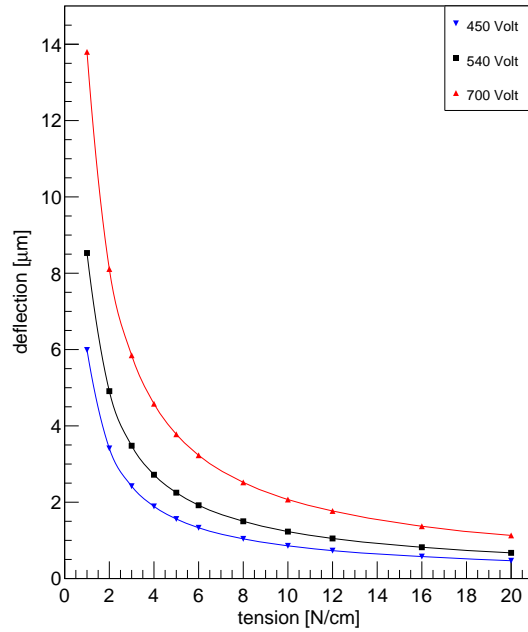


Figure 9.17: ANSYS simulations showing the deflection in the center of the mesh under different E-fields and mesh tensions with pillars forming 7 mm square unit cells

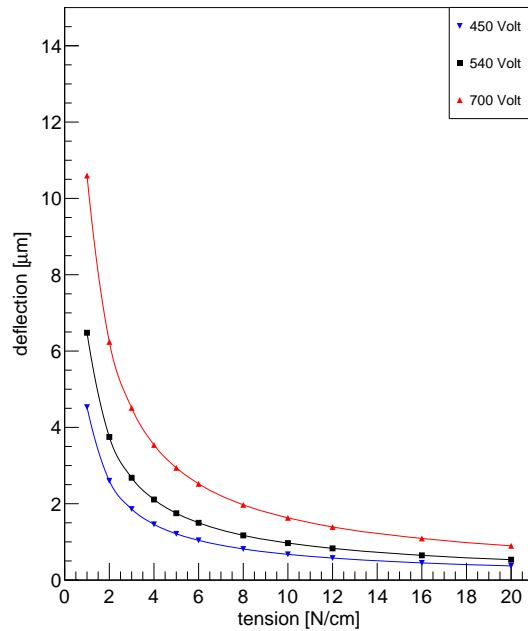


Figure 9.18: ANSYS simulations showing the deflection in the center of the mesh under different E-fields and mesh tensions with pillars forming a 7 mm triangle unit cells

membrane, can be described with equation 9.7.

$$S \cdot \nabla^2 u(x, y) = p \quad (9.7)$$

S denotes the pre-tension in the membrane, $u(x, y)$ is the deformation of the membrane and p is the constant pressure acting on the whole mesh. Equation 9.7 shows, that $1/S \propto \Delta u(x, y)$. This is the reason for the $1/x$ dependency of the deflection from the tension.

When looking at figure 9.18, it can be seen that for example for -540 V the maximum deflection of the mesh is $0.97 \mu\text{m}$ for a mesh tension of 10 N cm^{-1} . To get a maximum deformation of around $1 \mu\text{m}$ for -700 V a mesh tension of at least 16 N cm^{-1} is needed.

This section shows, that the triangular pillar setup is leading to less maximum deformation when an electric field applies pressure on the mesh. For example at an amplification gap of $128 \mu\text{m}$ a deformation of $(2 - 2.5) \mu\text{m}$ is leading to a deviation in gas amplification of about 10 %. If the deviation in the gas amplification for example should be below this value, the necessary mesh tension has to be at least 10 N cm^{-1} for a voltage of 700 V.

9.4 Sandwich Deformation because of Mesh Tension

This section is presenting an estimation of the deformation of a driftpanel sandwich due to mesh tension and the simultaneous reduction in mesh tension. The distance between the mesh and the neutral line (\approx middle) of the driftpanel is about 10 mm. The mesh is stretched with a tension of about 10 N cm^{-1} . This tension is leading to a bending moment at the borders of the panel, which is compensated by a bending moment in the middle of the panel, leading to a deformation of the whole panel. In an approximation the bending moments induced by the mesh are decoupled in x - and y -direction. This leads to a bending moment M for a 1 cm broad strip of the trapezoidal sandwich panel, which is approximated by a rectangle:

$$M = F \cdot d = 10 \text{ N} \cdot 0.01 \text{ m} = 0.1 \text{ N m},$$

where F is the force and d is the distance between the reference point and the point of force application. If the driftpanel is considered to be divided in 1 cm broad strips, the bending moment M is acting on each of them. This moment results in a force perpendicular to the sandwich plane. This force is acting on two lines in the middle of the driftpanel perpendicular to the corresponding mesh stretching direction. The two lines are represented by L_1 and L_2 in figure 9.19.

The forces on each centimeter of the lines are:

$$F_1 = \frac{0.1 \text{ N m}}{0.675 \text{ m}} = 0.148 \text{ N}$$

$$F_2 = \frac{0.1 \text{ N m}}{0.721 \text{ m}} = 0.138 \text{ N}$$

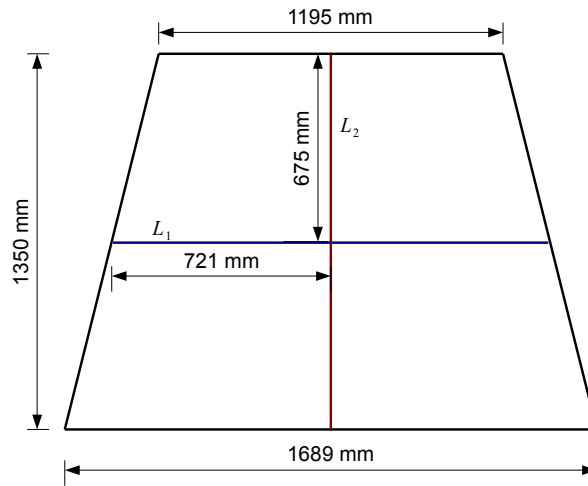


Figure 9.19: Schematic of drift panel showing the dimensions from a top view. The lines L_1 and L_2 are used to approximate the trapezoid as a rectangle with the dimensions of L_1 and L_2 .

The force F_1 is acting on line L_1 and force F_2 is acting on line L_2 . The total force on the lines can easily be calculated, because the length is known. With this information an ANSYS simulation is performed to find out the maximum deformation of the panel. In the simulation the borders of the panel, which is approximated by a rectangle with the dimensions of L_1 and L_2 , are able to rotate, meaning the panel is just simply supported on the borders. To get an estimation of the maximum loss of mesh tension due to panel deformation perpendicular to the panel plane, the sandwich at first does not contain the copper layer, reinforcing bars, interconnections or any fixation at the borders. With the forces calculated above, it results in a maximum deformation in the middle of $1180 \mu\text{m}$.

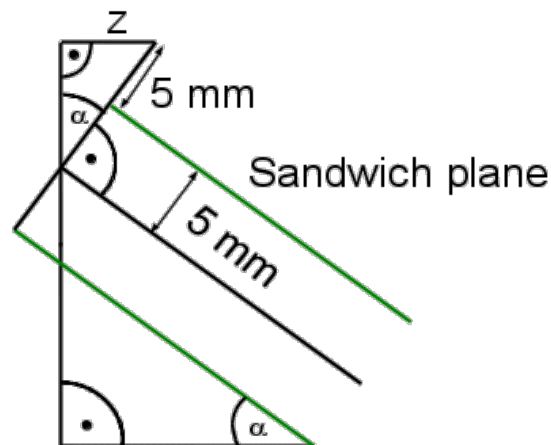


Figure 9.20: Schematic of connection between mesh displacement z and bending angle α of the sandwich panel at the border. The green lines represent the surfaces of the sandwich panel.

To calculate the distance z , which describes how much the mesh moves in one direction when the panel is bent, the angle α is needed. The relation between z

and α can be seen in figure 9.20. α is the inclination angle of the sandwich at the border where it is supported. The maximum inclination at the borders is given in the simulation as well. The inclination is $\tan \alpha$. With the knowledge of α it is possible to calculate z . The angle α is supposed to be small.

$$z_1 = 10 \text{ mm} \cdot \sin \alpha_1 = 27.4 \mu\text{m} \xrightarrow{\cdot 2} 54.8 \mu\text{m}$$

$$z_2 = 10 \text{ mm} \cdot \sin \alpha_2 = 25.2 \mu\text{m} \xrightarrow{\cdot 2} 50.4 \mu\text{m}$$

The reason to double the results for z is that each border bends and the total change in length of line L_1 and L_2 is of interest.

To find out how much tension is lost due to the deformation, a formula derived from Hooke's law is needed, which describes the elongation of an elastic beam due to tensile stress σ .

$$\sigma = E \cdot \epsilon$$

E is the E-modulus of the beam and ϵ is the change in length as fraction of total length.

$$\epsilon = \frac{\sigma}{E} = \frac{10 \text{ N}}{210 \text{ GPa} \cdot 18 \mu\text{m} \cdot 1 \text{ cm} \cdot 0.389} = 6.8 \cdot 10^{-4}$$

Since $\sigma = \frac{F}{A}$ and the steel mesh is not uniform, meaning it is not completely filled with a homogenous material, an effective area of it has to be used. A $18 \mu\text{m}$ thick steel wire, which is chosen for the simulation, has about $46.3 \mu\text{m}$ of space between its neighbour. This space between the wires has been calculated after investigating a steel mesh under an optical microscope. The calculations furthermore only look at a 1 cm broad strip. This leads to the factor $18 \mu\text{m}/46.3 \mu\text{m}=0.389$, which is multiplied with the area of the tensile stress.

If ϵ is multiplied with the length of L_1 and L_2 , the length change of the mesh is obtained in the two perpendicular directions, when the mesh is stretched with 10 N cm^{-1} . They are:

$$\Delta L_1 = \epsilon \cdot 1.350 \text{ m} = 918 \mu\text{m}$$

$$\Delta L_2 = \epsilon \cdot 1.442 \text{ m} = 981 \mu\text{m}$$

It is possible now to get the loss of mesh tension, when z_1 and z_2 is compared with ΔL_1 and ΔL_2 :

$$10 \text{ N cm}^{-1} \cdot \frac{54.8 \mu\text{m}}{918 \mu\text{m}} = 0.60 \text{ N cm}^{-1}$$

$$10 \text{ N cm}^{-1} \cdot \frac{50.4 \mu\text{m}}{981 \mu\text{m}} = 0.51 \text{ N cm}^{-1}$$

This means, that in the worst case, where the drift panel can deform much more than in reality, the mesh tension is reduced by about 5.5 % because of the rotation

of the borders of the panel. The maximum deformation, which has been shown before, is $1180\ \mu\text{m}$ for the sandwich in the simulation here. When the $35\ \mu\text{m}$ copper layer, reinforcing beams, six interconnections and fixation at the borders are taken into account, the maximum deformation in the middle of the panel is about $30\ \mu\text{m}$. This results in an inclination at the borders which leads to an absolutely negligible reduction of the mesh tension. In the estimation here the force, which deforms the panel is assumed to be constant, but in reality the force would decrease with the deformation of the panel and the reduction of the mesh length. This would result in even less deformation.

Despite the tilt of the borders only barely reducing the mesh tension, it has to be mentioned, that in the simulations and calculations here the frame of the mesh is assumed to not deform in the plane of the sandwich panel. This means the lines representing the borders of the sandwich panel in the simulation are fixated in x-,y- and z-direction, which means they are only able to rotate in every direction.

To investigate the compression of the driftpanel hollow aluminium beams with $3\ \text{cm} \times 1\ \text{cm}$ cross section and $1.5\ \text{mm}$ wall thickness are additionally introduced as frame. When these beams are pressed inwards with $10\ \text{N cm}^{-1}$ it results in a maximum deformation of about $50\ \mu\text{m}$. This would lead to a maximal mesh tension loss of about 5.4% . A mesh tension loss of this magnitude will hardly influence the deflection when loaded with an electric field, as shown in figure 9.18. This effect can therefore be neglected, because the real effect is even smaller.

10 Summary

In this thesis the construction of large area Micromegas detectors is discussed. On the basis of the construction of the mechanical prototype M1 the construction methodology of drift panels is explained. For the other panel type, the readout panels, slight modifications of the production process have to be made. The readout panels have pillars, with a height of 128 μm , attached to it. The auxiliary mesh for vacuum distribution can therefore be neglected. The requirement is, that the granite table and the stiffback have holes for evacuation.

The development of the stiffback, which is an important part of the construction process, from the initial design to the present one is the next important part of the thesis. The initial stiffback is not rigid enough, which leads to deformations of the sandwich panels during the construction process. ANSYS simulations are performed to improve the design. The resulting design uses a stiffback with two 1 mm thick aluminium plates, which sandwich a 8 cm thick aluminium honeycomb. The dimensions of the stiffback are $2 \times 1.5 \text{ m}^2$. The simulations show, that eight support points are sufficient to limit the deformation to a maximum of 32 μm , when loaded with a pressure corresponding to the weight of the SM2 module and taking into account the deformation under its own weight.

For characterization of the deformation and stiffness of sandwich structures, the sandwich beam theory has been introduced. It introduces the bending stiffness D , which describes the stiffness of the sandwich design. The parameter D can be used to compare different sandwich designs. Bending experiments have been performed, which show the validity of the theory in comparison with the measurements and simulations.

To check the planarity of a sandwich panel, three different measurement methods have been compared. The first one makes use of a straight edge and a feeler gauge. The second one uses an interferometer to scan the sandwich surface. The last method is a surface measurement with a coordinate measuring machine (CMM), which has proven to be the most practical one.

The two outer sandwich panels of each Micromegas quadruplet will be deformed by gas overpressure. To reduce this deformation for the optical alignment system, so-called interconnections have been introduced. Due to thorough ANSYS simulations, the total number of the interconnections for the SM2 module needed, could be reduced from initially proposed nine interconnections to six.

An important part of each Micromegas detector is the steel mesh, which separates the drift and amplification region. It has been shown, that small gap changes in the amplification region lead to big changes in the gas gain of the detector. To minimize the

sagging of the mesh, it is therefore stretched and supported by 128 μm large pillars. The deformation of the mesh, under the load of the electric field between the anode and the mesh, is simulated with ANSYS for various mesh tensions. The result is, that a triangular arrangement of the support pillars is leading to less deformation than the squared arrangement of the pillars. Another result is, that at an amplification gap of 128 μm a deformation of (2-2.5) μm is leading to a deviation in gas amplification of about 10 %. If the deviation in the gas amplification should be below this value, the necessary mesh tension has to be at least 10 N cm^{-1} for a voltage difference of 700 V between the mesh and the anode.

How to stretch the mesh has been shown as well, while comparing two systems from two different vendors. The stretching clamps from the Sefar company have proven to be superior in comparison to the clamps from the Yuangcheng Printing Equipment company. One aspect of the comparison is the ability to stretch meshes with homogenous mesh tension. This has been tested with a tension meter. Additionally two different tension meters have been compared. The Sefar Tensocheck 100 and the Newman ST1E tension meter. The Sefar Tensocheck is favourable, because of the less likely kink induction during the tension measurement and the increased accuracy.

A Material constants

	HC (9 mm cellsize)	HC (6 mm cellsize)	FR4
E_x [GPa]	1E-9	1E-9	19
E_y [GPa]	1E-9	1E-9	19
E_z [GPa]	0.63	1	9
PR_{xy}	0.5	0.5	0.11
PR_{yz}	0	0	0.3
PR_{xz}	0	0	0.3
G_{xy} [GPa]	1E-9	1E-9	3.6
G_{yz} [GPa]	0.28	0.44	3.5
G_{xz} [GPa]	0.14	0.22	3.5
ρ [$\frac{\text{kg}}{\text{m}^3}$]	59	83	1870

Table A.1: E-modulus, poisson ratio, shear modulus and density of different orthotropic materials used; the wall thickness for both honeycomb types is 76 μm

	Araldite 2011	Aluminium	Copper
E [GPa]	1.9	70	110
ν	0.35	0.34	0.34
ρ [$\frac{\text{kg}}{\text{m}^3}$]	1050	2700	8960

Table A.2: E-modulus, poisson ratio, shear modulus and density of different materials used

Bibliography

- ANSYS,Inc. ANSYS Mechanical APDL Element Reference, 2013. URL <http://148.204.81.206/Ansys/150/ANSYS%20Mechanical%20APDL%20Element%20Reference.pdf>.
- ATLAS Collaboration. The ATLAS Experiment at the CERN Large Hadron Collider. *Journal of Instrumentation*, 3, 2008.
- ATLAS Collaboration. New Small Wheel technical design report, 2013. URL <http://cds.cern.ch/record/1552862>.
- M.A.V. Chapman, R. Fergusson-Kelly, and W. Lee. Interferometric straightness measurement and application to moving table machines. <http://resources.renishaw.com>, 2013.
- Y. Giomataris, Ph. Rebourgeard, J.P. Robert, and G. Charpak. Micromegas: a high-granularity position-sensitive gaseous detector for high particle-flux environments. *Nuclear instruments & methods in physics research, Section A*, 1996.
- D.E. Groom, N.V. Mokhov, and S. Striganov. Muon stopping power and range tables 10 mev-100 tev. *Atomic Data and Nuclear Data Tables, Vol 76, No.2*, 2001.
- C. Groth and G. Müller. *FEM für Praktiker Band 3: Temperaturfelder*. expert verlag, 5th edition, 2009. ISBN 978-3-8169-2714-3.
- Ralf Hertenberger. Private Communication , 2014.
- Honeycomb Sandwich Design Technology*. Hexcel Corporation, 2000.
- K. Hirschfeld. *Baustatik - Theorie und Beispiele*. Springer, 5th edition, 2006. ISBN 3-540-36772-1.
- U. Huber. Entwurf und Dimensionierung von Sandwichstrukturen, 2011/2012.
- W.R. Leo. *Techniques for Nuclear and Particle Physics Experiments*. Springer-Verlag. Springer, 1994. ISBN 354057805.
- Philipp Lösel. Private Communication , 2014.
- D. Meschede. *Gerthsen Physik*. Springer, 24th edition, 2010. ISBN 978-3-642-12893-6.
- Elias Pree. Bestimmung der gasverstärkung und der kritischen entladungsdichte am micromegas detektor, 2012.

Acknowledgments

Ich möchte mich bei allen Personen bedanken und hoffe dass ich keine vergesse.

Ich möchte mich bei Prof. Dr. Otmar Biebel bedanken, dass ich diese Arbeit am Lehrstuhl schreiben konnte.

Ich möchte Dr. Ralf Hertenberger für die herausragende Betreuung und Unterstützung bei allem Problemen danken.

Ich möchte Prof. Dr. Dorothee Schaile für das spitzen Arbeitsklima an ihrem Lehrstuhl danken.

Ich möchte mich bei allen Kollegen der Hardware Gruppe bedanken, die mir immer geholfen haben, sei es bei Messungen, auf Dienstreisen oder beim Korrekturlesen der Arbeit.

Selbstständigkeitserklärung

Hiermit versichere ich, die vorliegende Arbeit selbstständig und unter ausschließlicher Verwendung der angegebenen Literatur und Hilfsmittel erstellt zu haben.

Ort, Datum

Elias Pree